

Theoretical studies
on analogue Hawking radiation
in quantum circuits

(量子回路における擬似的ホーキング輻射の理論的研究)

学位取得年月 2022年3月

片山 春菜

Contents

1	Introduction	1
1.1	Research background	1
1.1.1	Motivation	1
1.1.2	Basic concept of analogue black holes	4
1.1.3	Previous studies	5
1.2	Problem identification	7
1.3	Purpose	10
1.4	Structure of this thesis	11
2	Solitons in nonlinear transmission lines	12
2.1	Solitons	12
2.2	Reductive perturbation methods	13
2.3	Solitons in Josephson transmission lines	18
2.3.1	Model	18
2.3.2	Modified Korteweg-de Vries equation Soliton	19
2.4	Solitons in nonlinear LC transmission lines	22
2.4.1	Model	22
2.4.2	Nonlinear Schrödinger Soliton	24
2.5	Summary	28
3	Analogue black holes	29
3.1	Velocity of electromagnetic waves on transmission lines	29
3.2	Analogue black holes in Josephson transmissions lines	31
3.3	Analogue black holes in nonlinear LC transmission lines	34
3.4	Summary	35
4	Analogue Hawking radiation	37
4.1	Tunneling mechanism	37
4.2	Hawking temperature in Josephson transmission lines	43
4.3	The Hawking temperature in nonlinear LC transmission lines	45
4.4	Summary	47
5	Quantum-circuit black hole lasers	48
5.1	Requirements for constructing black hole lasers	49
5.2	Identifying issues and their approaches	56
5.3	Model	58

5.4	Quantum-circuit black hole lasers	60
5.4.1	Horizon resonators	61
5.4.2	Amplification of Hawking radiation	65
5.5	Entanglement entropy	76
5.6	Summary	76
6	Conclusion	78
6.1	Summary and conclusion	78
6.1.1	Analogue Hawking radiation	78
6.1.2	Quantum-circuit black hole lasers	79
6.2	Features and impacts	79
6.3	Future prospects	80
A	Designed analogue Black Hole Solitons in Josephson Transmission Lines	82
A.1	Designed analogue black hole solitons	82
A.1.1	Heterogeneous soliton pairs	83
A.1.2	Homogeneous soliton pairs	83
A.2	Analogue Hawking radiation	83
A.3	Summary	85
B	Solitonic black holes induced by magnetic solitons in a dc-SQUID array transmission line coupled with a magnetic chain	86
B.1	Magnetic solitons	87
B.1.1	Model	87
B.1.2	Ferrimagnetic-aligned nanoparticle chains	87
B.1.3	Effective ferromagnetic-aligned nanoparticle chains	89
B.1.4	Magnetic solitons as a magnetic-field source	90
B.1.5	90-degree magnetic solitons	91
B.1.6	180-degree magnetic solitons	92
B.2	Magnetic soliton induced analogue black hole	92
B.2.1	Black hole solitons induced by the 90-degree magnetic solitons	93
B.2.2	Black hole solitons induced by the 180-degree magnetic solitons	94
B.2.3	Magnetic soliton induced analogue black hole	96
B.3	Summary	98
B.4	Supplementary	100
	Acknowledgements	104
	Bibliography	105

Chapter 1

Introduction

1.1 Research background

1.1.1 Motivation

The ultimate goal of modern physics is to construct a “Theory of Everything” [1] that unifies the four forces in nature: strong nuclear force, weak nuclear force, electromagnetic force, and gravity. So far, human beings have succeeded in constructing the Standard Model of particle physics that addresses three of four known fundamental forces in Nature: electromagnetic force, weak nuclear force, and strong nuclear force. The remaining issue is to unify the Standard Model of particle physics and gravity. The Standard Model of particle physics is compatible with quantum mechanics which describes the microscopic world. However, gravity is incompatible with quantum mechanics, partly because of the different scales involved. To be more specific, gravity can be explained as the curvature of spacetime in general relativity, but if we apply this to quantum theory, the fine structure of spacetime in relativity itself will fluctuate due to the uncertainty principle. This is especially noticeable at singularities in spacetime such as a black hole. Therefore, the urgent task is to unify these two incompatible theories, namely general relativity and quantum mechanics.

Quantum gravity [2] has emerged as a physics field that describes gravity based on the principles of quantum mechanics. It deals with the quantum field theory in curved space-time. In the evaluation of many physical quantities, divergence occurs on the Planck scale where quantum theory and relativity meet. However, it is difficult to handle the divergence under gravity with renormalization used in ordinary quantum field theory. Thus, several approaches have been made to avoid these divergences such as string theory and loop gravity theory. In string theory, for instance, elementary particles are considered to be one-dimensional strings rather than points. This idea weakens the short-range integration (UV divergence) of the field appearing around the point. However, these are still incomplete and undeveloped theories.

On the other hand, it is also important to confirm the existence of the phenomenon itself involving quantum mechanics and gravity prior to the construction of quantum gravity. Note that the phenomenon we consider here is quantized in *classical* space-time while the gravitational field itself is quantized in quantum gravity. Hawking radiation [3,4] is the flux of particles with a thermal spectrum radiated from a black hole where even light cannot escape and has attracted much attention as one of the rare phenomena encountered by quantum mechanics and general relativity as discussed below.

Before proceeding to Hawking radiation, let us briefly review a black hole. The black hole is

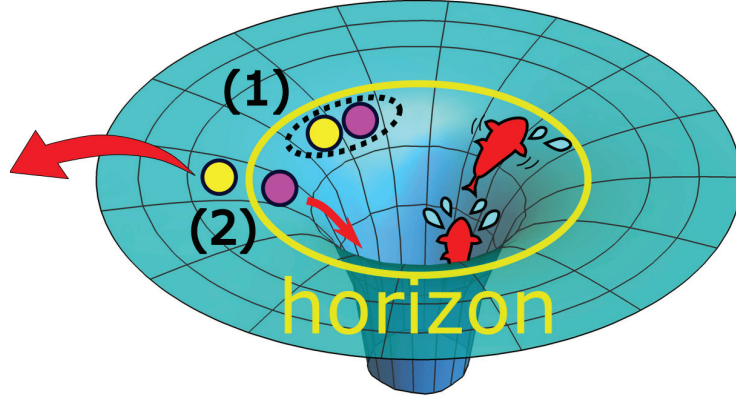


Figure 1.1: The sketch of the space-time curve of a black hole. The yellow line represents the event horizon which is a boundary of the black hole. No matter cannot escape from the black hole classically as shown on the right side. In quantum mechanics, a pair of particles and antiparticles are generated as shown in (1), and a particle is emitted as Hawking radiation while its partner falls into the black hole as shown in (2) by the vacuum fluctuations.

a region of spacetime where gravity is so strong that nothing even light can escape from it. It is formed by the gravitational collapse of stars with a large mass as follows. Stars release energy by reducing their mass due to internal nuclear fusion. The shape of the star is maintained if the internal force and the external force (gravity) are balanced. However, the star collapses by gravity when the star runs out of elements that can cause nuclear fusion. In this way, the star ends its life, and instead, a black hole with strong gravity is born.

According to the general theory of relativity proposed by Einstein, gravity represents the curvature of spacetime. In Riemannian spacetime with three dimensions of space and one dimension of time, the distance between two points x^μ and $x^\mu + dx^\mu$ in the coordinate is defined by

$$ds^2 = g_{\mu\nu} dx^\mu dx^\nu, \quad (1.1)$$

with the metric tensor $g_{\mu\nu}$ representing the curvature of spacetime, where we use the Einstein summation convention, in which an index variable appearing twice in a single term means the summation of that term over all the values of the index. In fields where gravity is very weak, spacetime can be regarded as an almost flat space called Minkowski space as

$$ds^2 = -c^2 dt^2 + dx^2 + dy^2 + dz^2. \quad (1.2)$$

On the other hand, the metric tensor is no longer Minkowski-like in a field with strong gravity. Einstein argued that the laws of physics must be written in the same form in every coordinate. Therefore, all physical quantities should be represented by tensors that are covariant with respect to coordinate transformations. The Einstein equation satisfying the requirement connects the existence of matter with the origin of gravity as follow,

$$R^{\mu\nu} - \frac{1}{2} g^{\mu\nu} R = \kappa T^{\mu\nu}, \quad (1.3)$$

where $R^{\mu\nu}$, R , and $T^{\mu\nu}$ are Ricci curvature tensor, Ricci scalar, and energy-momentum tensor, respectively. G is Newton's gravitational constant and $\kappa = 8\pi/c^4$ is Einstein's gravitational constant

with the speed of light c . According to this equation, gravity is the curvature of spacetime. By solving this equation about $g^{\mu\nu}$, we obtain the metric of the spacetime. Schwarzschild solved the Einstein equation for the gravitational field of a spherical object with a center at the origin on the assumption that the mass density is spherical symmetry and independent on time, and the space will be flat far away from the origin [5,6]. The solution called Schwarzschild metric is given as

$$ds^2 = - \left(c^2 - \frac{2GM}{r} \right) dt^2 + \frac{c^2}{c^2 - \frac{2GM}{r}} dr^2 + r^2 d\theta^2 + r^2 \sin^2 \theta d\varphi^2, \quad (1.4)$$

where M represents the mass of the spherical object. In this metric, there are singularity at $r = 0$ and $r = 2GM/c^2$. One of them at $r = 0$ called curvature singularity cannot be removed while another at $r = 2GM/c^2$ can be removed by selecting the appropriate coordinates. In Painlevé-Gullstrand coordinate

$$dt \rightarrow dt + \sqrt{\frac{2GM}{r}} \frac{1}{c^2 - \frac{2GM}{r}} dr, \quad (1.5)$$

Eq. (1.4) reduces to

$$ds^2 = - (c^2 - v^2(r)) dt^2 + 2v(r) dt dr + dr^2 + r^2 d\Omega^2, \quad (1.6)$$

where the singularity at $r = 2GM/c^2$ is removed. The metric tensor is

$$g_{\mu\nu} = \begin{pmatrix} v^2(r) - c^2 & v(r) & 0 \\ v(r) & 1 & 0 \\ 0 & 0 & r^2 \end{pmatrix}, \quad (1.7)$$

where $v(r) = \sqrt{2GM/r}$. The event horizon which is a boundary of a black hole is located at $g_{00} = 0$, i.e., $r = 2GM/c^2$. In short, gravity makes spacetime curved and forms a black hole which is a closed region. Nothing can escape from a black hole over the event horizon.

Nevertheless, Hawking proposed that there is thermal radiation from a black hole by considering the quantum effects [3,4]. According to the uncertainty principle of quantum mechanics, a pair of particles and antiparticles are unceasingly created and annihilated in the vacuum. Virtual particle pairs that arise quantum mechanically from a vacuum near the event horizon may result in one particle's escape as Hawking radiation from the black hole, while the partner particle with negative energy falls into it before the pair annihilation can happen as shown in Fig. 1.1. In short, Hawking radiation is a quantum phenomenon involving gravity, so it is considered to be an extremely significant consequence of quantum mechanics and general relativity. Therefore, the observation of Hawking radiation is a touchstone for evaluating possible unified theories of quantum mechanics and general relativity, i.e., quantum gravity.

However, it is unlikely to be measured from an actual black hole because it is much weaker than the background radiation. Here, we qualitatively derive the Hawking temperature by estimating the quantum fluctuations of energy in the vacuum which is the origin of Hawking radiation based on the uncertainty principle. The Hawking temperature is an important measure to assess the observability of Hawking radiation. We assume a Schwarzschild black hole with radius r and mass M , which has no charge and does not rotate. The time scale of the black hole is given as

$$\Delta t = \frac{2r}{c}, \quad (1.8)$$

where the velocity of the emitted particles is c . From the energy conservation law at the event horizon, we obtain

$$\begin{aligned}\frac{m}{2}c^2 &= G\frac{mM}{r}, \\ r &= \frac{2GM}{c^2},\end{aligned}\tag{1.9}$$

where m is the mass of the emitted particles. The time scale reduces to

$$\Delta t = \frac{4GM}{c^3}.\tag{1.10}$$

The relationship between energy and temperature is given as

$$E = k_B T\tag{1.11}$$

with the Boltzmann constant k_B . From the uncertainty principle

$$\Delta E \Delta t \simeq \hbar,\tag{1.12}$$

the Hawking temperature is given as

$$T_H = \frac{\Delta E}{k_B} = \frac{\hbar}{k_B \Delta t} = \frac{\hbar c^3}{4k_B GM},\tag{1.13}$$

where \hbar is the Planck constant h divided by 2π . There is a little difference between this result and original Hawking temperature T_H^o as

$$T_H^o = \frac{\hbar c^3}{8\pi k_B GM},\tag{1.14}$$

which is quantitatively derived based on the surface gravity [3, 4]. Let us estimate the Hawking temperature of the black hole with the mass $M = 10 \times (2 \times 10^{30})$ kg which is 10 times the solar mass as an example,

$$T_H^o \simeq \frac{(1.1 \times 10^{-34}) \cdot (3.0 \times 10^8)^3}{8 \cdot 3.1 \cdot (1.4 \times 10^{-23}) \cdot (6.8 \times 10^{-11}) \cdot (10 \times 2.0 \times 10^{30})} \simeq 3.9 \times 10^{-8}.\tag{1.15}$$

This is much smaller than the cosmic background radiation ($3K$). In this way, it is extremely difficult to observe Hawking radiation from an actual black hole. Therefore, it has been proposed to establish the basic principle of Hawking radiation using an analogue black hole artificially created in a laboratory system.

1.1.2 Basic concept of analogue black holes

Firstly, we briefly review an idea for generating analogue black holes in laboratory systems. Black holes are regions in space where gravity is so strong that nothing even light can escape. An event horizon is defined as a boundary that separates black holes from our world, beyond which events cannot affect an observer. For an intuitive understanding of event horizons, let us consider an example of carp climbing up a waterfall as shown in Fig. 1.2 (a). The carp can swim at the velocity

v_c against still water. The flow of the river is faster downstream and reaches the maximum at the waterfall. The velocity vectors of the carp in still water (v_c), flowing water ($v(x)$), and the carp against the flow of the river ($v_c + v(x)$) are indicated in Fig. 1.2 (b). The vector $v_c + v(x)$ points to the left downstream, which means the carp below the event horizon has flowed downstream. Therefore, the carp will fall into the basin if it cannot resist this flow. Figure 1.2 (c) shows the speed of the carp $|v_c|$ and the flow of the river $|v(x)|$. The unreturnable point occurs at the place x_h satisfying $|v_c| = |v(x)|$. This is the event horizon in an analogue black hole. The carp that is downstream from the event horizon cannot climb up the waterfall where $|v(x)| > |v_c|$, while it can swim freely at the upstream where $|v(x)| < |v_c|$. Therefore, the region where the carp cannot escape is considered as an analogue black hole in waterfalls. In this case, the carp plays the role of the light and the spatially varying velocity of the waterfall corresponds to the free-fall velocity in actual black holes. Note that we need to set up the background flow with spatial varying velocity to create analogue black holes in laboratory systems.

1.1.3 Previous studies

Based on the above basic idea, Unruh opened up the path for the studies of analogue black holes [7] by showing the analogy between the behavior of sound waves in a fluid cascade and that of light in the spacetime of a black hole. Sakagami et. al [8] proposed an experimental model of acoustic black holes using the transonic flow in a Laval nozzle as shown in Fig. 1.3. The background velocity $v(x)$ in a nozzle depends on space while the acoustic velocity v_c is fixed. The equation of motion for fluid can be written in terms of an effective metric as

$$ds^2 = - [v_c^2 - v^2(r)] dt^2 + 2v(r)drdt + dr^2 + r^2d\Omega^2, \quad (1.16)$$

which is in perfect agreement with the metric of the Schwarzschild black hole in Painlevé-Gullstrand coordinates as shown in Eq. (1.6). The background velocity $v(x)$ plays the role of the waterfall velocity, while the acoustic velocity v_c corresponds to the carp velocity in the above example. The background velocity reaches the sonic point at the throat in the nozzle corresponding to the event horizon. The supersonic region ($|v(x)| > |v_c|$) is the analogue black hole, where sound waves (phonons) cannot escape beyond the event horizon. After Unruh's seminal work, various systems of analogue black holes have been proposed [7, 9–13].

Here, let us look at the current state of studies on analogue black holes in the most highly advanced system, i.e., the Bose-Einstein condensate (BEC). BEC is a condensate formed by a macroscopic number of bosons falling into one quantum state as follows. At high temperatures, noble gas atoms obeying the Bose-Einstein quantum statistics can move freely with their own energies. At this time, the velocity distribution follows the Maxwell-Boltzmann distribution. As the temperature decreases, the quantum properties of the atom become more prominent, and the atom behaves as a wave. The wavefunctions of each atom overlap each other when the de Broglie wavelength becomes longer than the average interatomic distance. According to the Bose-Einstein quantum statistics, a macroscopic number of bosons takes the lowest-energy quantum state at low temperature. Therefore, BEC behaves as a quantum fluid and provides a background flow for generating analogue black holes. An analogue black hole in BEC is realized by spatially changing the quantum fluid velocity. In these studies, the sound is radiated as Hawking radiation instead of light. An acoustic analogue black hole is created by introducing a narrow region into the tube to form subsonic and supersonic regions. In this case, sound cannot escape from the supersonic region.

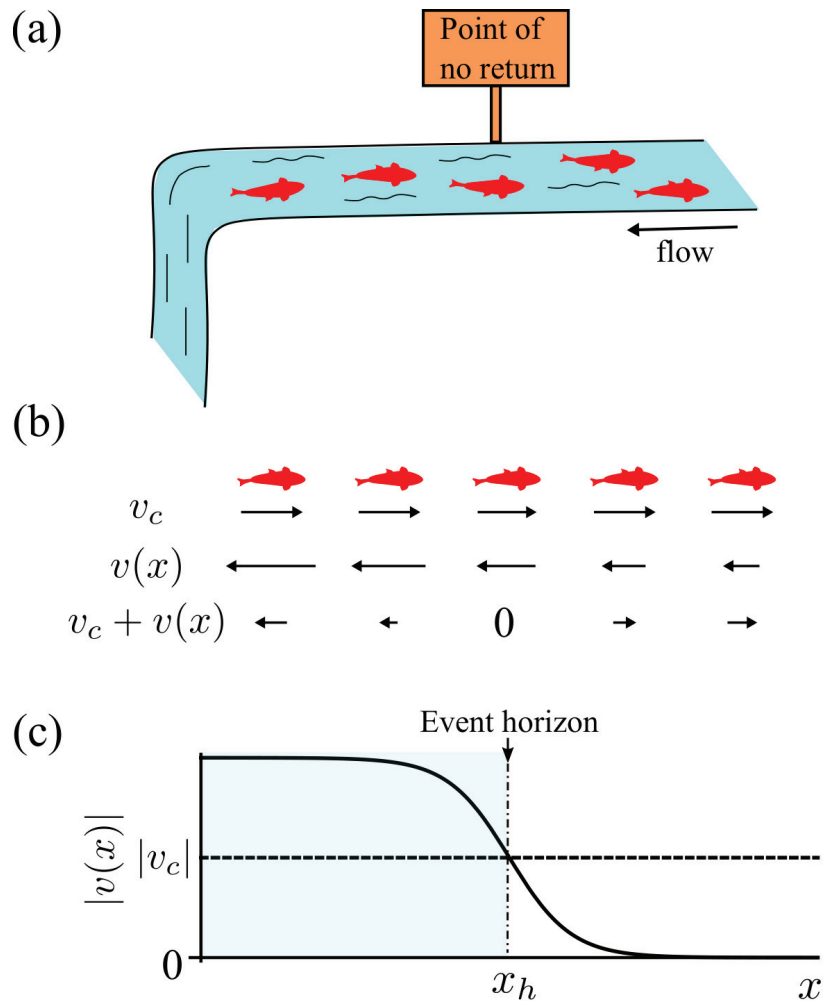


Figure 1.2: (a) A schematic diagram of carp climbing up a waterfall. (b) A diagram of the velocity vectors of the carp in still water v_c , the flow of the river $v(x)$, and the carp in the river $v_c + v(x)$. (c) A graph showing the spatial dependence of the flow speed in the river $|v(x)|$. The dotted line represents the speed of the carp $|v_c|$. The light blue area corresponds to the black hole.

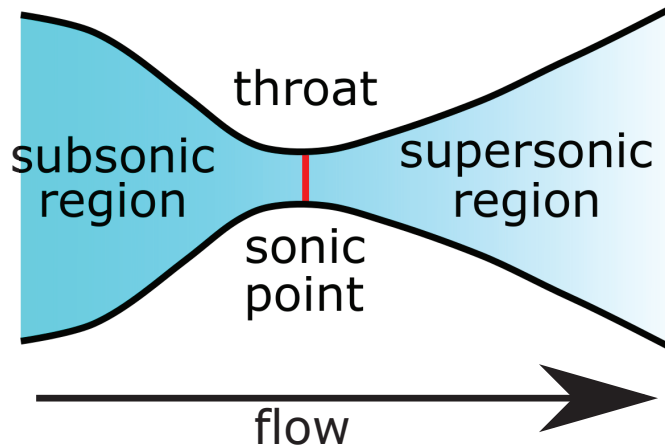


Figure 1.3: A Laval nozzle is a tube with a narrow throat near the center of it. The transonic flow is formed by applying different pressure on both ends. At the throat, the flow has the sonic point and a sonic horizon emerges.

In 2010, Steinhauer et al. experimentally realized analogue black holes using sound waves in Bose-Einstein condensed 10^5 rubidium poured into a tube [14]. The event horizon is created by accelerating the condensate to supersonic speeds with a laser, which introduces the spatially changes in the flow velocity in BEC. The sound waves are confined in the supersonic region corresponding to an analogue black hole. In 2016, Steinhauer reported that Hawking radiation was observed from a single black hole by measuring the correlation function between particles radiated outside the black hole and antiparticles falling inside [15]. Michel et al. theoretically analyzed the experiment and obtained the results in good agreement with the experimental results. However, Steinhauer's results are still being debated over whether the observed fluctuations are due to spontaneous quantum fluctuations or not [15–17].

Another promising system for an analogue black hole is optical fibers. The current status of the optical analogue black hole, which is our basis in quantum-circuit black hole laser, is as follows. In 2008, Philbin et al. succeeded in creating an analogue black hole by injecting light pulse into an optical fiber using a Ti: sapphire laser [12]. The incident pulse wave modulates the index of refraction δn proportional to its intensity I ($\delta n \propto I$) through the optical Kerr effect as shown in Fig. 1.4. The velocity of probe light in the optical fiber is then given as $v = c/(n_0 + \delta n)$ with c and n_0 being light velocity in vacuum and refractive index without modulations, respectively. Thus, the velocity of probe light slows down in the vicinity of the pulse. As a result, the probe light cannot overtake the pulse. This results in the event horizon, which is generated when the probe light and the pulse velocities are the same. Belgiorno et al. [18] and Rubino et al. [19] experimentally confirmed the radiation from the superluminal region. However, their results are not consistent with the characteristics expected from Hawking radiation.

1.2 Problem identification

There have been a lot of proposals of analogue black holes in various systems so far. However, measuring the Hawking radiation in those systems goes along with serious difficulties in terms of

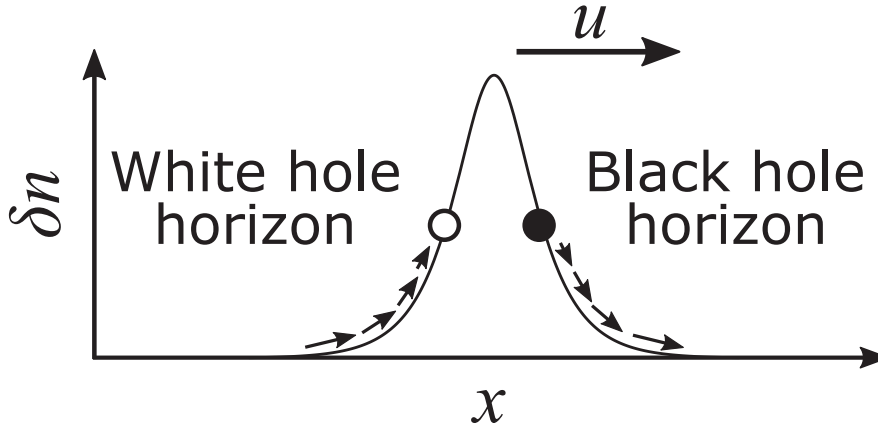


Figure 1.4: Schematic diagram of analogue black holes in optical fibers. The incident pulse moving with the constant velocity u modulates the refractive index by δn through the Kerr effect. The velocity of the probe light changes in space and two horizons are formed.

the detection of the very low Hawking temperature. On the other hand, electric circuits have many advantages over other systems, including scalability and controllability. Hawking radiation is expected since electric circuits have been miniaturized and can operate in the quantum mechanical domain. In addition, the detection of microwave photons and their quantum correlations in Josephson transmission lines has been proven through the study of the dynamical Casimir effect [20].

In analogue black holes in electric circuits, the situation is slightly different from the waterfall-climbing model of carp described earlier. The electromagnetic wave and reference wave play the roles of the carp and waterfall, respectively. To generate the event horizon, the spatial varying velocity of electromagnetic waves is required, which corresponds to the carp with the spatial varying ability to swim up. The reference wave is given depending on the systems and has a fixed velocity, which corresponds to a river on flat ground with a constant flow. Figure 1.5 (a) represents the vectors of the velocity of the electromagnetic waves, the reference wave, and their composition. Despite the differences in these roles compared to the example of the carp climbing the waterfall in Fig. 1.2, the same situation as the example is realized (compare the composite vectors in 1.2 (b) and 1.5 (a)). The event horizon of an analogue black hole appears where the velocity of the electromagnetic wave is equal to the velocity of the reference wave as shown in 1.5 (b).

In 2015, Schützhold et al. proposed an analogue black hole in the LC transmission line as shown in Fig. 1.6 (a) [11]. The velocity of electromagnetic waves propagating in transmission lines is given by both inductance and capacitance such as $v = a/\sqrt{LC}$ with the unit cell length a as described in Chapter 3. In their system, the permittivity $\varepsilon(t)$ of the capacitor is changed by illuminating the material with a laser to excite the electrons in it. Suppose laser light moves at a constant speed u , the capacitance in the transmission line has a spatial dependence such as $C(x, t) = C(x + ut)$, and the electromagnetic wave velocity is also modulated in space, resulting in an analogue black hole. However, there is a problem of heating by lasers. This makes it difficult to observe Hawking radiation. For example, the residual energy that makes high-frequency phonons have to be cooled to a Hawking temperature (10–100 mK) or less before it is converted to low-frequency electromagnetic waves in their system.

In 2009, Nation et al. [21] overcame the main problem of heating by using superconductivity

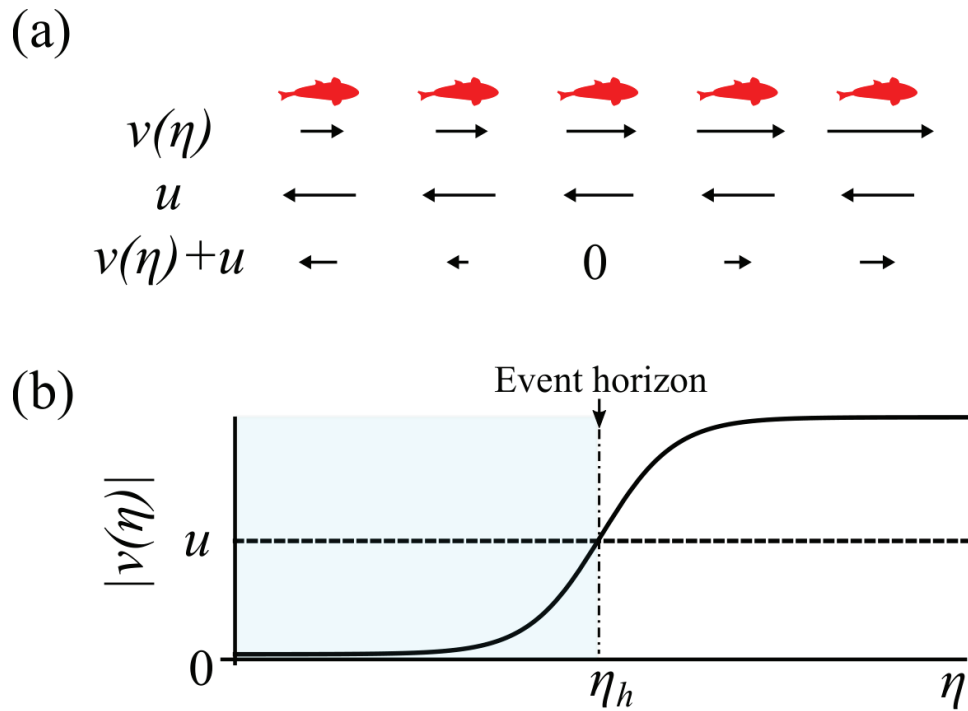


Figure 1.5: (a) A diagram of the velocity vectors of the electromagnetic wave $v(\eta)$, the reference wave u , and $v(\eta)+u$. The electromagnetic wave and reference wave play the roles of the carp and the flow of the river, respectively. (b) A graph showing the spatial dependence of the electromagnetic wave speed $|v(\eta)|$. The dotted line represents the speed of the reference wave u . The light blue area corresponds to a black hole.

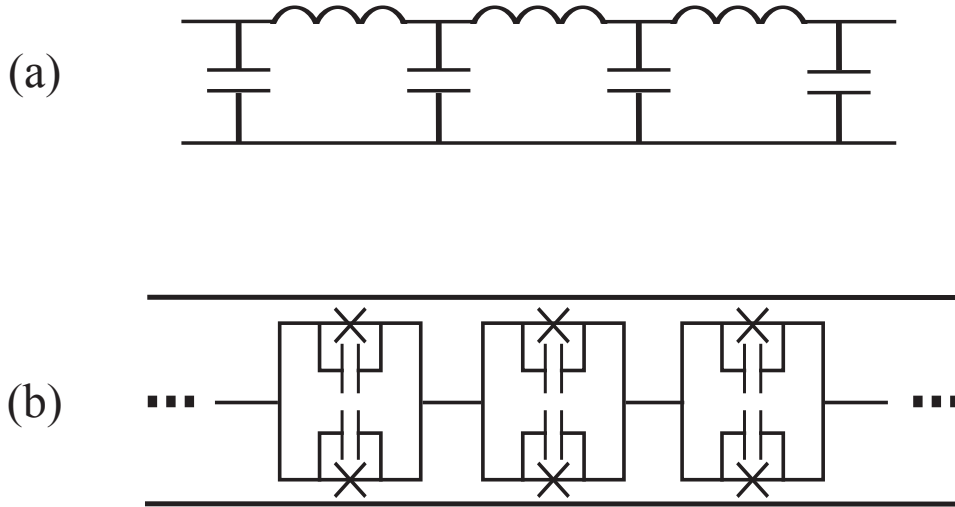


Figure 1.6: Schematic diagrams of the circuits for generations of analogue black holes. (a) Schützhold et al. proposed LC transmission lines. (b) Nation et al. proposed the dc-SQUID arrays.

in the waveguide. They applied an external magnetic field pulse moving at a constant speed to the dc superconducting quantum interference devices (dc SQUIDS) transmission line (Fig. 1.6 (b)). In the system, the Josephson inductance is spatially changed because it depends on the flux through dc SQUIDS. This leads to the spatial changes in the velocity of the electromagnetic waves propagating in the transmission line, resulting in an analogue black hole in their transmission lines. There are many advantages such as high-precision waveguide control based on strong coupling with electromagnetic waves and operability on the nanosecond time scale. However, the pulsed current that generates the external magnetic flux applied to the dc SQUID array is not stable and the shape of the wave collapses with time due to the wavenumber dispersion. This causes the problem that it cannot create a stable analogue black hole.

In this thesis, we propose analogue black holes using solitons to overcome the problems inherent in electric circuits. A soliton is a solitary wave created by balancing dispersion and nonlinearity of the nonlinear dispersive media that propagate stably after the collisions with other solitons [22–24]. This unique property has led to applications to information communication such as optical solitons and has provided a fundamental concept for understanding nonlinear physical phenomena in a variety of systems. In electrical circuits, the Toda (voltage) solitons obeying the Korteweg-de Vries (KdV) equation is well known in the nonlinear LC circuit with nonlinear capacitors, which gives the basic concept of soliton theory and its use for signal transmissions [25]. We explore a soliton obeying nonlinear evolution equations in electric circuits and apply it to the generation of analogue black holes.

1.3 Purpose

In this thesis, we discuss the observability of Hawking radiation as a touchstone for the construction of the quantum gravity theory. For this purpose, we propose analogue black holes on two types of transmission lines. One is a Josephson transmission line and the other is an LC transmission line

with nonlinear capacitors. These are electromagnetically dual to each other. We reveal that solitons exist on these transmission lines, and show that these solitons behave as analogous black holes. We also propose the black hole laser composed of two horizons to enhance Hawking radiation. Our purpose is to construct a theory to verify the Hawking radiation with our systems.

1.4 Structure of this thesis

This thesis is organized as follows. In Chapter 2, we derive equations that describe the waves hidden in the transmission lines (Josephson transmission lines and nonlinear LC transmission lines). Starting with a description of the circuit equation in our systems, we show that there are solitons that obey the nonlinear evolution equations. In Chapter 3, we show that the soliton obtained in Chapter 2 spatially changes the velocity of electromagnetic waves on the transmission lines, and then the analogue black hole is created by the solitons. In Chapter 4, we derive the Hawking temperature using the tunneling mechanism and discuss the observability of Hawking radiation. Chapter 5 outlines the principle of a black hole laser for the further amplification of Hawking radiation and then we propose a system that can realize a black hole laser in an electric circuit system. Finally, we conclude the thesis and describe the future prospects in Chapter 6.

Chapter 2

Solitons in nonlinear transmission lines

There have been some proposals for analogue black holes in electric circuits [11,21]. However, stable analogue black holes are unlikely to be formed in their system due to external field instability for control and the resulting heating problems. In this thesis, we propose analogue black holes using solitons that stably propagate with a fixed velocity to overcome the problem. A soliton is a solitary wave formed by balancing dispersion and nonlinearity in nonlinear dispersive systems. Therefore, soliton formation requires the introduction of nonlinearities into the system. There are two types of methods for introducing nonlinearity into transmission lines. One method is to use nonlinear inductance using Josephson's relation, and the other is to use nonlinear capacitance: Josephson transmission lines and LC transmission lines with nonlinear capacitors. These are electromagnetically dual to each other.

In this chapter, we review the concepts of solitons and their features in Section 2.1 at first. In Section 2.2, we describe the essence of the reductive perturbation method which is used to derive the nonlinear evolution equations from the circuit equations. Then, we derive the solitons propagating on both Josephson transmission lines and LC transmission lines with nonlinear capacitors in Sections 2.3 and 2.4, respectively. These sections are constructed in parallel. Starting from formulating the circuit equations for each model, we find the waves hidden in the circuit equations by using reductive perturbation methods. We derive a scale-invariant nonlinear evolution equation by considering the balance between dispersion and nonlinearity in the comoving frame of reference waves. Then, we obtain soliton solutions from the nonlinear evolution equations.

2.1 Solitons

In 1965, Zabusky and Kruskal [23] numerically analyzed a nonlinear partial differential equation called the Korteweg-de Vries equation describing water waves derived by D. J. Korteweg and G. de Vries [26]. They found that the obtained pulsed solitary wave solutions behave like a particle against collisions with each other and named the solitary wave as a soliton after the particle-like feature. Solitons have been studied more energetically since a method for analytically solving the Korteweg-de Vries equation was established in 1967 [24]. The nonlinear effect of waves makes waves sharpen and the dispersion effect diffuses the waves. A soliton is formed by balancing the dispersion and nonlinearity of the nonlinear dispersive media as shown in Fig. 2.1.

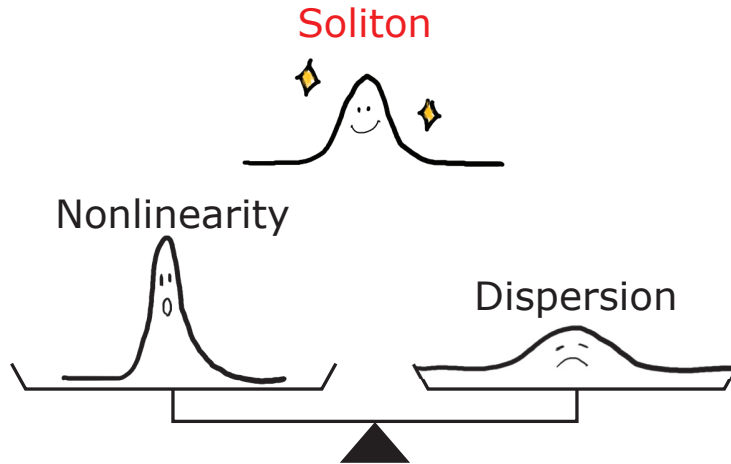


Figure 2.1: The nonlinearity of waves sharpens the shape of the waves and the dispersion diffuses the waves. A soliton is a solitary wave formed by the balance of dispersion and nonlinearity.

A soliton gives not only a fundamental concept for understanding nonlinear physical phenomena in various fields but it also has been applied to information communication such as optical solitons [27]. In electrical circuits, the Toda solitons [25,28] have been studied by generating voltage solitons in the nonlinear LC circuit to explore the basic concept of soliton theory and have been utilized to signal transmissions [29,30].

2.2 Reductive perturbation methods

Most physical phenomena are inherently nonlinear. Nevertheless, the analysis of these phenomena has been based on linear analysis, ignoring the nonlinearity due to mathematical difficulties for a long time. Therefore, as a natural approach, a perturbation method came up to express weakly nonlinear phenomena by taking into account variations from the linear approximation. The reductive perturbation method is an asymptotic perturbation theory that was first used by Gardner and Morikawa [24] to derive the KdV equation describing magnetohydrodynamic waves, and later generalized by Taniuti et al. [31–33]. This method can be summarized as follows: in a dispersive or dissipative medium with nonlinearity, even if their effects are small, a stable steady state is expected to exist in a wave field (far-field) far away from the wave source since the nonlinearity and the dispersion effect or the dissipative effect are balanced. In order to achieve this balance, we introduce a stretched coordinate with a small parameter ε and balance both effects with respect to this parameter to derive the nonlinear dispersive wave equation in the far-field. By this method, complex nonlinear equations can be reduced to simple nonlinear equations by decreasing their order. In this sense, this asymptotic method is then called the reductive perturbation method. In the following, we will use the example of a nonlinear pendulum to illustrate the essence of this method, which must be taken care of in perturbation methods in nonlinear systems, although it is not a wave problem that we will deal with in this thesis.

The equation of motion for a pendulum of length l with respect to the rotation angle $\theta(t)$ is given by

$$\frac{d^2\theta}{dt^2} + \frac{g}{\ell} \sin \theta = 0, \quad (2.1)$$

with the initial conditions

$$\theta(0) = a, \quad (2.2)$$

$$\left. \frac{d\theta}{dt} \right|_{t=0} = 0, \quad (2.3)$$

where g is the acceleration of gravity. Under these initial conditions, the pendulum oscillates periodically between $\pm a$. Thus, the rotation angle and time are scaled by a and the angular frequency $\omega = \sqrt{g/l}$, respectively, i.e., $\Theta = \theta/a$ and $\tau = \omega t$. Equation (2.1) is then rewritten as

$$\frac{d^2\Theta}{d\tau^2} + \frac{1}{a} \sin(a\Theta) = 0, \quad (2.4)$$

with the scaled initial conditions

$$\Theta(0) = 1, \quad (2.5)$$

$$\left. \frac{d\Theta}{d\tau} \right|_{\tau=0} = 0. \quad (2.6)$$

The Taylor series expansion of $\sin(a\Theta)$ is expressed as

$$\sin(a\Theta(\tau)) = a\Theta(\tau) - \frac{(a\Theta(\tau))^3}{3!} + \mathcal{O}(a^5). \quad (2.7)$$

Here, assuming that the angle of rotation is small, we truncate at the first nonlinear term in the above equation. The equation of motion of the pendulum, Eq (2.4), is given by

$$\frac{d^2\Theta(\tau)}{d\tau^2} + \Theta(\tau) = \frac{a^2}{6}\Theta^3(\tau). \quad (2.8)$$

This is the so-called Duffing's equation, which is well known in the field of nonlinear vibration. This equation represents a simple pendulum if the right-hand side is zero. The right-hand side is therefore a perturbation term that represents the non-linear effect on the linear equations. The parameter a^2 can be regarded as a small perturbation parameter.

Now, let us solve this nonlinear equation, Eq. (2.8), using the *regular* perturbation method. The nonlinear equation can be solved by an asymptotic expansion that introduces the nonlinearity perturbatively with a^2 as the perturbation parameter in the vicinity of the linear approximation. To represent the solution in the asymptotic expansion of a^2 , we now expand $\Theta(\tau)$ in powers of a^2 as

$$\Theta(\tau) = \Theta_0(\tau) + a^2\Theta_1(\tau) + \mathcal{O}(a^4). \quad (2.9)$$

Substituting this into Eq. (2.8) and rearranging them by the power of a^2 , we get

$$\left(\frac{d^2\Theta_0(\tau)}{d\tau^2} + \Theta_0(\tau) \right) + a^2 \left(\frac{d^2\Theta_1(\tau)}{d\tau^2} + \Theta_1(\tau) - \frac{1}{6}\Theta_0^3(\tau) \right) + \mathcal{O}(a^4) = 0. \quad (2.10)$$

From this, the coefficients for each power must be identically zero in order to obtain the solution. This yields the sequence of problems.

$\mathcal{O}(1)$ problem: The leading-order is unchanged from the linear system, i.e., simple pendulum.

$$\frac{d^2\Theta_0(\tau)}{d\tau^2} + \Theta_0(\tau) = 0, \quad (2.11)$$

$$\Theta_0(0) = 1, \quad (2.12)$$

$$\left. \frac{d\Theta_0}{d\tau} \right|_{\tau=0} = 0. \quad (2.13)$$

The solution is given by

$$\Theta_0(\tau) = \cos \tau. \quad (2.14)$$

$\mathcal{O}(a^2)$ problem: At $\mathcal{O}(a^2)$, we have

$$\frac{d^2\Theta_1(\tau)}{d\tau^2} + \Theta_1(\tau) - \frac{1}{6}\Theta_0^3(\tau) = 0, \quad (2.15)$$

$$\Theta_1(0) = 0, \quad (2.16)$$

$$\left. \frac{d\Theta_1}{d\tau} \right|_{\tau=0} = 0. \quad (2.17)$$

By using the $\Theta_0(\tau)$ solution, this equation is rewritten as

$$\frac{d^2\Theta_1(\tau)}{d\tau^2} + \Theta_1(\tau) = \frac{1}{24}(\cos(3\tau) + 3\cos(\tau)), \quad (2.18)$$

where the formula $\cos^3 \tau = (\cos 3\tau + 3\cos \tau)/4$ is used. This is nothing but the equation of motion of a forced oscillation subjected to periodic external forces consisting of two different angular frequencies. Thus, nonlinear oscillations involve essentially different time scales. The second term on the right-hand side of this equation represents the resonant force. This causes a situation that is not physically appropriate, as we will see below.

Solving the equation using the previous solution of $\Theta_0(\tau)$, we obtain the $\Theta_1(\tau)$ solution

$$\Theta_1(\tau) = \frac{1}{192}(\cos \tau - \cos 3\tau) + \frac{1}{16}\tau \sin \tau. \quad (2.19)$$

As a result, the solution (2.9) incorporating up to the first-order perturbation is given by

$$\Theta(\tau) = \cos \tau + a^2 \left[\frac{1}{192}(\cos \tau - \cos 3\tau) + \frac{1}{16}\tau \sin \tau \right] + \mathcal{O}(a^4). \quad (2.20)$$

This solution contains a secular term that grows linearly in τ . It is physically unsuitable for the angle of rotation to increase even though energy is not injected from the outside. As a result, the expansion Eq. (2.9) is not uniformly valid in τ and breaks down when $\tau = \mathcal{O}(a^2)$ and $a^2\Theta_1$ is no longer a small correction to Θ . This is due to the fact that we dealt with phenomena that appear on different time scales in linear and nonlinear systems at the same time. Therefore, this can be avoided by using a *singular* perturbation method that takes them into account. Physically, the amplitude dependence of the frequency is involved. The frequency is amplitude-independent in

simple oscillation, whereas the frequency is amplitude-dependent in nonlinear oscillations. These produce different frequencies equivalent to different timescales. In fact, the secular term in Eq. (2.20) arises from the Taylor expansion of the frequency part for small ϵ as follows:

$$\cos[(1 + \epsilon)t] \sim \cos t - \epsilon t \sin t + \mathcal{O}(\epsilon^2). \quad (2.21)$$

Note that this asymptotic expansion is valid only when $t \ll 1/\epsilon$. This indicates that the frequency modulation due to nonlinear vibration could not be properly incorporated in a regular perturbation method with only one time scale. Therefore, it can also be improved by considering the frequency instead of the time.

To construct a uniformly valid solution, we have to introduce multi-scale time variables. Equation (2.8) is the equation of motion for a simple pendulum with the eigenfrequency ω when the right-hand side is zero. On the other hand, the right-hand side represents the nonlinear restoring force, which modulates the frequency with the nonlinearity. Therefore, the frequency is no longer fixed as described above, but must be treated as $\bar{\omega} = \Omega(a^2)\omega$, which depends on the parameter a^2 for nonlinearity, where

$$\Omega(a^2) = \Omega_0 + a^2\Omega_1 + \mathcal{O}(a^4). \quad (2.22)$$

As shown above, this corresponds to the introduction of different time scales. By taking this modulation into account, Eq. (2.8) becomes

$$\Omega^2(a^2) \frac{d^2\Theta(s)}{ds^2} + \Theta(s) = \frac{a^2}{6}\Theta^3(s), \quad (2.23)$$

where $s = \Omega(a^2)\tau$ with the initial conditions written as

$$\Theta(0) = 1, \quad (2.24)$$

$$\left. \frac{d\Theta}{ds} \right|_{s=0} = 0. \quad (2.25)$$

$\Theta(s)$ can be expanded as

$$\Theta(s) = \Theta_0(s) + a^2\Theta_1(s) + \mathcal{O}(a^4), \quad (2.26)$$

similar to Eq. (2.9). Substituting Eq. (2.26) into Eq. (2.23), we obtain

$$\left(\Omega_0^2(a^2) \frac{d^2\Theta_0(s)}{ds^2} + \Theta_0(s) \right) + a^2 \left(\Omega_0^2 \frac{d^2\Theta_1(s)}{ds^2} + \Theta_1(s) - \frac{1}{6}\Theta_0^3(s) + 2\Omega_0\Omega_1 \frac{d^2\Theta_0(s)}{ds^2} \right) + \mathcal{O}(a^4) = 0, \quad (2.27)$$

and the coefficients for each power must be identically zero.

$\mathcal{O}(1)$ problem:

$$\frac{d^2\Theta_0(s)}{ds^2} + \Theta_0(s) = 0, \quad (2.28)$$

$$\Theta_0(0) = 1, \quad (2.29)$$

$$\left. \frac{d\Theta_0}{ds} \right|_{s=0} = 0. \quad (2.30)$$

This solution is given by

$$\Theta_0(s) = \cos(s). \quad (2.31)$$

$\mathcal{O}(a^2)$ problem:

$$\Omega_0^2 \frac{d^2 \Theta_1(s)}{ds^2} + \Theta_1(s) - \frac{1}{6} \Theta_0^3(s) + 2\Omega_0 \Omega_1 \frac{d^2 \Theta_0(s)}{ds^2} = 0. \quad (2.32)$$

This gives rise to

$$\frac{d^2 \Theta_1(s)}{ds^2} + \Theta_1(s) = \left(\frac{1}{8} + 2\Omega_1 \right) \cos s + \frac{1}{24} \cos 3s, \quad (2.33)$$

when the solution $\Theta_0(s) = \cos(s)$ is taken into account. The coefficient of the term $\cos s$ that generates the divergent solution should be zero to obtain a periodical solution. We set $\Omega_1 = -1/16$ and then obtain a solution

$$\Theta_1(s) = A_1 \sin s + B_1 \cos s - \frac{1}{192} \cos 3s, \quad (2.34)$$

where A_1 and B_1 are constants. As a result, a periodical solution described as

$$\begin{aligned} \theta(t) &= a\Theta(\omega t) \\ &= a \{ \Theta_0(s) + a^2 \Theta_1(s) \} + \mathcal{O}(a^4) \\ &= a \left\{ \cos s + a^2 \left(A_1 \sin s + B_1 \cos s - \frac{1}{192} \cos 3s \right) \right\} + \mathcal{O}(a^4) \\ &= a \cos(\Omega(a^2)\omega t) + \mathcal{O}(a^3) \\ &= a \cos \left[\left\{ 1 - \frac{1}{16} a^2 + \mathcal{O}(a^4) \right\} \omega t \right] + \mathcal{O}(a^3) \\ &= a \cos \bar{\omega} t + \mathcal{O}(a^3), \end{aligned} \quad (2.35)$$

where

$$\bar{\omega} = \Omega(a^2)\omega = \left(1 - \frac{1}{16} a^2 + \mathcal{O}(a^4) \right) \omega. \quad (2.36)$$

The solution is also written as

$$\theta(t) = a \cos \omega \bar{t}, \quad (2.37)$$

with the stretched time scale

$$\bar{t} = \Omega(a^2)t = \left(1 - \frac{1}{16} a^2 + \mathcal{O}(a^4) \right) t, \quad (2.38)$$

where the nonlinear effects are included in the time coordinate.

In short, regular perturbation methods for nonlinear systems breaks down since the multiple time scales inherent in the nonlinearity cause resonance, resulting in a secular term. Therefore, the singular perturbation method avoids this problem by introducing multiple time scales. On the other hand, the waves treated in this thesis have degrees of freedom not only in time but also in space. In that case, the dispersion relation plays a role in introducing different time scales. This will be discussed in detail in the next section.

2.3 Solitons in Josephson transmission lines

In this section, we show the existence of soliton in a Josephson transmission line. At first, we show the circuit model for the Josephson transmission lines and derive the circuit equation. We also explore the waves hidden in the circuit equation by using the perturbation method. And then, we obtain the modified Korteweg-de Vries (mKdV) equation and its soliton solution.

2.3.1 Model

Let us consider a coplanar Josephson transmission line indicated in Fig. 2.2, where all Josephson junctions are assumed to have identical critical current I_c and capacitance C . This transmission line is a dual to nonlinear LC transmission line described in the next section.

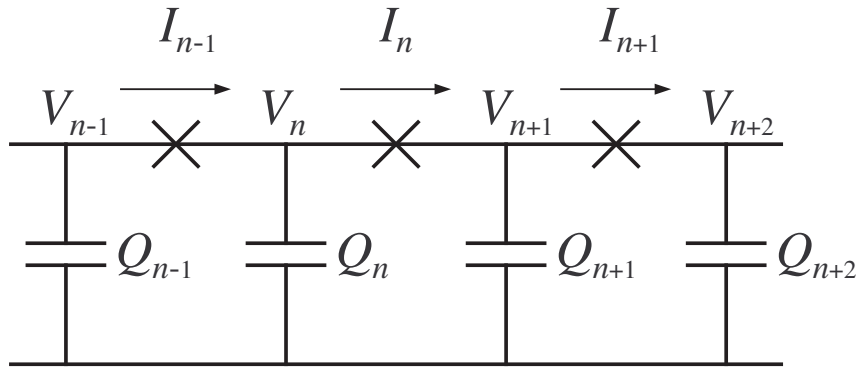


Figure 2.2: Schematic diagram of a Josephson transmission line. The cross indicates a Josephson junction. I_n , V_n , and Q_n represent the current, voltage, and electric charge of the n th junction, respectively.

Nonlinear inductance

The Josephson inductance is derived as follows. In general, inductance is defined as

$$V = L \frac{dI}{dt}, \quad (2.39)$$

where V , I , and L are the voltage, current, and inductance. From Josephson relation, we obtain

$$\frac{\partial I}{\partial t} = \frac{\partial I}{\partial \theta} \frac{\partial \theta}{\partial t} = I_c \cos \theta \frac{2e}{\hbar} V, \quad (2.40)$$

for Josephson junctions, where θ is the phase difference with I_c , \hbar and e being the critical current, the Planck constant h divided by 2π and the elementary electric charge, respectively. Compared with Eq. (2.39), the Josephson inductance is defined as

$$L = \frac{\hbar}{2eI_c} \frac{1}{\cos \theta} = \frac{L_J}{\cos(\arcsin(I/I_c))}, \quad (2.41)$$

where $L_J = \hbar/2eI_c$. This means that the Josephson transmission line has a nonlinear inductance so that it is dual to the LC transmission line with nonlinear capacitors. This implies that there exist current solitons in Josephson transmission lines.

Circuit equation

Now let us derive the circuit equation. From Kirchhoff's law together with the Josephson relation, the circuit equations are given by

$$I_n(t) - I_{n-1}(t) = C \frac{dV_n(t)}{dt}, \quad (2.42)$$

and

$$V_{n+1}(t) - V_n(t) = \frac{\hbar}{2e} \frac{d\theta_n(t)}{dt}. \quad (2.43)$$

I_n , V_n and θ_n represent the current, voltage, and phase difference of the n th Josephson junction on the line, respectively. These equations lead to the discrete equation of motion for the phase difference as

$$\frac{\hbar}{2e} C \frac{d^2\theta_n(t)}{dt^2} = I_{n+1}(t) + I_{n-1}(t) - 2I_n(t). \quad (2.44)$$

In continuum approximation, i.e., $I_n(t) = I(x, t) \equiv I$ together with the Josephson relation

$$\theta = \sin^{-1} \frac{I}{I_c} = \sum_{i=1}^{\infty} \frac{1}{(2i-1)!} \left(\frac{I}{I_c} \right)^{2i-1}, \quad (2.45)$$

Eq. (2.44) is reduced to

$$\frac{\hbar}{2e} C \frac{\partial^2}{\partial t^2} \left\{ \sum_{i=1}^{\infty} \frac{1}{(2i-1)!} \left(\frac{I}{I_c} \right)^{2i-1} \right\} = \sum_{i=1}^{\infty} \frac{2a^{2i}}{(2i)!} \frac{\partial^{2i}}{\partial x^{2i}} I. \quad (2.46)$$

By introducing the normalized variables $\bar{x} = x/a$ and $\bar{t} = t/\omega_J^{-1} = t\sqrt{I_c/(C\hbar/2e)}$ with ω_J being the Josephson plasma frequency, the equation reduces to

$$\frac{\partial^2}{\partial \bar{t}^2} \left\{ \sum_{i=1}^{\infty} \frac{1}{(2i-1)!} \bar{I}^{2i-1} \right\} = \sum_{i=1}^{\infty} \frac{2}{(2i)!} \frac{\partial^{2i}}{\partial \bar{x}^{2i}} \bar{I}, \quad (2.47)$$

where $\bar{I} = I/I_c$.

2.3.2 Modified Korteweg-de Vries equation Soliton

Now let us find the wave nature hidden in the circuit equation by using the reductive perturbation method [33], which is an asymptotic perturbation expansion to derive a scale-invariant nonlinear evolution equation in the vicinity of a linear approximation.

Firstly, let us consider the dispersion under the linear approximation. In this limit, Eq. (2.47) becomes

$$\frac{\partial^2 \bar{I}}{\partial \bar{t}^2} = \frac{\partial^2 \bar{I}}{\partial \bar{x}^2} + \frac{1}{12} \frac{\partial^4 \bar{I}}{\partial \bar{x}^4} + \dots, \quad (2.48)$$

and we obtain

$$\omega^2 = k^2 - \frac{k^4}{12} + \mathcal{O}(k^6), \quad (2.49)$$

with the frequency ω and wavenumber k by substituting the plane solution expressed as

$$\bar{I} = \exp \{i(k\bar{x} - \omega\bar{t})\}. \quad (2.50)$$

In the long-wavelength approximation, the wavenumber k is small and we obtain the dispersion relation expressed as

$$\omega \simeq k \left(1 - \frac{k^2}{24}\right). \quad (2.51)$$

Here, we set $k = \varepsilon^p \kappa$ with a small parameter ε to express that k is small enough, where κ is of the order of 1 and p represents how small the wavenumber k is. The deviation $k^2/24$ from the non-dispersion relation $\omega = k$ should be represented by the small parameter $\varepsilon \sim k^2$, so we set $p = 1/2$. This dispersion relation plays exactly the same role as the different frequencies shown in Eq. (2.36) in the singular perturbation method, leading equivalently to multi-time scales in the systems. In fact, two different time scales are introduced into the phase of the linear wave and integrated into stretched variables that represent slow phenomena as follows

$$\begin{aligned} k\bar{x} - \omega\bar{t} &= \varepsilon^{\frac{1}{2}}(\bar{x} - \bar{t}) - \frac{1}{24}\varepsilon^{\frac{3}{2}}\bar{t} + \mathcal{O}(\varepsilon^{\frac{5}{2}}) \\ &= \xi - \frac{1}{24}\tau + \mathcal{O}(\varepsilon^{\frac{5}{2}}), \end{aligned} \quad (2.52)$$

where the stretched (slow) variables called the Gardner-Morikawa transformation is introduced as

$$\begin{cases} \xi = \varepsilon^{\frac{1}{2}}(\bar{x} - \bar{t}) \\ \tau = \varepsilon^{\frac{3}{2}}\bar{t}, \end{cases} \quad (2.53)$$

which are slowly changed against the changes of \bar{x} and \bar{t} because ε is a small parameter. $\xi = (\varepsilon^{1/2}/a)(x - a\omega_J t)$ is the comoving frame with the phase velocity $a\omega_J$ of the linear wave in the long-wavelength approximation and the changes of the waves caused by the dispersion are small in this frame. In this way, the dispersion effect can be successfully described by a parameter ε . Note again that these transformations correspond to the expansion of frequency (or time) as described in Eq. (2.22) in the singular perturbation methods and allow us to introduce the two different time scales. Applying these transformations into the field equation (2.47), we have

$$\left(\varepsilon \frac{\partial^2}{\partial \xi^2} - 2\varepsilon^2 \frac{\partial^2}{\partial \xi \partial \tau} + \varepsilon^3 \frac{\partial^2}{\partial \tau^2}\right) \left\{\bar{I} + \frac{\bar{I}^3}{6}\right\} = \left(\varepsilon \frac{\partial^2}{\partial \xi^2} + \frac{1}{12}\varepsilon^2 \frac{\partial^4}{\partial \xi^4}\right) \bar{I}. \quad (2.54)$$

Next, let us consider how to describe the nonlinear effects by the parameter ε . We assume that the normalized current \bar{I} is expanded in a power series of a small parameter ε , in order to include nonlinearity perturbatively as follows,

$$\bar{I} = \varepsilon^s \bar{I}^{(1)} + \varepsilon^{2s} \bar{I}^{(2)} + \varepsilon^{3s} \bar{I}^{(3)} + \dots. \quad (2.55)$$

The order s of ε is determined so that the dispersive and nonlinear terms are balanced. We substitute Eq. (2.55) into Eq. (2.54) and obtain

$$\frac{1}{6}\varepsilon^{1+3s}\frac{\partial^2(\bar{I}^{(1)})^3}{\partial\xi^2} - 2\varepsilon^{2+s}\frac{\partial^2\bar{I}^{(1)}}{\partial\xi\partial\tau} = \frac{1}{12}\varepsilon^{2+s}\frac{\partial^4\bar{I}^{(1)}}{\partial\xi^4}, \quad (2.56)$$

where we write only for the lowest possible terms. The dispersion and nonlinearity are balanced at $1 + 3s = 2 + s$, i.e. $s = 1/2$. Introducing the expansion Eq. (2.55) with $s = 1/2$ into Eq. (2.54) and setting the coefficients of similar powers equal to zero, we obtain a set of differential equations. For $\varepsilon^{\frac{5}{2}}$,

$$2\frac{\partial^2\bar{I}^{(1)}}{\partial\xi\partial\tau} - \frac{1}{6}\frac{\partial^2(\bar{I}^{(1)})^3}{\partial\xi^2} + \frac{1}{12}\frac{\partial^4\bar{I}^{(1)}}{\partial\xi^4} = 0. \quad (2.57)$$

From the integration of Eq. (2.57) with respect to ξ , we get

$$2\frac{\partial\bar{I}^{(1)}}{\partial\tau} - \frac{1}{6}\frac{\partial(\bar{I}^{(1)})^3}{\partial\xi} + \frac{1}{12}\frac{\partial^3\bar{I}^{(1)}}{\partial\xi^3} = g(\tau), \quad (2.58)$$

where $g(\tau)$ is an arbitrary function of its argument and can be chosen to be zero like

$$2\frac{\partial\bar{I}^{(1)}}{\partial\tau} - \frac{1}{2}(\bar{I}^{(1)})^2\frac{\partial\bar{I}^{(1)}}{\partial\xi} + \frac{1}{12}\frac{\partial^3\bar{I}^{(1)}}{\partial\xi^3} = 0. \quad (2.59)$$

By re-scaling our coordinates as $\bar{I}^{(1)} = 2u$, $\xi = \bar{\xi}/2$ and $\tau = 3\bar{\tau}$, this finally reduces to the modified Korteweg-de Vries equation with a *negative* nonlinear term [34]

$$\frac{\partial u}{\partial\bar{\tau}} - 6u^2\frac{\partial u}{\partial\bar{\xi}} + \frac{\partial^3 u}{\partial\bar{\xi}^3} = 0. \quad (2.60)$$

This equation is specifically called defocusing mKdV, or mKdV⁻ because the sign of the nonlinear term is negative. The difference in the sign of the nonlinear term in the KdV equation only changes its polarity, and no significant changes appear in the soliton solution. In contrast, the difference in the sign of the nonlinear term in the mKdV equation makes a drastic change. The mKdV⁻ produces an entirely new solution set shown below.

Unlike the mKdV⁺ equation, the mKdV⁻ equation has kink (or shock-wave-type) traveling wave solutions of the form [34, 35]

$$u(\bar{\xi}, \bar{\tau}) = \alpha \tanh(\alpha\bar{\xi} + 2\alpha^3\bar{\tau}), \quad (2.61)$$

where the parameter α characterizes solitons like amplitude α and velocity $(-2\alpha^2)$. Figure 2.3 represents the solution of the soliton and the antisoliton. In terms of electric current in the system, the normalized current soliton in the $\bar{x} - \bar{t}$ coordinate is given as

$$\begin{aligned} \bar{I}(\bar{x}, \bar{t}) &= 2\alpha\sqrt{\varepsilon} \tanh\left[2\alpha\sqrt{\varepsilon}\left\{\bar{x} - \left(1 - \frac{(\alpha\sqrt{\varepsilon})^2}{3}\right)\bar{t}\right\}\right] \\ &= 2\sqrt{3(1-\bar{v}_s)}\tanh\left[2\sqrt{3(1-\bar{v}_s)}\{\bar{x} - \bar{v}_s\bar{t}\}\right], \end{aligned} \quad (2.62)$$

where \bar{v}_s stands for the normalized soliton velocity in the $\bar{x} - \bar{t}$ coordinate ($\bar{v}_s = 1 - \alpha'^2/3$) and $\alpha' = \alpha\sqrt{\varepsilon}$. This is exactly in agreement with the numerical results in the previous studies [36, 37]. Thus, we succeeded in demonstrating analytically the existence of shock-wave-type solutions in the superconducting circuits that have not been solved for many years. Note that the smaller shock-wave type soliton moves more rapidly than the larger one, contrary to the solitons of both KdV and mKdV⁺ equations. In addition, discrete treatment might be required for detailed analysis when the soliton speed is slow since the soliton width d approaches the lattice spacing a .

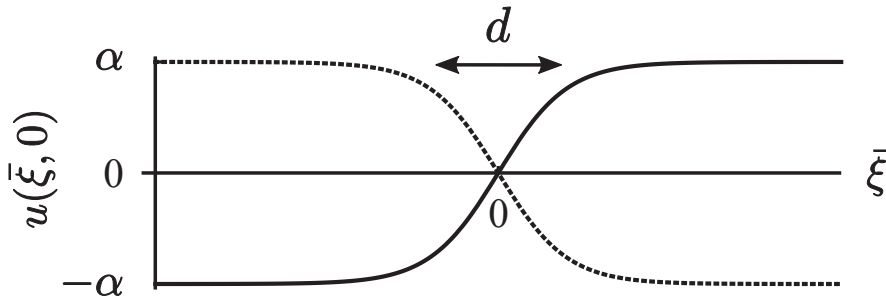


Figure 2.3: Schematic diagram of a soliton represented by the solid line and antisoliton indicated by the dotted line in the comoving frame $\bar{\xi}$. The amplitude and the width are given by α and d , respectively.

2.4 Solitons in nonlinear LC transmission lines

In this section, we analytically derive the soliton in the nonlinear LC transmission lines with nonlinear capacitors. We show the circuit model for the nonlinear LC transmission lines and derive the circuit equation. We also explore the waves hidden in it.

2.4.1 Model

Here, let us consider the LC transmission lines with a *nonlinear* capacitor as shown in Fig. 2.4. We assume that the inductors have an identical fixed inductance L , while the capacitors have nonlinear dependence on the voltage $C(V)$.

Nonlinear capacitor

Let us suppose nonlinear capacitors like varicap diodes. A p-n diode is composed of p-type and n-type semiconductors. A p-type and n-type semiconductor are created by adding impurities called acceptor and donor into an intrinsic semiconductor, respectively. A donor (acceptor) is an atom with one more (less) valence electrons than one of the intrinsic atoms and then supplies an electron (hole) into the semiconductor. A p-n junction has the depletion layer where there are no carriers but ions of donor and acceptor impurities due to the cancellation of the electrons and holes as shown in Fig. 2.5 (a). In forward bias, the electrons in the n-type region and the holes in the p-type region are pushed toward the junction and the depletion becomes neutralized zone, reducing its width as shown in Fig. 2.5 (b). On the other hand, in reverse bias, the electrons in the n-type region and the holes in the p-type region are pulled away from the junction, and the width of the depletion

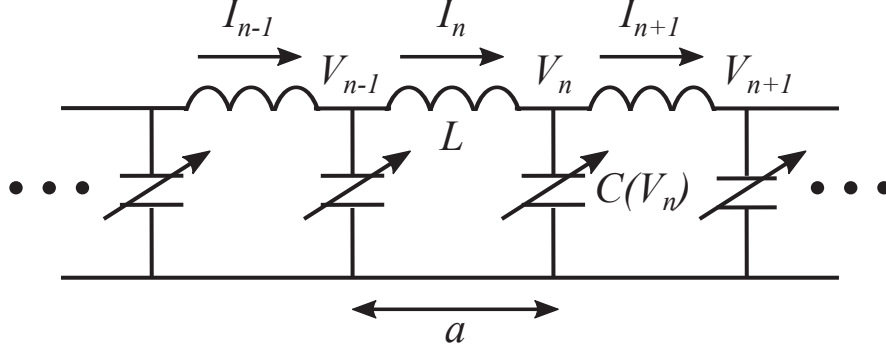


Figure 2.4: The nonlinear LC transmission line consisting of the constant inductance L and the nonlinear capacitance depending on the voltage $C(V_n)$. The unit cell length is denoted by a . The current and the voltage on the n th unit cell are I_n and V_n , respectively.

layer increases as shown in Fig. 2.5 (c). In this case, a diode behaves as a conductor because very little current flows. The varicap diode is used in the reverse bias and its capacitance is dependent on the applied voltage.

In general, capacitance is defined by

$$C(V) = \frac{\Delta Q}{\Delta V}, \quad (2.63)$$

where ΔQ and ΔV represent the variations in charge in the depletion layer and voltage, respectively. The variation on the charge ΔQ is given by

$$\Delta Q = qN_D \Delta x_n, \quad (2.64)$$

where q is the charge per a donor ion, N_D is the density of donor ions, x_n is the width of the depletion layer of the n-side, and Δx_n is its changes. The width x_n depends on the applied voltage as

$$x_n(V) = \sqrt{\frac{2\varepsilon}{qN_D} \frac{N_A}{N_A + N_D} (V_0 + V)}, \quad (2.65)$$

where N_A is the acceptor ion density, V_0 is built-in voltage and ε is the permittivity. The width when further applied ΔV is approximated as

$$\begin{aligned} x_n(V + \Delta V) &= \sqrt{\frac{2\varepsilon}{qN_D} \frac{N_A}{N_A + N_D} (V_0 + V)} \sqrt{1 + \frac{\Delta V}{V_0 + V}} \\ &\simeq x_{n0} \left(1 + \frac{1}{2} \frac{\Delta V}{V_0 + V} \right), \end{aligned} \quad (2.66)$$

where

$$x_{n0} = \sqrt{\frac{2\varepsilon}{qN_D} \frac{N_A}{N_A + N_D} (V_0 + V)}. \quad (2.67)$$

Then we obtain the changes in the width

$$\Delta x_n(\Delta V) = \frac{x_{n0}}{2} \frac{\Delta V}{V_0 + V}. \quad (2.68)$$

From Eq. (2.63), the capacitance is derived as [38]

$$C(V) = C_0 \frac{V_0}{V_0 + V}, \quad (2.69)$$

where C_0 is the characteristic capacitance such that $C_0 V_0 = qN_D x_{n0}/2$. The capacitance has a nonlinear dependence on the voltage V .

Circuit equation

Now let us derive the circuit equation. From Faraday's law, the voltage applied to the n th inductor with inductance L is given by

$$V_n - V_{n-1} = -L \frac{dI_n}{dt}, \quad (2.70)$$

where V_n is the voltage applied to the n th capacitor and I_n is the current flowing n th inductor. We obtain

$$\frac{d}{dt} (I_{n+1} - I_n) = -\frac{1}{L} (V_{n+1} - 2V_n + V_{n-1}), \quad (2.71)$$

by taking the difference with the equation for the $(n + 1)$ th inductor. From Kirchhoff's law, we obtain

$$I_{n+1} - I_n = -\frac{d}{dt} \{C(V_n)V_n\}. \quad (2.72)$$

Substituting Eq. (2.72) for Eq. (2.71), we obtain the circuit equation

$$\frac{d^2}{dt^2} \{C(V_n)V_n\} - \frac{1}{L} (V_{n+1} - 2V_n + V_{n-1}) = 0. \quad (2.73)$$

Note that the nonlinear capacitance can be expanded as

$$C(V_n) = C_0 (1 - \alpha V_n + \beta V_n^2 - \dots), \quad (2.74)$$

where $\alpha = 1/V_0$ and $\beta = 1/V_0^2$ are positive parameters.

2.4.2 Nonlinear Schrödinger Soliton

Now let us explore the waves hidden in our circuit using the discrete reductive perturbation method [32, 39–43], which allows us to extract the waves balancing the nonlinearity and the dispersion from the circuit equation (2.73) as in the previous section. The discrete reductive perturbation method starts by introducing the stretched variables as follows.

$$\begin{cases} \xi = \varepsilon (an - v_g t) \\ \tau = \varepsilon^2 t, \end{cases} \quad (2.75)$$

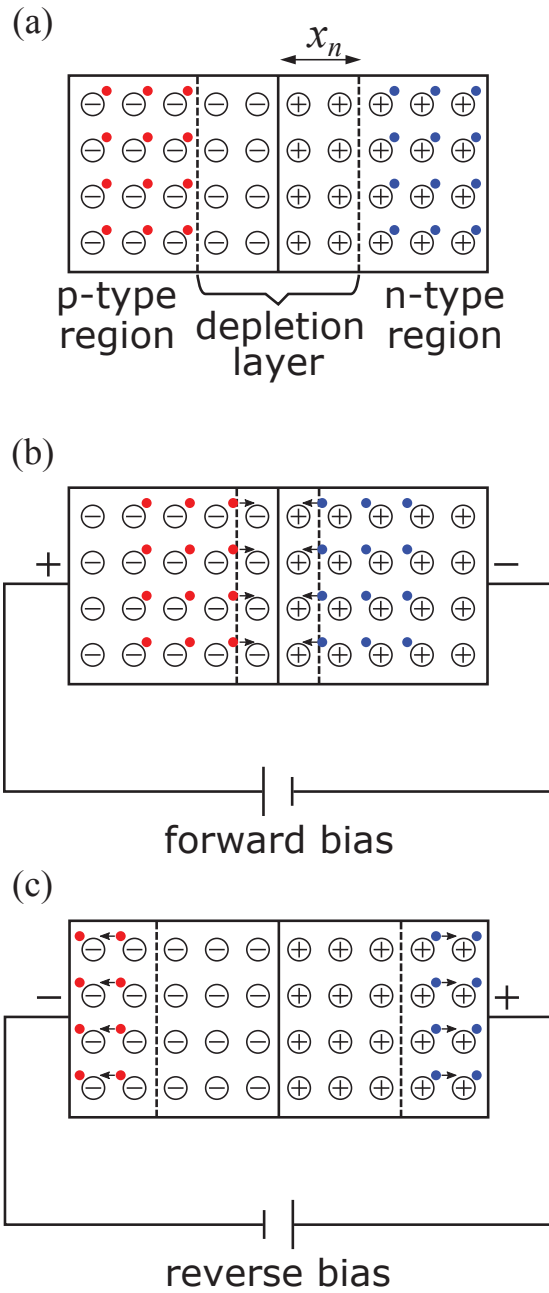


Figure 2.5: (a) Schematic diagram of a p-n junction composed of p-type and n-type semiconductors. There are the donor ions represented by circled plus signs and electrons indicated by the blue circles in n-type semiconductors, while there are the acceptor ions respected circled minus signs and holes indicated by the red circles in p-type semiconductors. Electrons and holes at the interface combine to form a carrier-free layer (depletion layer). (b) The electrons in the n-type region and the holes in the p-type region come into the depletion layer and they are combined, resulting in the reduction of the depletion layer when applied the forward bias. (c) In reverse bias, the electrons in the n-type region and holes in the p-type region go to the electrode, resulting in expansion of the depletion layer.

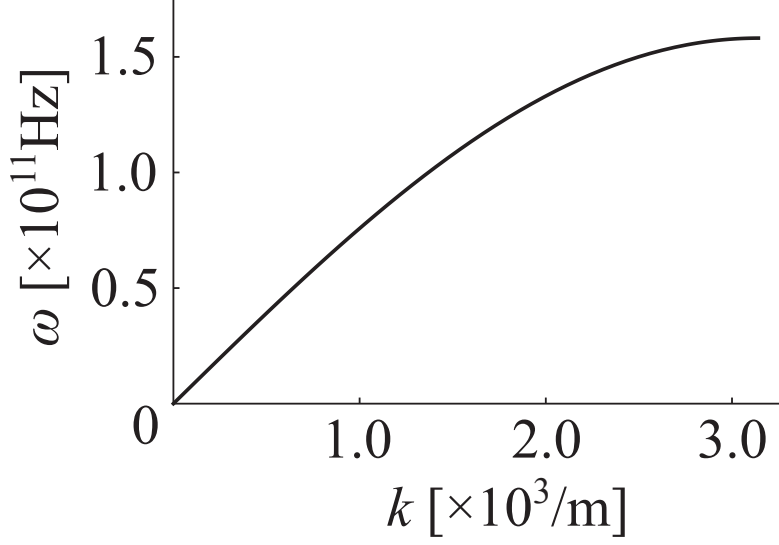


Figure 2.6: Diagram of dispersion relation in our system. We set the circuit parameters to $a = 10^{-3}\text{m}$, $L = 0.4 \times 10^{-9}\text{H}$, and $C_0 = 0.4 \times 10^{-12}\text{F}$.

where ε is a small dimensionless parameter ($0 < \varepsilon \ll 1$) and v_g represents the group velocity. The order of ε is determined in the same way as described in the previous section. These transformations extract slowly varying waves in comoving frames with group velocities v_g from the circuit equations. We also expand the voltage as [33],

$$V_n = V^{(0)} + \sum_{l=-\infty}^{+\infty} \sum_{\alpha=1} \varepsilon^\alpha V_l^{(\alpha)}(\xi, \tau) \exp[i l (kan - \omega t)], \quad (2.76)$$

where the rapidly varying phase $i(kan - \omega t)$ preserves the discrete character of the system even in slow varying frames. We restrict our analysis to the so-called rotating-wave approximation that consists essentially of neglecting higher harmonics:

$$V_n(t) \simeq \varepsilon V_1^{(1)}(\xi, \tau) \exp[i(kan - \omega t)] + \varepsilon V_1^{*(1)}(\xi, \tau) \exp[-i(kan - \omega t)]. \quad (2.77)$$

Substituting Eqs. (2.75) and (2.77) into Eq. (2.73) (the circuit equation), we obtain some important formulae for each ε order.

For the $\varepsilon e^{i(kan - \omega t)}$ order, the dispersion relation in our system is obtained as

$$\omega = \pm \frac{2}{\sqrt{LC_0}} \sin \frac{ka}{2}, \quad (2.78)$$

as shown in Fig. 2.6. This is because this lowest order corresponds to non-perturbative linear waves.

For the $\varepsilon^2 e^{i(kan - \omega t)}$ order, the group velocity that matches the expression from the definition $v_g = \partial\omega/\partial k$ is also derived as

$$v_g = \frac{1}{\omega} \frac{a}{LC_0} \sin ka = \pm v_0 \cos \frac{ka}{2}, \quad (2.79)$$

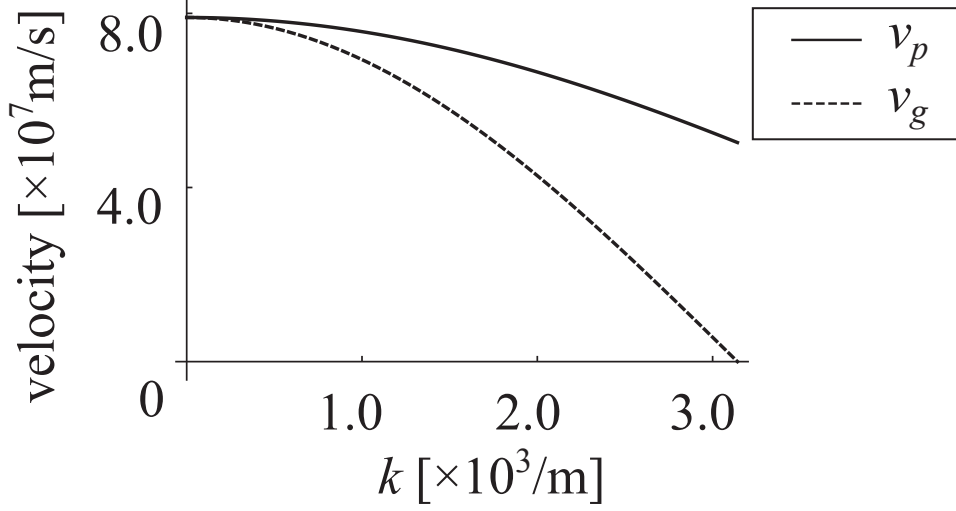


Figure 2.7: Phase velocity v_p (solid line) and group velocity v_g (dashed line) as a function of wavenumber k . The circuit parameter values are the same as in Fig. 2.6. The phase velocity is always larger than the group velocity.

with $v_0 = a/\sqrt{LC_0}$. As a result, our system has a normal dispersion, since the phase velocity

$$v_p = \frac{\omega}{k} = \pm v_0 \frac{2}{ka} \sin \frac{ka}{2}, \quad (2.80)$$

is always larger than the group velocity v_g in our system as shown in Fig. 2.7. For this order, nonlinear effects are not yet involved.

Finally, we also derive the desired nonlinear evolution equation, the so-called nonlinear Schrödinger equation, for the $\varepsilon^3 e^{i(kan - \omega t)}$ order, as

$$i \frac{\partial V_1^{(1)}}{\partial \tau} + P \frac{\partial^2 V_1^{(1)}}{\partial \xi^2} + Q V_1^{(1)} |V_1^{(1)}|^2 = 0, \quad (2.81)$$

where

$$P = \frac{1}{2\omega} \left(\frac{a^2}{LC_0} \cos ka - v_g^2 \right) = \mp \frac{a}{4} v_0 \sin \frac{ka}{2}, \quad (2.82)$$

$$Q = \frac{3\beta\omega}{2} = \pm \frac{3\beta}{\sqrt{LC_0}} \sin \frac{ka}{2}. \quad (2.83)$$

The coefficient P represents the group velocity *dispersion* and has the well-known relation expressed as

$$P = \frac{1}{2} \frac{dv_g}{dk}. \quad (2.84)$$

Thus, by this method, a complex nonlinear equation (2.73) can be reduced to a simple nonlinear equation (2.81) by reducing its order.

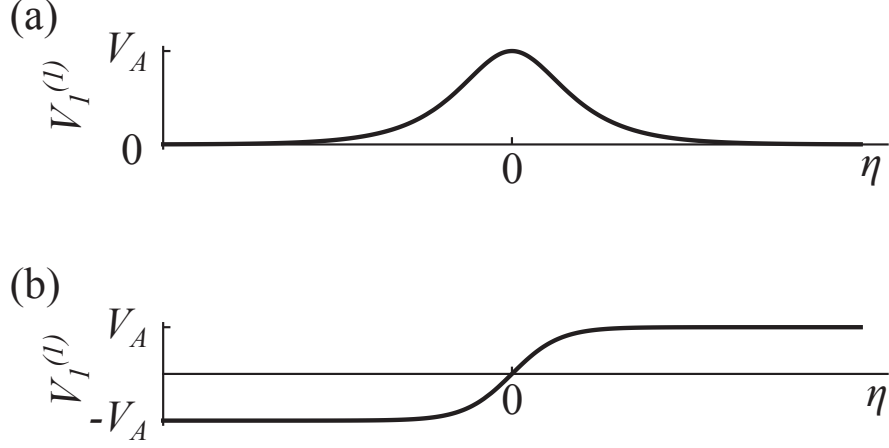


Figure 2.8: Schematic diagram of (a) a bright soliton and (b) a dark soliton in the comoving frame η described by Eqs. (2.85) and (2.86), respectively. The amplitude is represented by V_A .

The nonlinear Schrödinger equation has the soliton solutions depending on the sign of the product PQ . The bright soliton

$$V_1^{(1)} = V_A \operatorname{sech} \left(V_A \sqrt{\left| \frac{Q}{2P} \right|} (\xi - u\tau) \right) e^{i(k\xi - \omega\tau)}, \quad (2.85)$$

is formed when $PQ > 0$ and the dark soliton

$$V_1^{(1)} = V_A \tanh \left(V_A \sqrt{\left| \frac{Q}{2P} \right|} (\xi - u\tau) \right) e^{i(k\xi - \omega\tau)}, \quad (2.86)$$

is obtained when $PQ < 0$, where V_A is the amplitude and u is the relative velocity of the soliton in the $\xi - \tau$ coordinates as shown in Fig. 2.8. In our system, the product is given by

$$PQ = -\frac{3\beta}{4} v_0^2 \sin^2 \frac{ka}{2}, \quad (2.87)$$

so the sign is always negative ($PQ < 0$), and then the dark solitons are admitted. The soliton width is written by $w = 2 \operatorname{arccosh}(\sqrt{2}) \sqrt{|2P/Q|}/A$, where $\sqrt{|2P/Q|} = aV_0/\sqrt{6}$. This will be used later to evaluate the validity of the continuum approximation.

2.5 Summary

In this chapter, we have devised new types of transmission lines that contain nonlinear elements and have shown that current or voltage solitons exist there. Specifically, we have considered two types of transmission lines that are dual to each other: one has a nonlinear inductance and the other has a nonlinear capacitance. The nonlinear evolution equation has been derived from each of the circuit equations by using the reductive perturbation method. One is the modified Koreteweg-de Vries equation for nonlinear inductance transmission lines and the other is the nonlinear Schrödinger equation for nonlinear capacitance transmission lines. In the next chapter, we will discuss how these solitons behave as analogue black holes.

Chapter 3

Analogue black holes

In this chapter, we discuss the analogue black holes with the solitons in electric circuits discussed in the previous chapter based on the idea by Unruh et al. [7]. Please remember the model of carp swimming at a waterfall as discussed in chapter 1. In our proposals, the electromagnetic wave and soliton play the roles of the carp and waterfall, respectively. The velocity of electromagnetic waves propagating in transmission lines is given by $v = a/\sqrt{LC}$ as described in Section 3.1. We can modify the velocity of electromagnetic waves through the nonlinearity of inductance or capacitance. Note that the velocity of the electromagnetic wave changes spatially while the soliton velocity is a constant. This means that the carp in our system swim at spatially varying velocity, while the water in the river flows at a *constant* speed, unlike the sonic black holes by Unruh et al. [7]. Despite the differences in these roles, the same situation is realized in our systems, and both systems have the same spacetime metric as the real black holes. Comparing the metric, the event horizons of analogue black holes appear where the velocity of the electromagnetic wave is equal to the velocity of the reference wave, i.e., the soliton.

This chapter is organized as follows: we first describe how the electromagnetic waves propagate on transmission lines in Section 3.1. Then, we propose analogue black holes in transmission lines with nonlinear inductors in Section 3.2 and nonlinear capacitors in Section 3.3 by deriving the spatial varying velocity of the electromagnetic waves. We also show that the metric of our systems is similar to that of an actual black hole.

3.1 Velocity of electromagnetic waves on transmission lines

Here we briefly review the LC transmission lines. The LC circuit indicated in Fig. 3.1 (a) consists of an inductor and a capacitor describing the magnetic field and the electric field, respectively. This is a fundamental component of the electric circuit. The electromagnetic waves are generated by the variation of magnetic field and electric field in the LC circuit. The LC transmission line represented in Fig. 3.1 (b) is formed by the array of the LC circuit and the electromagnetic waves propagate through it. Suppose that inductance L_0 and capacitance C_0 are constant, the circuit equation is derived as follows. From Faraday's law, the voltage applied to the n th inductor is derived by

$$V_n - V_{n-1} = -L_0 \frac{dI_n}{dt}, \quad (3.1)$$

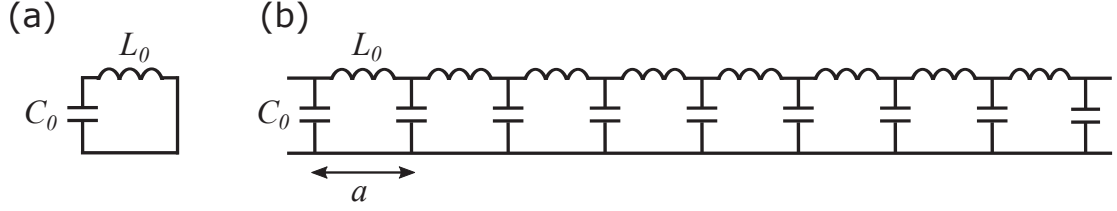


Figure 3.1: (a) LC circuit composed of an inductor and a capacitor is a fundamental component in electric circuits. (b) An LC transmission line is formed by connecting the LC circuit as the fundamental component. All inductors and capacitors have identical fixed inductance L_0 and C_0 , respectively, and the length of the unit cell is a . The electromagnetic waves propagate through the LC transmission line with the velocity $v = a/\sqrt{L_0C_0}$.

where V_n is the voltage applied to the n th capacitor and I_n is the current flowing through the n th inductor. We obtain

$$\frac{d}{dt}(I_{n+1} - I_n) = -\frac{1}{L_0}(V_{n+1} - 2V_n + V_{n-1}), \quad (3.2)$$

by taking the difference with the equation for the $(n + 1)$ th inductor. From Kirchhoff's law, we obtain

$$I_{n+1} - I_n = -\frac{d}{dt}C_0V_n. \quad (3.3)$$

The circuit equation is given by

$$\frac{d^2V_n}{dt^2} - \frac{1}{L_0C_0}(V_{n+1} - 2V_n + V_{n-1}) = 0, \quad (3.4)$$

by substituting Eq. (3.3) for Eq. (3.2). This equation is equivalent to the equation for lattice vibration with a linear coupling constant. We can apply it to the continuum approximation $V_n \equiv V(x, t)$ under the condition of unit cell length $a \ll 1$ and perform Taylor expansion as

$$\begin{aligned} V_{n\pm 1}(t) &= V(x \pm a, t) \\ &= V \pm a \frac{\partial V}{\partial x} + \frac{a^2}{2!} \frac{\partial^2 V}{\partial x^2} \pm \frac{a^3}{3!} \frac{\partial^3 V}{\partial x^3} + O(a^4), \end{aligned} \quad (3.5)$$

to obtain the wave equation. Equation (3.4) leads to

$$\frac{\partial^2 V}{\partial t^2} = \frac{2}{L_0C_0} \sum_{m=1}^{\infty} \frac{a^{2m}}{(2m)!} \frac{\partial^{2m} V}{\partial x^{2m}}. \quad (3.6)$$

Substituting the plane wave solution $V = \exp\{i(kx - \omega t)\}$, the dispersion relation in these transmission lines is given as

$$\omega = \pm \frac{2}{\sqrt{L_0C_0}} \sin \frac{ka}{2}, \quad (3.7)$$

as shown in Fig. 3.2. If there are multiple modes with various wavenumbers or frequencies, a wave packet composed of waves with various frequencies moves with the group velocity. The phase velocity and the group velocity are given by

$$v_p = \frac{\omega}{k} = \frac{a}{k\sqrt{L_0C_0}} \sin \frac{ka}{2}, \quad (3.8)$$

and

$$v_g = \frac{d\omega}{dk} = \frac{a}{\sqrt{L_0C_0}} \cos \frac{ka}{2}, \quad (3.9)$$

respectively. In the long-wavelength approximation, the dispersion relation Eq. (3.7) reduces to

$$\omega(k) = v_0k, \quad (3.10)$$

where there are no dispersion, i.e., $v_p = v_g = v_0$ with

$$v_0 = \frac{a}{\sqrt{L_0C_0}}. \quad (3.11)$$

The velocity of electromagnetic waves propagating on the transmission lines depends on both inductance and capacitance. Equation (3.6) becomes the well-known wave equation

$$\frac{\partial^2 V}{\partial t^2} = v_0^2 \frac{\partial^2 V}{\partial x^2}. \quad (3.12)$$

We restrict our analysis to a single mode with a small wavenumber when we consider analogue horizons. If both or either of the capacitor and inductance is nonlinear, the velocity of electromagnetic waves is no longer a constant as follows,

$$v = \frac{a}{\sqrt{L(I)C(V)}}. \quad (3.13)$$

Therefore, the velocity is modulated if either of the inductance or capacitance are not constants. In this paper, we propose two different types of systems with nonlinear inductance and capacitance for analogue black holes.

3.2 Analogue black holes in Josephson transmissions lines

Firstly, we propose analogue black holes in the Josephson transmission line with a nonlinear inductor as discussed in Section 2.3. The effective geometry of our analogue black holes is derived as follows. By defining the potential A_n as

$$V_n = A_{n+1} - A_n, \quad (3.14)$$

$$I_n = -C \frac{d}{dt} A_n. \quad (3.15)$$

By using these definitions, these circuit equations

$$I_n - I_{n-1} = C \frac{dV_n}{dt}, \quad (3.16)$$

$$V_{n+1} - V_n = L_n \frac{dI_n}{dt}, \quad (3.17)$$

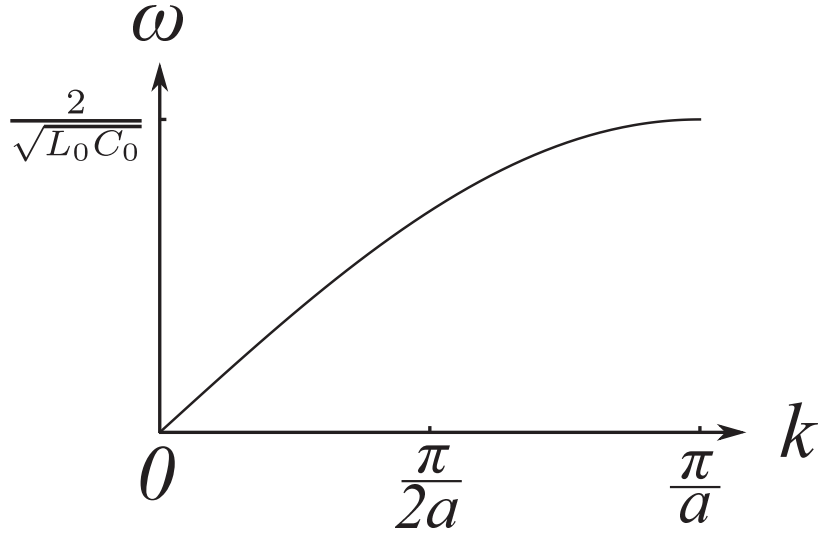


Figure 3.2: Schematic diagram of the dispersion relation in the LC transmission line.

become

$$A_{n+1} - 2A_n + A_{n-1} = \frac{d}{dt}LC \frac{d}{dt}A_n. \quad (3.18)$$

In the continuum approximation, we obtain the wave equation for the potential A as

$$\left(\frac{\partial}{\partial t} \frac{1}{v^2(x,t)} \frac{\partial}{\partial t} - \frac{\partial^2}{\partial x^2} \right) A = 0. \quad (3.19)$$

The velocity of electromagnetic waves is then given as

$$v(x,t) = \frac{a}{\sqrt{L(\bar{I})C}} = v_0 \sqrt{\cos(\arcsin \bar{I}(x,t))}, \quad (3.20)$$

where $v_0 = a/\sqrt{L_J C}$. Since the current soliton depends on the position, the velocity of the electromagnetic wave is modulated in space as

$$v(\bar{x}, \bar{t}) = v_0 \sqrt{\cos[\arcsin\{2\alpha' \tanh\{2\alpha'(\bar{x} - \bar{v}_s \bar{t})\}\}]}. \quad (3.21)$$

The soliton parameter α' is restricted to $|\alpha'| \leq 1/2$ due to the range $-1 \leq x \leq 1$ of the inverse sine function ($\arcsin(x)$). Equation (3.21) is rewritten by

$$\bar{v}(\bar{x}, \bar{t}) = \left[1 - 12(1 - \bar{v}_s) \tanh^2 \left\{ 2\sqrt{3(1 - \bar{v}_s)} (\bar{x} - \bar{v}_s \bar{t}) \right\} \right]^{\frac{1}{4}}, \quad (3.22)$$

where $\bar{v}(\bar{x}, \bar{t})$ is the normalized velocity of the electromagnetic wave, i.e., $\bar{v}(\bar{x}, \bar{t}) = v(\bar{x}, \bar{t})/v_0$, in the Josephson transmission lines.

In this system, the electromagnetic wave and soliton play the roles of the carp and waterfall, respectively. Note that the velocity of the electromagnetic wave changes spatially while the soliton velocity is a constant. This means that the carp in our system swim at spatially varying velocities,

while the water in the river flows at a constant velocity. In the comoving frame with the soliton velocity v_s , it becomes

$$\left[\left(\frac{\partial}{\partial \tau} - v_s \frac{\partial}{\partial \eta} \right) \frac{1}{v^2(\eta)} \left(\frac{\partial}{\partial \tau} - v_s \frac{\partial}{\partial \eta} \right) - \frac{\partial^2}{\partial \eta^2} \right] A = 0, \quad (3.23)$$

where $\eta = x - v_s t$ and $\tau = t$. The inverse of the metric matrix $g^{\mu\nu}$ is defined as

$$\left(\begin{array}{cc} \partial_\tau & \partial_\eta \end{array} \right) g^{\mu\nu} \left(\begin{array}{c} \partial_\tau \\ \partial_\eta \end{array} \right) A = 0, \quad (3.24)$$

where

$$g^{\mu\nu} = -\frac{1}{v^2(\eta)} \left(\begin{array}{cc} 1 & -v_s \\ -v_s & v_s^2 - v^2(\eta) \end{array} \right). \quad (3.25)$$

Therefore the metric matrix is derived as

$$g_{\mu\nu} = (g^{\mu\nu})^{-1} = \left(\begin{array}{cc} v_s^2 - v^2(\eta) & v_s \\ v_s & 1 \end{array} \right). \quad (3.26)$$

The metric for this system is given as

$$ds^2 = - (v^2(\eta) - v_s^2) dt^2 + 2v_s dt dx + dx^2, \quad (3.27)$$

which is the same form as the metric of acoustic analogue black hole Eq. (1.16). This implies that the velocity of the carp is constant and the water flow varies spatially in an acoustic analogue black hole, whereas the velocity of the carp varies spatially and the water flow is constant in a soliton black hole.

Figure 3.3 shows the correlation diagram of a current soliton (b) and the velocity of the electromagnetic wave (c) in the Josephson transmission line (a). Two event horizons are formed due to the spatially varying velocities of the electromagnetic wave, leading to a pair of black holes and white holes as presented in nonlinear optical fibers [12]. The event horizons appear where the velocity of electromagnetic wave $\bar{v}(\bar{x}, \bar{t})$ is equal to the velocity of the reference wave, i.e., the normalized current soliton $\bar{v}_s = v_s/v_0$. The positions of the horizons are derived as

$$\bar{x}_h^\pm = \pm \frac{1}{2\sqrt{3(1-\bar{v}_s)}} \tanh^{-1} \left(\sqrt{\frac{(1+\bar{v}_s)(1+\bar{v}_s^2)}{12}} \right). \quad (3.28)$$

In short, the velocity of the current soliton determines the position of the event horizon. In our system, a pair of black holes and white holes occur within $11/12 \leq \bar{v}_s < 1$ as follows. The lower bound is given by the condition $|\alpha'| = |\sqrt{3(1-\bar{v}_s)}| \leq 1/2$ demonstrated above. This is also equivalent to the condition that the soliton width is larger than the lattice spacing. In other words, the continuum approximation is justified for soliton velocities greater than this. On the other hand, the upper bound is determined by the condition that the velocity of the soliton is smaller than the velocity of the electromagnetic wave v_0 .

The area behind the soliton corresponds to a black hole because the electromagnetic waves cannot overtake the soliton there, while the front side of the soliton is a white hole because the electromagnetic waves in solitons cannot propagate forward. The normal area between two horizons is determined by the shape of the soliton and cannot be freely changed. In the Appendix, we will propose a scheme to design the configuration of black holes on demand by combining solitons and antisolitons.

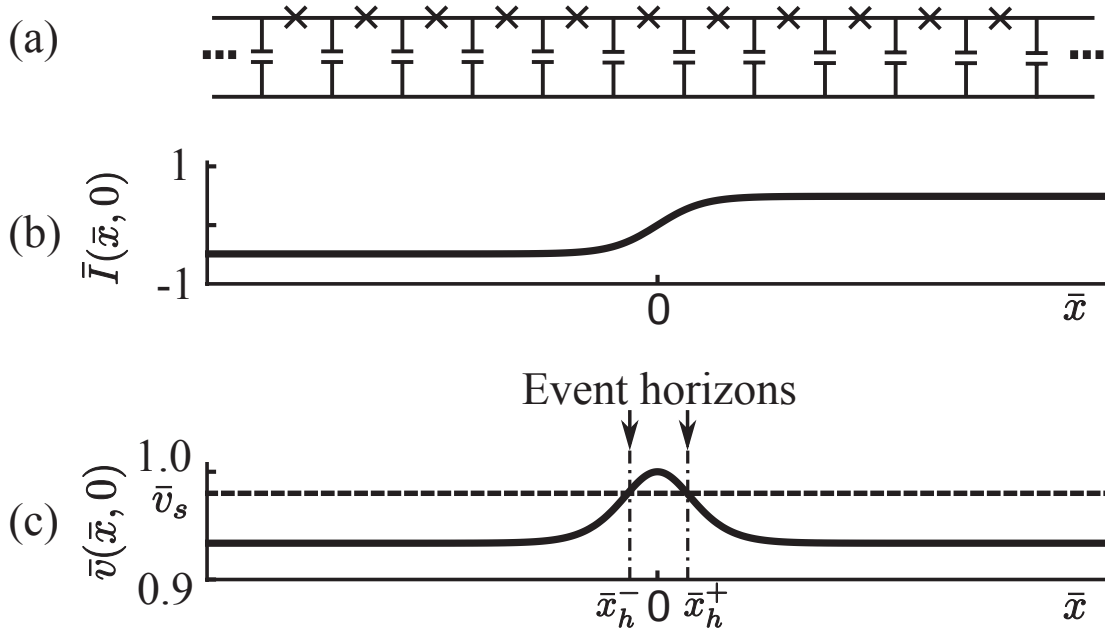


Figure 3.3: (a) Josephson transmission line, (b) shock-wave-type normalized current soliton at $\bar{t} = 0$ with the velocity $\bar{v}_s = 0.98$, (c) normalized velocity of the electromagnetic wave at $\bar{t} = 0$. The horizontal dotted line represents the normalized soliton velocity \bar{v}_s . x_h^- and x_h^+ indicate the black hole and white hole horizon positions, respectively.

3.3 Analogue black holes in nonlinear LC transmission lines

Next, we propose analogue black holes on the LC transmission line with *nonlinear capacitance* as discussed in Section 2.4. Now, we show that the velocity of the electromagnetic waves changes in space due to the voltage solitons. In LC transmission lines with nonlinear capacitance depending on the voltage expressed as

$$C(V) = C_0 \frac{V_0}{V_0 + V}, \quad (3.29)$$

the following two sets of circuit equations

$$I_{n+1} - I_n = -\frac{d}{dt} \{C(V_n) V_n\}, \quad (3.30)$$

$$V_n - V_{n-1} = -L \frac{dI_n}{dt}, \quad (3.31)$$

are given. The effective geometry of our analogue black holes is derived as follows in the procedures parallel to the previous section. By defining the potential A_n as

$$V_n = A_{n+1} - A_n, \quad (3.32)$$

$$I_n = -C \frac{d}{dt} A_n, \quad (3.33)$$

the integrated circuit equation is written as

$$A_{n+1} - 2A_n + A_{n-1} = \frac{d}{dt} LC \frac{d}{dt} A_n. \quad (3.34)$$

In a continuum approximation, we obtain

$$\left(\frac{\partial}{\partial t} \frac{1}{v^2(x,t)} \frac{\partial}{\partial t} - \frac{\partial^2}{\partial x^2} \right) A = 0, \quad (3.35)$$

where the velocity of electromagnetic waves depends on the voltage soliton $V_1^{(1)}$ and varies spatially as follows,

$$v(x,t) = \frac{a}{\sqrt{LC(V_1^{(1)})}} = v_0 \sqrt{1 + \frac{V_1^{(1)}(x,t)}{V_0}}, \quad (3.36)$$

where $v_0 = a/\sqrt{LC_0}$. The metric is described by

$$ds^2 = - (v^2(\eta) - v_s^2) dt^2 + 2v_s dt dx + dx^2, \quad (3.37)$$

as same as Eq. (3.27).

Figure 3.4 represents the correlation diagram of voltage soliton (b) and the velocity of the electromagnetic waves (c) in the nonlinear LC transmission lines (a). The horizon occurs where $g_{00} = 0$ in the metric matrix, i.e. $v^2(\eta) = v_s^2$. The position of the event horizon is given as

$$\eta_h = \frac{a}{\sqrt{6}} \frac{V_0}{V_A} \operatorname{arctanh} \left\{ \frac{V_0}{V_A} \left(\frac{v_s^2}{v_0^2} - 1 \right) \right\}. \quad (3.38)$$

The soliton velocity is restricted in the range between the minimum and maximum of $v_g(\eta)$ for the generation of the event horizon, i.e., $v_0 \sqrt{1 - V_A/V_0} \leq v_s \leq v_0 \sqrt{1 + V_A/V_0}$.

3.4 Summary

In this chapter, we have proposed the analogue black holes induced by the solitons in both Josephson transmission lines with nonlinear Josephson inductors and LC transmission lines with nonlinear capacitors. In electric circuits, analogue black holes are generated using electromagnetic waves with spatial varying velocities. The velocity of electromagnetic waves is changed in space due to the nonlinear inductance or capacitance depending on the current solitons or the voltage soliton, resulting in the analogue black holes. We have confirmed that the same metric as a Schwarzschild black hole has been realized. The number of horizons is different between our two systems due to the difference in dependencies of the nonlinear inductors or capacitors on current or voltage solitons. In the next chapter, we evaluate the observability of Hawking radiation on our systems by estimating the Hawking temperature.

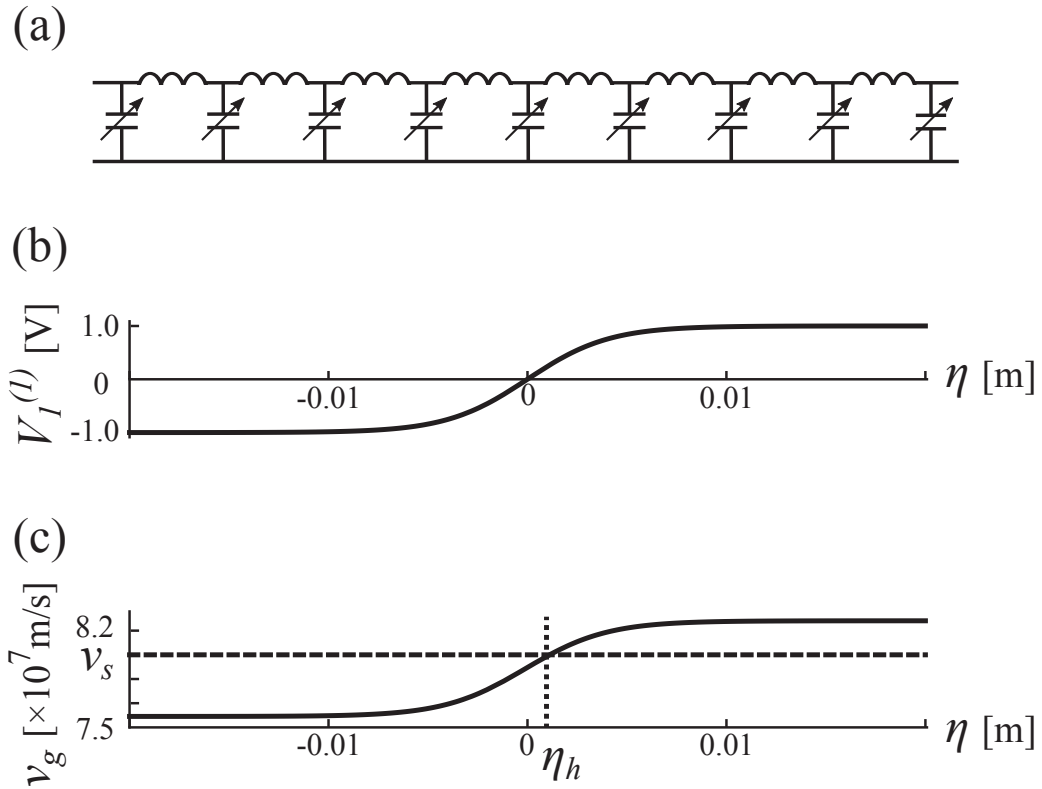


Figure 3.4: (a) Schematic diagram of the nonlinear transmission lines. (b) A voltage soliton $V_1^{(1)}$ in the comoving frame η . We set $V_A = 0.1\text{V}$ and $V_0 = 1\text{V}$, and the other circuit parameters are the same as in Fig. 2.6. The soliton width is about $w \sim 7a$. (c) The spatially varying group velocity of the electromagnetic waves in the comoving frame η for the wavenumber $k = 100/\text{m}$ with the same circuit parameters. The horizontal dashed line represents the soliton velocity v_s . The event horizon is formed at η_h , where $v_g^2 = v_s^2$.

Chapter 4

Analogue Hawking radiation

A black hole is an area of space where a gravitational field is so strong that no matter or radiation (including light) can escape. However, Hawking proposed that *virtual* particle-antiparticle pairs arising quantum-mechanically from a vacuum near the event horizon may result in one particle's escape as Hawking radiation in the vicinity of the black hole while the partner particle with negative energy falls into it before the pair annihilation can happen [4,44]. The Hawking temperature is an important measure to assessing the observability of Hawking radiation in our systems.

In this chapter, we derive the Hawking temperature by using the tunneling mechanism. We also estimate the Hawking temperature using the obtained formula in our analogue black holes and discuss the observability of Hawking radiation.

4.1 Tunneling mechanism

Now let us derive the general formula for the Hawking temperature to discuss the observability of Hawking radiation in our systems. In the previous papers [45], it was evaluated from the surface gravity of the effective horizon that depends on the rate of spatial change of the light velocity in the laboratory frame across the horizon. Here we employ the tunneling mechanism known as the radial null geodesic method [46,47]: a particle with the positive energy of virtual particle-antiparticle pairs tunnels through the event horizon toward the outside of the black hole.

Firstly, let us derive the tunneling probability in the semi-classical approximation. In the Wentzel-Kramer-Brillouin (WKB) approximation, we assume the wave function $\psi(x, t)$ as

$$\psi(x, t) = e^{-\frac{iEt}{\hbar}} u(x), \quad (4.1)$$

$$u(x) = e^{\frac{i}{\hbar}S}, \quad (4.2)$$

where S is the classical action of the trajectory. The tunneling probability Γ of the classically forbidden trajectory from the inside (x_{in}) to the outside (x_{out}) of the horizon, per unit time per

unit volume in the semi-classical approximation is given by the following formula,

$$\begin{aligned}
\Gamma &= |\psi(x, t)|^2 \\
&= |u(x)|^2 \\
&= \exp \left\{ \frac{1}{\hbar} (-i\Re S - \Im S) \right\} \exp \left\{ \frac{1}{\hbar} (i\Re S - \Im S) \right\} \\
&= \exp \left(-\frac{2\Im S}{\hbar} \right).
\end{aligned} \tag{4.3}$$

The classical action of the trajectory is defined by

$$S = \int L dt, \tag{4.4}$$

where Lagrangian is given as

$$L(x, \dot{x}) = p\dot{x} - H(x, p) \tag{4.5}$$

with Hamiltonian H and momentum p . The classical action is reduced to

$$\begin{aligned}
S &= \int (p\dot{x} - H(x, p)) dt \\
&= \int_{x_{in}}^{x_{out}} \int_0^p dp' dx - \int H(x, p) dt \\
&= \int_{x_{in}}^{x_{out}} \int_0^{E(t)} \frac{dH}{dx/dt} dx - \int H(x, p) dt,
\end{aligned} \tag{4.6}$$

where Hamilton's equation of motion $\dot{x} = dH/dp$ is used. To evaluate the imaginary part of the action, we need to express dx/dt concretely.

In the Painlevé-Gullstrand coordinates [11, 21], the metric of our systems is

$$ds^2 = -(v^2 - v_s^2) dt^2 + 2v_s dx dt + dx^2. \tag{4.7}$$

The radial null geodesic ($ds^2 = 0$) leads to

$$\left(\frac{dx}{dt} \right)^2 + 2v_s \frac{dx}{dt} - (v^2 - v_s^2) = 0. \tag{4.8}$$

The solution is then given as

$$\frac{dx}{dt} = -v_s \pm v, \tag{4.9}$$

where the positive (negative) sign in the second term of the right side represents the external (internal) mode. For the external mode, Eq. (4.6) is reduced to

$$S = \int_{x_{in}}^{x_{out}} \int_0^{E(t)} \frac{dH'}{v - v_s} dx - \int H(x, p) dt. \tag{4.10}$$

Hereafter the second term of this equation is ignored since it is real. Taylor expansion of $v(x, t)$ near the position of the event horizon x_h is written as

$$\begin{aligned} v(x, t) &= v(x_h, t) + \left. \frac{\partial v}{\partial x} \right|_{x=x_h} (x - x_h) + \mathcal{O}((x - x_h)^2) \\ &\simeq v_s + \left. \frac{\partial v}{\partial x} \right|_{x=x_h} (x - x_h), \end{aligned} \quad (4.11)$$

and then the action becomes

$$S \simeq - \frac{E(t)}{\left. \frac{\partial v}{\partial x} \right|_{x=x_h}} \int_{x_{in}}^{x_{out}} \frac{1}{x - x_h} dx. \quad (4.12)$$

This is impossible to integrate in the usual sense because there is a singular point x_h on the integral path.

Here, let us review the singular integral which can integrate even when the integrand has an infinite value at one or more points in the domain of integration. We consider the integral on the real axis as

$$\int_{-\infty}^{\infty} \frac{f(x)}{x - x_0} dx, \quad (4.13)$$

which is rewritten as the complex integral

$$\oint_C \frac{f(z)}{z - x_0} dz, \quad (4.14)$$

where the integral path C consists of the path on the real axis $-\infty < x < \infty$ and C_R which is the upper semicircle path centered on the origin with the radius $R \rightarrow \infty$. In this case, the singular point x_0 exists on the integral path, and it cannot be integrated in the usual sense. One of the approaches for solving this problem is modifying the integral path to avoid the singular point. We define upper semicircle clockwise path $C_{+\varepsilon}$ and lower semicircle counterclockwise path $C_{-\varepsilon}$ centered at the singular point with the radius ε as shown in Fig. 4.1. When the integral path is modulated into a path that excludes singular points through path $C_{+\varepsilon}$, the integral path becomes a closed path that does not include the singular points. The integral becomes 0 according to the residue theorem as

$$\int_{C_R} \frac{f(z)}{z - x_0} dz + \int_{-\infty}^{x-\varepsilon} \frac{f(x)}{x - x_0} dx + \int_{C_{+\varepsilon}} \frac{f(z)}{z - x_0} dz + \int_{x+\varepsilon}^{\infty} \frac{f(x)}{x - x_0} dx = 0. \quad (4.15)$$

On the other hand, when the integral path is deformed into the closed path through $C_{-\varepsilon}$, it includes the singular point and the integral becomes $2i\pi f(x_0)$ as

$$\int_{C_R} \frac{f(z)}{z - x_0} dz + \int_{-\infty}^{x-\varepsilon} \frac{f(x)}{x - x_0} dx + \int_{C_{-\varepsilon}} \frac{f(z)}{z - x_0} dz + \int_{x+\varepsilon}^{\infty} \frac{f(x)}{x - x_0} dx = 2i\pi f(x_0). \quad (4.16)$$

If $f(z)$ approaches zero quickly enough on C_R with $R \rightarrow \infty$, we obtain

$$\int_{C_R} \frac{f(z)}{z - x_0} dz = 0. \quad (4.17)$$

In the limit of $\varepsilon \rightarrow 0$, these equations are reduced to

$$\lim_{\varepsilon \rightarrow 0} \int_{C_{+\varepsilon}} \frac{f(z)}{z - x_0} dz + \lim_{\varepsilon \rightarrow 0} \left\{ \int_{-\infty}^{x-\varepsilon} \frac{f(x)}{x - x_0} dx + \int_{x+\varepsilon}^{\infty} \frac{f(x)}{x - x_0} dx \right\} = 0, \quad (4.18)$$

$$\lim_{\varepsilon \rightarrow 0} \int_{C_{-\varepsilon}} \frac{f(z)}{z - x_0} dz + \lim_{\varepsilon \rightarrow 0} \left\{ \int_{-\infty}^{x-\varepsilon} \frac{f(x)}{x - x_0} dx + \int_{x+\varepsilon}^{\infty} \frac{f(x)}{x - x_0} dx \right\} = 2i\pi f(x_0). \quad (4.19)$$

By changing the variable as $z = \varepsilon e^{i\theta} + x_0$, we obtain the following expressions

$$\begin{aligned} \lim_{\varepsilon \rightarrow 0} \int_{C_{+\varepsilon}} \frac{f(z)}{z - x_0} dz &= \lim_{\varepsilon \rightarrow 0} \int_{\pi}^0 \frac{f(\varepsilon e^{i\theta} + x_0)}{\varepsilon e^{i\theta}} i\varepsilon e^{i\theta} d\theta \\ &= \lim_{\varepsilon \rightarrow 0} i \int_{\pi}^0 f(\varepsilon e^{i\theta} + x_0) d\theta \\ &= i \int_{\pi}^0 f(x_0) d\theta \\ &= -i\pi f(x_0), \end{aligned} \quad (4.20)$$

$$\begin{aligned} \lim_{\varepsilon \rightarrow 0} \int_{C_{-\varepsilon}} \frac{f(z)}{z - x_0} dz &= \lim_{\varepsilon \rightarrow 0} \int_{\pi}^{2\pi} \frac{f(\varepsilon e^{i\theta} + x_0)}{\varepsilon e^{i\theta}} i\varepsilon e^{i\theta} d\theta \\ &= \lim_{\varepsilon \rightarrow 0} i \int_{\pi}^{2\pi} f(\varepsilon e^{i\theta} + x_0) d\theta \\ &= i \int_{\pi}^{2\pi} f(x_0) d\theta \\ &= i\pi f(x_0). \end{aligned} \quad (4.21)$$

Then, Eq. (4.18) and Eq. (4.19) reduce to

$$\lim_{\varepsilon \rightarrow 0} \left\{ \int_{-\infty}^{x-\varepsilon} \frac{f(x)}{x - x_0} dx + \int_{x+\varepsilon}^{\infty} \frac{f(x)}{x - x_0} dx \right\} = i\pi f(x_0), \quad (4.22)$$

where the term on the left hand is called Cauchy principal value represented by

$$\mathcal{P} \int_{-\infty}^{\infty} \frac{f(x)}{x - x_0} dx = \lim_{\varepsilon \rightarrow 0} \left\{ \int_{-\infty}^{x-\varepsilon} \frac{f(x)}{x - x_0} dx + \int_{x+\varepsilon}^{\infty} \frac{f(x)}{x - x_0} dx \right\}. \quad (4.23)$$

As a result, we obtain the expression

$$\mathcal{P} \int_{-\infty}^{\infty} \frac{f(x)}{x - x_0} dx = i\pi f(x_0). \quad (4.24)$$

So far, we have tried complex integral

$$\oint_C \frac{f(z)}{z - x_0} dz, \quad (4.25)$$

by transforming the integral path. Another coping method is to shift the singular point as shown in Fig. 4.2. If we shift the singular point by ε in the imaginary axis, the closed integral path does not include the singular point and we obtain

$$\oint_C \frac{f(z)}{z - x_0 - i\varepsilon} dz = \int_{-\infty}^{\infty} \frac{f(x)}{x - x_0 - i\varepsilon} dx = 2i\pi f(x_0). \quad (4.26)$$

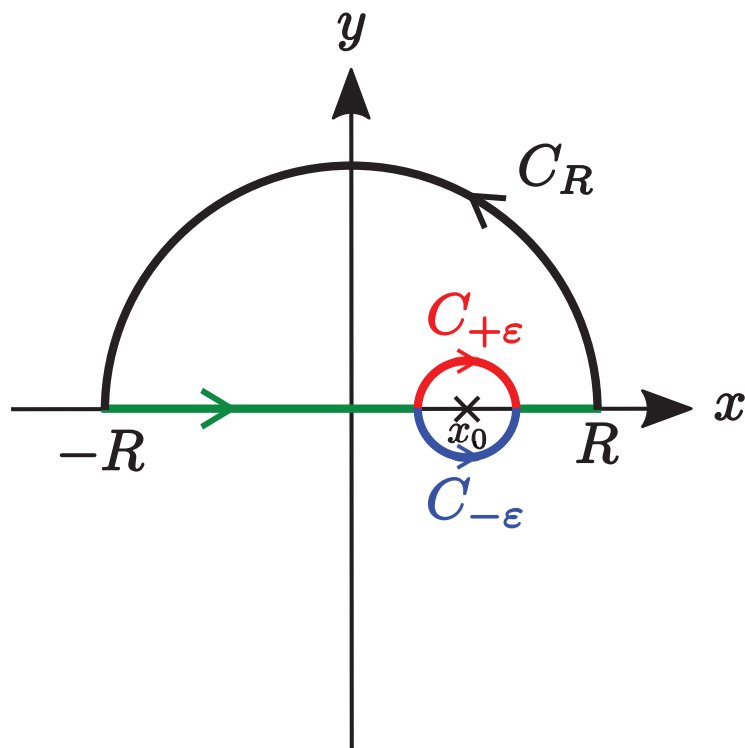


Figure 4.1: The integral path is modulated. C_R is the upper semicircle path centered on the origin with the radius $R \rightarrow \infty$. $C_{+\epsilon}$ and $C_{-\epsilon}$ are upper semicircle clockwise path and lower semicircle counterclockwise path, respectively.

On the other hand, if we shift the singular point by $-\varepsilon$ in the imaginary axis, the singular point is included in the closed integral path and we obtain

$$\oint_C \frac{f(z)}{z - x_0 + i\varepsilon} dz = \int_{-\infty}^{\infty} \frac{f(x)}{x - x_0 + i\varepsilon} dx = 0. \quad (4.27)$$

From Eq. (4.24), we obtain the Hilbert formula

$$\int_{-\infty}^{\infty} \frac{f(x)}{x - x_0 \mp i\varepsilon} dx = \mathcal{P} \int_{-\infty}^{\infty} \frac{f(x)}{x - x_0} dx \pm i\pi f(x_0). \quad (4.28)$$

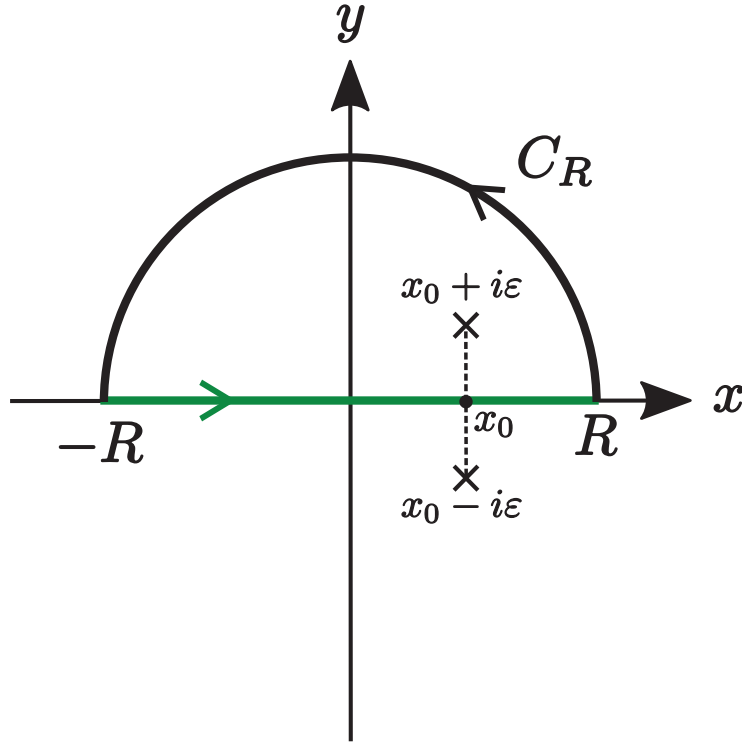


Figure 4.2: The singular point x_0 is shifted by $\pm\varepsilon$ in the imaginary axis.

According to the Hilbert formula, the action is described as

$$\begin{aligned} S &\simeq \int_{x_{in}}^{x_{out}} \int_0^H \frac{dH'}{-\frac{\partial v}{\partial x} \Big|_{x=x_h} (x - x_h)} dx \\ &= -\mathcal{P} \int_{x_{in}}^{x_{out}} \frac{E(t)}{\frac{\partial v}{\partial x} \Big|_{x=x_h} (x - x_h)} dx - i\pi \left(-\frac{E(t)}{\frac{\partial v}{\partial x} \Big|_{x=x_h}} \right). \end{aligned} \quad (4.29)$$

Since the principal value is real, the imaginary part of the action is given as

$$\Im S = \frac{\pi E(t)}{\frac{\partial v}{\partial x} \Big|_{x=x_h}}. \quad (4.30)$$

The tunneling rate is then expressed as

$$\Gamma \simeq \exp\left(-\frac{2\Im S}{\hbar}\right) = \exp\left(-\frac{2\pi E(t)}{\hbar \left.\frac{\partial v}{\partial x}\right|_{x=x_h}}\right). \quad (4.31)$$

The Hawking temperature T_H is defined by assuming that the tunneling rate is related to the Boltzmann factor $\exp(-E(t)/k_B T_H)$ with k_B being the Boltzmann constant. That reads

$$T_H = \frac{\hbar}{2\pi k_B} \left.\frac{\partial v}{\partial x}\right|_{x=x_h}. \quad (4.32)$$

This is exactly identical with Unruh's expression [45] despite being derived in a different way. Higher-order quantum corrections will appear in the theory beyond the semiclassical approximation. This will be discussed elsewhere.

We also estimate the radiation power of Hawking radiation. The radiation power for black holes in 1 + 1 dimensional asymptotically flat spacetime [48, 49] is given by

$$\frac{dE}{dt} = \frac{k_B T}{2\pi} \int_0^\infty d\omega \frac{\frac{\hbar\omega}{k_B T}}{e^{\frac{\hbar\omega}{k_B T}} - 1} = \frac{\pi}{12\hbar} (k_B T_H)^2. \quad (4.33)$$

It is interesting to note that the radiation power depends only on the Hawking temperature.

4.2 Hawking temperature in Josephson transmission lines

The Hawking temperature in our Josephson transmission lines is derived as

$$\begin{aligned} T_H &= \frac{\hbar}{2\pi k_0} \left(v_0 \frac{d\bar{x}}{dx}\right) \left.\frac{\partial \bar{v}}{\partial \bar{x}}\right|_{\bar{x}=\bar{x}_h} \\ &= T_H^0 f(\bar{v}_s), \end{aligned} \quad (4.34)$$

where the *bare* Hawking temperature T_H^0 is the dominant term of Hawking temperature expression and determines the order of the temperatures, while $f(\bar{v}_s)$ represents the dynamical contribution to the Hawking temperature of solitons as defined below,

$$T_H^0 = \frac{\hbar}{2\pi k_B} \left(\frac{1}{\sqrt{L_J C}}\right), \quad (4.35)$$

$$f(\bar{v}_s) = \left.\frac{\partial \bar{v}}{\partial \bar{x}}\right|_{\bar{x}=\bar{x}_h} = \left|\frac{\sqrt{1-\bar{v}_s^4}(12\bar{v}_s - \bar{v}_s^4 - 11)}{2\bar{v}_s^3}\right|. \quad (4.36)$$

Here we use the position of the event horizon arising under the condition of $\bar{v}_s^2(\bar{x}) = \bar{v}^2(\bar{x})$ as follows

$$\bar{x}_h^\pm = \pm \frac{1}{2\sqrt{3(1-\bar{v}_s)}} \tanh^{-1}\left(\sqrt{\frac{(1+\bar{v}_s)(1+\bar{v}_s^2)}{12}}\right). \quad (4.37)$$

The Hawking temperature is essentially determined by the characteristic time scale $(1/\sqrt{L_J C})$ as shown in Eq. (4.35). This implies that the Hawking temperature can be controlled by designing

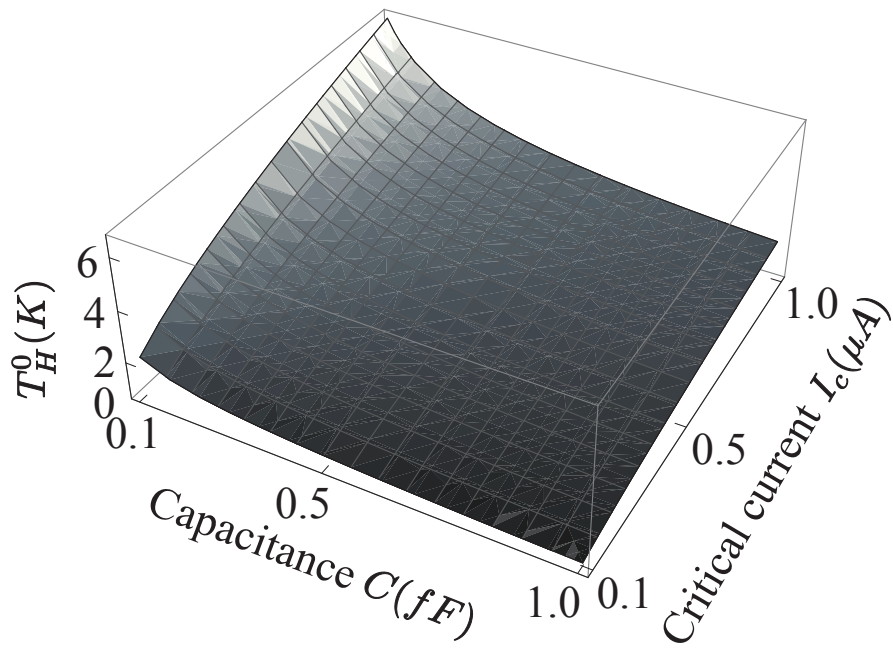


Figure 4.3: Diagram of junction parameter (the capacitance C and critical current I_c) dependence on the bare Hawking temperature T_H^0 defined in Eq. (4.35).

the circuit. In fact, the bare Hawking temperature T_H^0 changes with the junction parameters C and I_c as shown in Fig. 4.3. Note that the bare Hawking temperature is in the order of the Kelvin temperature range that is accessible experimentally in existing technologies. This result shows that analogue Hawking radiation is observable in our Josephson transmission lines.

In addition, there is a completely new contribution to the Hawking temperature in our expression that has not been found in the previous theories. That is the dynamical contribution of the soliton represented by $f(\bar{v}_s)$ as depicted in Fig. 4.4. This stems from the change in the shape of the soliton depending on the soliton velocity as shown in Fig. 4.5. This contribution indicates that the Hawking temperature can be controlled simply by changing the soliton velocity without changing the circuit at all. Therefore, it can be confirmed that the experimentally detected radiation is indeed due to Hawking radiation through this change. This is an advantageous feature that has never existed before. Considering this effect, the Hawking temperature eventually reaches tens milli-Kelvin order for $v_s = 0.98v_0$ and is sufficiently observable.

Using the results obtained above, the radiation power can be estimated to be in the region of 10^{-17}W to 10^{-15}W for $v_s = 0.98v_0$. Therefore, Hawking radiation can be detected experimentally enough from the viewpoint of the radiation power.

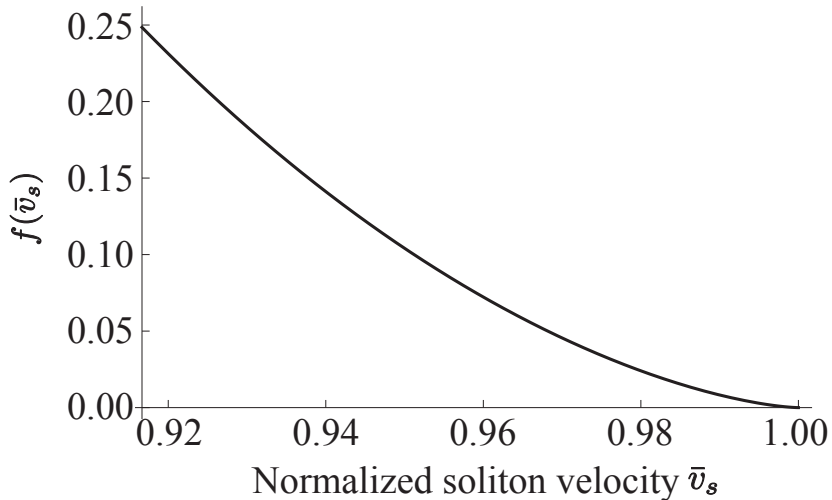


Figure 4.4: Diagram of soliton velocity \bar{v}_s dependence on Hawking temperature $f(\bar{v}_s)$ given in Eq. (4.36).

4.3 The Hawking temperature in nonlinear LC transmission lines

Now let us evaluate the Hawking temperature in nonlinear LC transmission lines. The Hawking temperature is described by [50]

$$T_H = \frac{\hbar}{2\pi k_B} \left| \frac{\partial v_g}{\partial \eta} \right|_{\eta=\eta_h}. \quad (4.38)$$

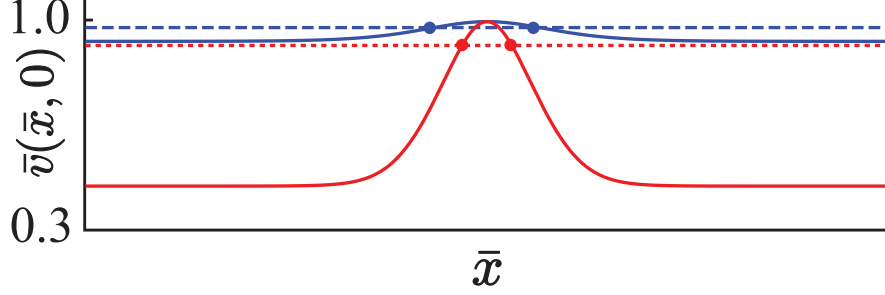


Figure 4.5: The shape of the solitons depends on the soliton velocity. The red (blue) solid line represents the normalized velocity of the electromagnetic waves at $\bar{v}_s = 0.92$ (0.98). The horizontal dotted lines and circles represent the normalized soliton velocity \bar{v}_s and the position of the event horizons.

The gradient of the electromagnetic-wave velocity is given as

$$\frac{\partial v_g}{\partial \eta} = \frac{v_0}{a} \frac{\sqrt{6}}{2} \frac{V_A^2}{V_0^2} \left\{ 1 + \frac{V_A}{V_0} \tanh \left(\frac{\sqrt{6}}{a} \frac{V_A}{V_0} \eta \right) \right\}^{-\frac{1}{2}} \operatorname{sech}^2 \left(\frac{\sqrt{6}}{a} \frac{V_A}{V_0} \eta \right) \cos \frac{ka}{2}. \quad (4.39)$$

Together with Eq. (3.38) and (4.39), the Hawking temperature is given as

$$T_H = \frac{\hbar}{2\pi k_B} \frac{v_0}{a} \frac{\sqrt{6}}{2} \frac{V_A^2}{V_0^2} \frac{v_0}{v_s} \left\{ 1 - \frac{V_0^2}{V_A^2} \left(\frac{v_s^2}{v_0^2 \cos^2 \frac{ka}{2}} - 1 \right)^2 \right\} \cos^2 \frac{ka}{2}. \quad (4.40)$$

The Hawking temperature depends on the soliton velocity as shown in Fig. 4.6. The Hawking temperature reaches the maximum \tilde{T}_H where the gradient of the electromagnetic-wave velocity at the horizon η_h is the largest. The soliton velocity \tilde{v}_s , which gives the maximum Hawking temperature, is derived by

$$\frac{dT_H}{dv_s} = 0. \quad (4.41)$$

Solving this equation, we obtain

$$\tilde{v}_s = v_0 \sqrt{\frac{1}{3} \left(1 + \sqrt{4 - 3 \frac{V_A^2}{V_0^2}} \right) \cos \frac{ka}{2}}, \quad (4.42)$$

and

$$\tilde{T}_H = \frac{\hbar}{2\pi k_B} \frac{v_0}{a} \left\{ \frac{2\sqrt{2}}{3} \cos \frac{ka}{2} \left(3 \frac{V_A^2}{V_0^2} - 2 + \sqrt{4 - 3 \frac{V_A^2}{V_0^2}} \right) \left(1 + \sqrt{4 - 3 \frac{V_A^2}{V_0^2}} \right)^{-\frac{1}{2}} \right\}, \quad (4.43)$$

which means that the order of magnitude of the Hawking temperature is dominated by $v_0/a = 1/\sqrt{LC_0}$. The Hawking temperature reaches the milli-Kelvin order with experimentally feasible circuit parameters as shown in Fig. 4.6. This shows that Hawking radiation is observable in nonlinear LC transmission lines.

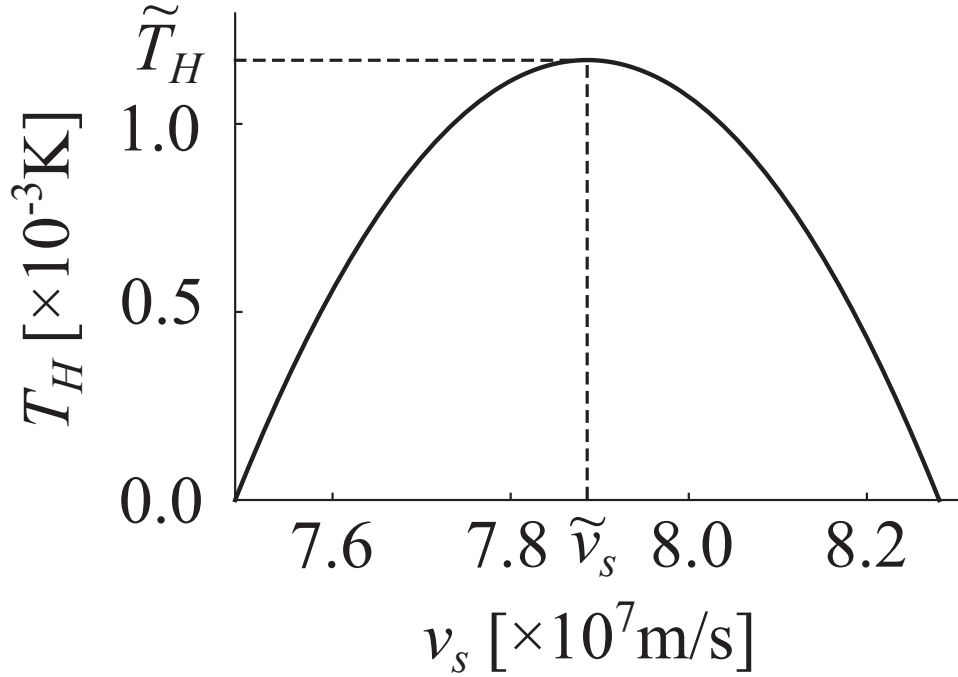


Figure 4.6: The dependence of the Hawking temperature on the soliton velocity in the nonlinear LC transmission lines. The Hawking temperature reaches the maximum \tilde{T}_H at the soliton velocity \tilde{v}_s . The circuit parameters are the same as in Fig. 3.4.

4.4 Summary

In this chapter, we have derived the Hawking temperature using a tunneling mechanism and evaluated it on our systems. The Hawking temperature was found to be experimentally accessible. The resulting formula also showed that the experimentally observed temperature was indeed due to Hawking radiation by confirming the dependence of soliton velocity on the temperature without changing circuit parameters.

Chapter 5

Quantum-circuit black hole lasers

So far, we have discussed analogue black holes in order to propose a system in which Hawking radiation can be observed. Along with the analogue black hole idea, an extremely unique proposal called a black hole laser has been made by Corley and Jacobson [51–53] to further enhance the Hawking radiation. This amplifies Hawking radiation by the stimulated emissions within an analogue cavity composed of both a black hole and a white hole for reliable observations. The dispersion relation of the system is not involved in analogue black holes but plays an important role in establishing the black hole laser, which will be discussed later. Corley and Jacobson showed that for the bosonic field, the negative energy partner goes back and forth between two horizons if the dispersion is superluminal. Some of the particles with negative energy are transformed into particles with positive energy by the mode conversion caused on the event horizons during repeating these processes. It leads to an amplification of the Hawking process.

In fact, experimental studies on black hole lasers have progressed in BECs with *anomalous* dispersion by Steinhauer et al. [54]. They reported the standing waves that formed between two horizons. This means that a partner Hawking particle with negative energy bounces at horizons. They also observed self-amplifying Hawking radiation. On the other hand, Faccio et al. proposed black hole lasers in optical fibers with *normal* dispersion [55]. In their system, the probe pulse is confined in a cavity consisting of two pulses. This is because the probe light slows down near the two pulses due to the optical Kerr effect, resulting in the formation of the event horizons. Stimulated emission in the cavity amplifies Hawking radiation.

In contrast, despite significant advances in detection techniques on extremely weak electromagnetic fields in the study of the dynamical Casimir effect [20], there have been no reports on black hole lasers in electric circuits. This is due to the absence of the anomalous dispersion required for black hole lasers in the previous electric circuits. However, there is a possibility of establishing the black hole lasers by engineering the desired dispersion relation as proposed in optical fibers, even though the system has a normal dispersion. Here, we propose the analogue black hole lasers in electric circuits.

This chapter is organized as follows. Firstly, we clarify the requirements for black hole lasers reviewing the proposals by Corley et al. [51–53] and point out the problems for proposing the black hole lasers in electric circuits. Then, we propose the black hole lasers in Josephson transmission lines with the metamaterial elements. In addition, we evaluate the entanglement entropy, which measures the degree of entanglement of particles and antiparticles created in pair production near the event horizons, in order to confirm that the emitted light is surely Hawking radiation. It is

revealed that entanglement entropy is characterized by squeezing parameters related to the Hawking temperatures, which depend on the velocity of the soliton.

5.1 Requirements for constructing black hole lasers

Here, let us briefly review the seminal works of Corley et al. [51–53] on black hole lasers and consider the conditions necessary for these. In general, the main requirements for a laser are to have a cavity and to amplify the light. The cavity is composed of two mirrors facing each other, and the light travels back and forth between them as represented in Fig. 5.1 (a). Standing waves are formed in the cavity when the spacing between the mirrors is an integer multiple of the half-wavelength of the light. This causes the light to be in phase. The optical amplification is based on the stimulated emission in the medium inside the cavity as follows. Stimulated emission requires a population inversion, in which the probability is distributed higher in the excited state than in the ground state. This population inversion is formed by pumping ground-state atoms that absorb pump light in a laser medium and are excited to an excited state. In population inversion, stimulated emission predominates over absorption. When light injects a medium with a population inversion, the excited atoms are stimulated to undergo quantum transitions with the emission of light equal to its energy difference to the ground state and in phase as the incident light. This light serves as a seed to stimulate other atoms in the excited level, resulting in a quantum transition to the ground level. This chain process, called stimulated emission, amplifies the light (Fig. 5.1 (b)). The light is further amplified since it travels back and forth through the medium between the mirrors. Finally, a part of the amplified light can be taken out as laser light if the mirror on one side is semitransparent.

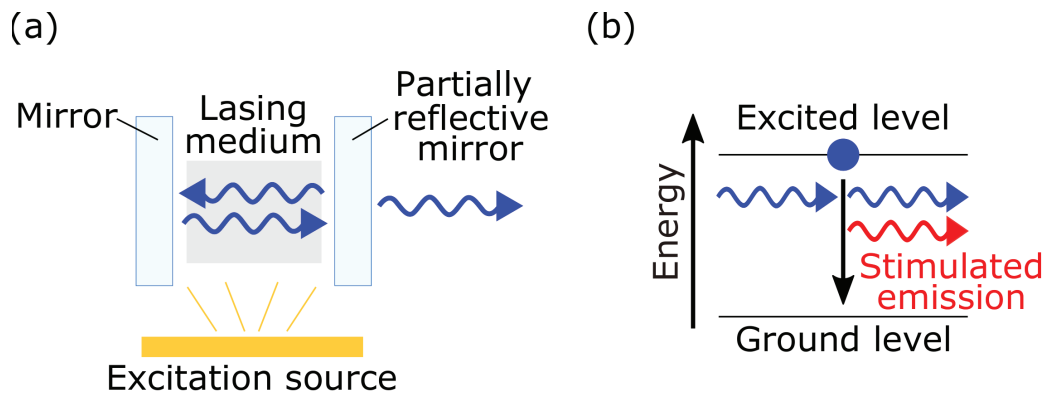


Figure 5.1: (a) A laser device consists of two mirrors and a lasing medium. The light bounces off the mirrors. The atoms in the lasing medium are excited by the external pumping, resulting in forming the population inversion in the probability distribution. The amplified light is emitted through the partially reflective mirror. (b) The stimulated emission occurs in the lasing medium. When the light of a specific frequency is incident on the population inversion, the excited atom undergoes a quantum transition to the ground state, and light with the same phase and direction as the incident light is emitted. This emitted light induces quantum transitions in the same way for other atoms, producing new in-phase light. The light in the resonator is amplified in this chained process.

Now let us review the black hole laser proposed by Corley et al. [53]. In their proposal, two

horizons play the role of a cavity. They assume the Reissner-Nordström black hole spacetime in Painlevé Gullstrand coordinates as

$$ds^2 = (c^2 - v^2(x)) dt^2 + 2v(x) dt dx + dx^2, \quad (5.1)$$

where the free-fall velocity is given as $v(x) = -\sqrt{2GM/x - Q^2/x^2}$ with the gravitational constant G , the mass M and the charge Q of the black hole, and the speed of light in the vacuum c . The event horizon is formed under the condition $c^2 = v^2(x)$. When applied to the model of carp climbing a waterfall, the free-fall speed corresponds to the space-dependent water flow speed, while the speed of light is the speed of the carp swimming in still water, which is a constant. Since two horizons are required to construct the resonator, let us consider the downstream of the waterfall in addition to the model considered for a single black hole as shown in Fig. 5.2. In this case, the carp can swim freely upstream (Region I) and downstream (Region III) of the waterfall, because the water flow is gentle. On the other hand, carp in the waterfall (Region II) cannot climb up and is washed away due to the fast flow. As a result, the boundary of Region I and II becomes a black hole horizon because the carp in Region II cannot escape to Region I, and another boundary (Region II and III) becomes a white hole horizon since the carp in Region III cannot enter to Region II. These horizons, however, do not work as mirrors of a cavity because the carp that reaches the white hole horizon do never return to the black hole. By making these horizons act as mirrors, the carp can climb up without being swept away. This requires the anomalous dispersion as described below.

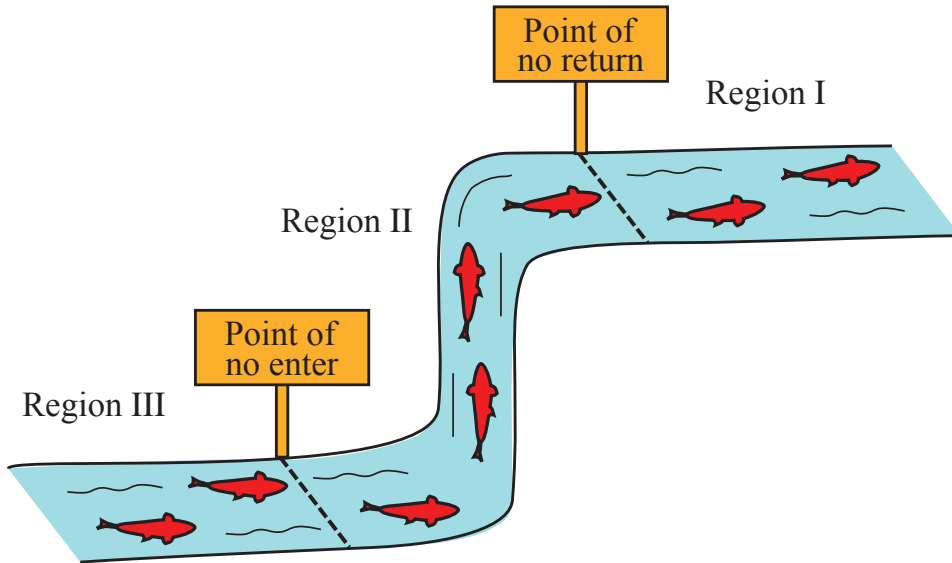


Figure 5.2: The model of carp climbing up the waterfall for a black hole and a white hole. Suppose a carp has the ability to swim at a constant velocity of c against still water. The velocity of the water flow depends on the space. The carp at both sides of the waterfall (Region I and III) can climb up because the water flow is gentle upstream and downstream where $|v(x)| < |c|$, whereas the carp inside the waterfall (Region II) cannot climb up at all where $|v(x)| > |c|$. Therefore, two event horizons are generated where $v^2(x) = c^2$. A black hole horizon is located at the boundary of Region I and II, while a white hole horizon is settled at the boundary of Region II and III.

Here we explain that the horizons behave as the mirrors if the system has anomalous dispersion. At first, we derive the equation of motion for the bosonic field ϕ according to their work. They adopted a linear field theory with higher spatial derivatives in the potential as

$$U = -\phi \hat{F}(\partial_x) \phi, \quad (5.2)$$

$$\hat{F}(\partial_x) = c^2 \left(\partial_x^2 - \frac{1}{k_0^2} \partial_x^4 \right), \quad (5.3)$$

in order to provide an anomalous dispersion relation. When there is no background flow, the kinetic energy is given as

$$K = \frac{1}{2} m \left(\frac{\partial \phi}{\partial t} \right)^2, \quad (5.4)$$

where m represents the mass of the boson. The Lagrangian density is given as

$$\mathcal{L} = \frac{1}{2} \left(\frac{\partial \phi}{\partial t} \right)^2 + \phi \hat{F}(\partial_x) \phi, \quad (5.5)$$

where we set $m = 1$ for simplicity. When the background velocity is $-v$, the Lagrangian density is modulated as

$$\mathcal{L} = \frac{1}{2} \left[\left(\frac{\partial}{\partial t'} + v \frac{\partial}{\partial x'} \right) \phi \right]^2 + \phi \hat{F}(\partial_{x'}) \phi, \quad (5.6)$$

through the coordinate transformations

$$\begin{cases} x' = x + vt \\ t' = t, \end{cases} \quad (5.7)$$

and their derivatives

$$\frac{\partial}{\partial t} = \frac{\partial x'}{\partial t} \frac{\partial}{\partial x'} + \frac{\partial t'}{\partial t} \frac{\partial}{\partial t'} = v \frac{\partial}{\partial x'} + \frac{\partial}{\partial t'}, \quad (5.8)$$

$$\frac{\partial}{\partial x} = \frac{\partial x'}{\partial x} \frac{\partial}{\partial x'} + \frac{\partial t'}{\partial x} \frac{\partial}{\partial t'} = \frac{\partial}{\partial x'}, \quad (5.9)$$

which mean the coordinate system (x', t') of an observer on a conveyor belt moving at $-v$ as shown in Fig. 5.3 (a). These transformations can also be interpreted as a stationary observer looking at the field on the conveyor belt moving at the velocity v as shown in Fig. 5.3 (b). We express the laboratory coordinate as (x, t) and the Free-fall frame as (x', t') to match the notation with their paper. The Lagrangian density is written as

$$\mathcal{L} = \frac{1}{2} \left[\left(\frac{\partial}{\partial t} + v \frac{\partial}{\partial x} \right) \phi \right]^2 + \phi \hat{F}(\partial_x) \phi, \quad (5.10)$$

and the action is given as

$$S_\phi = \iint \mathcal{L} dx dt = \frac{1}{2} \int d^2x \left\{ [(\partial_t + v \partial_x) \phi]^2 + \phi \hat{F}(\partial_x) \phi \right\}. \quad (5.11)$$

From the principle of least action $\delta S_\phi = 0$, the Euler-Lagrange equation is given as

$$\frac{\partial \mathcal{L}}{\partial \phi} - \frac{d}{dt} \frac{\partial \mathcal{L}}{\partial (\partial_t \phi)} - \frac{d}{dx} \frac{\partial \mathcal{L}}{\partial (\partial_x \phi)} = 0. \quad (5.12)$$

From the Euler-Lagrange equation, we obtain the wave equation

$$(\partial_t + \partial_x v) (\partial_t + v \partial_x) \phi = c^2 \left(\partial_x^2 \phi - \frac{1}{k_0^2} \partial_x^4 \phi \right). \quad (5.13)$$

We replace the wave solution like

$$\phi(t, x) = \exp \left(-i\omega t + i \int^x k(x') dx' \right), \quad (5.14)$$

into Eq. (5.13) and obtain the dispersion relation

$$(\omega - vk)^2 = F^2(k), \quad (5.15)$$

$$F^2(k) = c^2 \left(k^2 + \frac{k^4}{k_0^2} \right), \quad (5.16)$$

where ω and k are the frequency and the wavenumber in the laboratory system. The frequency relation between in the free-fall frame ω' and laboratory frame can be written as $\omega' = \omega - vk$ by the Doppler effect. The frequency in the free-fall frame is written by the two following equations

$$\omega' = \omega_0 - vk, \quad (5.17)$$

$$\omega' = \pm F(k), \quad (5.18)$$

where the observed frequency in the laboratory system is ω_0 and $F(k)$ is a function with a positive gradient.

For a sake of simplicity, let us first consider the dispersionless case

$$F(k) = ck. \quad (5.19)$$

In this case, the phase velocity is equal to group velocity. Figure 5.4 (A) shows the dispersion relation Eq. (5.18). The lines represent the Doppler shift ω' expressed in Eq. (5.17). In this Figure, a black solid (dotted) line represents the solution of $\omega' = F(k)$ ($\omega' = -F(k)$). The black solid and dotted lines are straight because there are no nonlinear terms in the dispersion relation of Eq. (5.19). The gradient of these black lines represents the group velocity in the free-fall frame $v'_g = d\omega'/dk = \pm dF(k)/dk$. Therefore, the black solid (dotted) line represents a wave going to the right (left) side with a positive (negative) velocity in the free-fall frame because it has a positive (negative) gradient. The green, red, and blue lines shows the Doppler shifts expressed in Eq. (5.17) when $v = 0$, $0 < |v| < |c|$, and $|v| > |c|$, respectively. The intersections of the black lines and the colored lines represent the modes of the background flow that satisfy the dispersion relation. When there is no background flow, the intersections of the green line and the black lines correspond to the modes propagating in the system. The green-filled circle is the mode propagating to the right with the velocity c and the green open circle represents the mode propagating to the left with the velocity $-c$. In short, light can propagate at the speed c , when the background velocity is zero. The background flow $v(x)$ causes the Doppler shift. When the speed of background flow is slower than

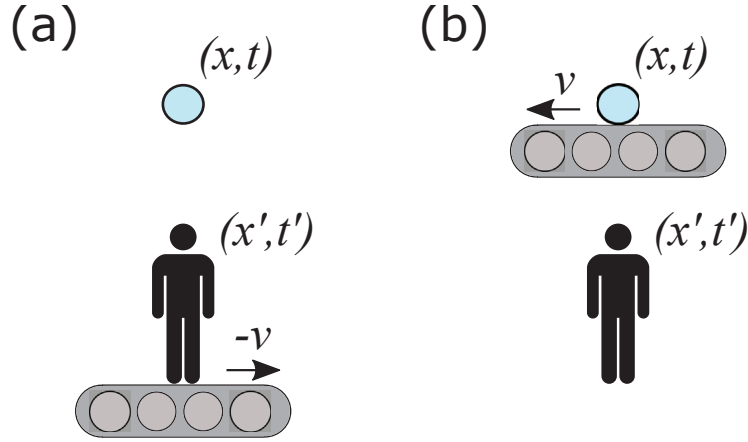


Figure 5.3: Two interpretations of the Galilei transformation (5.7). (a) The coordinate system (x, t) is seen from an observer (x', t') on a conveyor belt that moves with $-v$. (b) The coordinate system (x, t) on the conveyor moving with v is seen from a fixed observer (x', t') .

that of the light, i.e., $|v| < |c|$, the gradient of the red line is smaller than that of the black line. In that case, a red-filled circle is a mode propagating to the right with the velocity c and a red open circle is a mode propagating to the left with the velocity $-c$ in the free-fall frame. The Doppler shift causes an increase (decrease) in the frequency of the right (left) traveling mode compared to the case without background flow. When the background flow speed is faster than the light speed $|v| > |c|$, the blue line is inclined more than the blue line. There are two modes represented by a blue-filled circle and a blue open circle. The blue-filled one is the mode propagating to the right with the velocity c in the free-fall frame and can be regarded as an antiparticle with negative energy. The other mode represented by a blue open circle is a mode traveling to the left with the velocity $-c$ in the free-fall frame. We focus on the modes traveling in the opposite direction of the background flow. In other words, we handle carp against the flow of the river. Hereafter, we ignore the left traveling modes represented by the open circles.

We have discussed modes in the free-fall frame in Fig. 5.4 (A) above. Now, let us reconsider how those modes travel for the observer in the laboratory system. The group velocity in the laboratory system is given by

$$v_g = \pm \frac{dF(k)}{dk} + v = v'_g + v, \quad (5.20)$$

which is the inclination of a black line subtracted by that of a colored line in Fig. 5.4 (A). To put it another way, the dispersion relation in the laboratory system can be reworked as follows,

$$\omega = \omega_0, \quad (5.21)$$

$$\omega = vk \pm F(k). \quad (5.22)$$

In Fig. 5.4 (a), the black line parallel to the k -axis represents the observed frequency ω_0 given by Eq. (5.21) and the colored lines are the dispersion relation in the laboratory system at several velocities by Eq. (5.22). The intersections of the black line and the colored lines represent the modes realized in the system. The group velocity in the laboratory system is given by the gradient

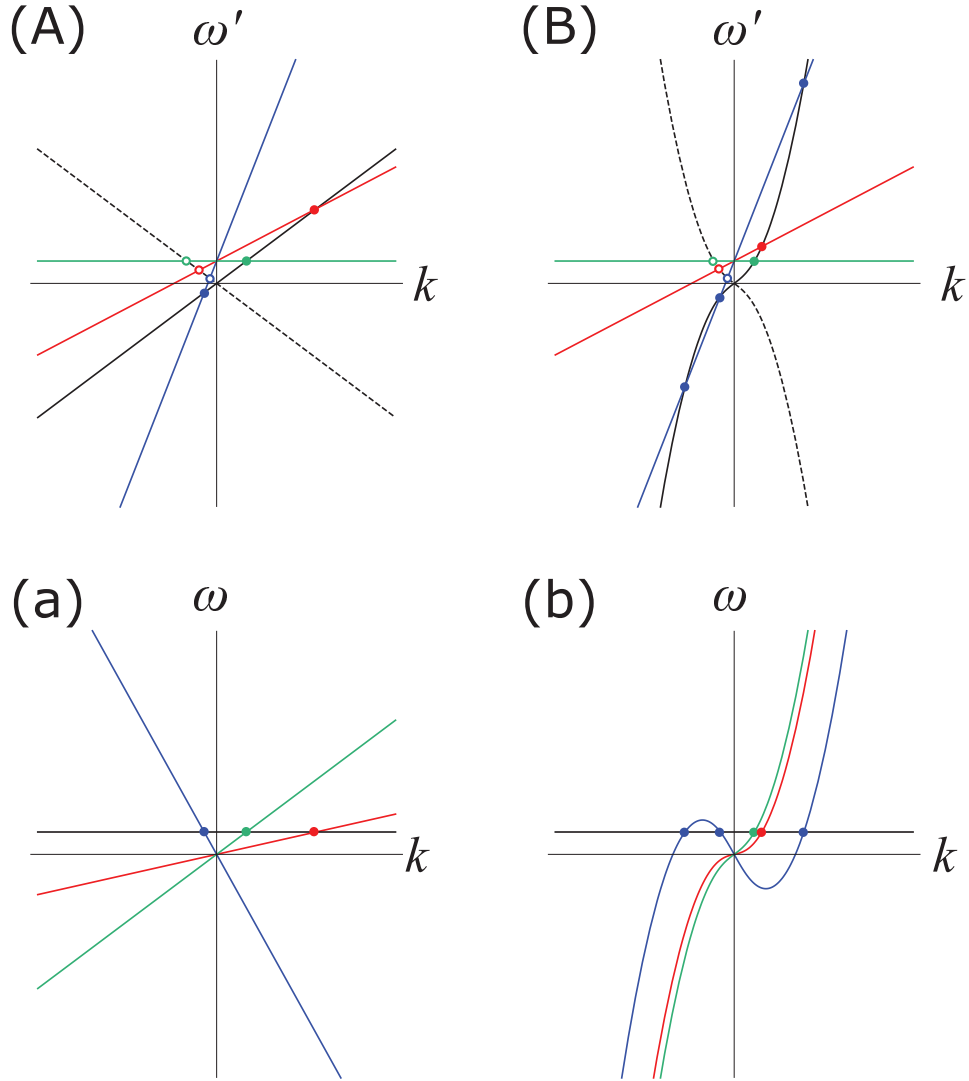


Figure 5.4: (A)(B) The graph of the dispersion relation in the free-fall frame (black lines) given by Eq. (5.18) and the Doppler shift (colored lines) given by Eq. (5.17). The horizontal axis represents the wavenumber k and the vertical axis with the frequency ω' in the free-fall frame. The solid black line plot the solution with the positive group velocity ($\omega' = F(k)$) and the black dotted line represents the solution with the negative group velocity ($\omega' = -F(k)$) in Eq. (5.18). The green, red and blue lines represent the Doppler shift given by Eq. (5.17) when the background flow is 0, $0 < |v| < |c|$, and $|v| > |c|$, respectively. The modes that are the solutions of Eq. (5.18) and Eq. (5.17) are given by the intersections of the black lines and the colored lines. The right-moving modes in the free-fall frame are marked by the open circles and the left traveling modes are depicted by the filled circles. (a) (b) The Diagram of the dispersion relation in the laboratory system given by Eq. (5.22), where we focus on the solution $\omega = vk + F(k)$. The horizontal axis and the vertical axis indicate the wavenumber k and the frequency ω in the laboratory frame. The green, red and blue lines represent the dispersion relation given by Eq. (5.22) when the background flow is 0, $0 < |v| < |c|$, and $|v| > |c|$, respectively. The intersections of the colored curves and the parallel black line representing Eq. (5.17) are existing modes. We use Eq. (5.19) for (A) and (a), and Eq. (5.23) for (B) and (b).

of the dispersion relation. When the background speed is smaller than the light speed $0 < |v| < |c|$, there is a mode traveling to the right indicated by the red-filled circle in the laboratory system. On the other hand, there exists a left traveling mode for $|v| > |c|$.

Now, let us return to the dispersion relation with a nonlinear term given by Eq. (5.16) where $F(k)$ is defined as

$$F(k) = \begin{cases} c\sqrt{k^2 + \frac{k^4}{k_0^2}} & k \geq 0 \\ -c\sqrt{k^2 + \frac{k^4}{k_0^2}} & k < 0. \end{cases} \quad (5.23)$$

Figures 5.4 (B) and (b) show the dispersion relation in the free-fall frame and the laboratory frame as in Figures 5.4 (A) and (a), respectively. The nonlinearity distorts the dispersion relation as shown in Fig. 5.4 (B). The dispersion is called anomalous dispersion, where the larger the wavenumber, the faster the phase velocity and the smaller the refractive index. In the long-wavelength limit, the dispersion relation approaches a dispersion-less one. Therefore, for $0 \leq |v| < |c|$, there is the same number of modes as when the dispersion relation is linear. On the other hand, there are three right-moving modes in the free-fall frame indicated by blue-filled circles and a left traveling mode in the free-fall frame depicted by a blue open circle. The two modes are added at the region with the large wavenumber due to the anomalous dispersion. Figure 1.4 (b) shows the dispersion relation in the laboratory frame. In this figure, we consider only the modes that travel to the right in the free-fall frame. The two modes added to Fig. 5.4 (a) are depicted by blue circles on both sides and have positive group velocity due to their positive gradient. These modes correspond to carp overcoming the flow of the waterfall as shown in Fig. 5.5 (a). This causes the two horizons to play the role of mirrors as described later.

Here, let us show how these modes propagate. There is one right-traveling mode as particles outside horizons for $0 < |v| < |c|$, which we call the T mode. On the other hand, there exist three modes between horizons for $|v| > |c|$. One is the N mode which propagates to the right as an antiparticle, another is the P mode which travels to the right as a particle, and the other is the IN mode traveling to the left as an antiparticle. In Fig. 5.5, the solid and the dotted arrows represent a particle with positive energy ($\omega' > 0$) and an antiparticle with negative energy ($\omega' < 0$) in the free-fall frame, respectively. Figure 5.5 (b) shows the trajectories of propagating modes. At first, a particle (T mode) and an antiparticle (IN mode) are pair-created by the quantum fluctuations in the vacuum at the black hole horizon. The T mode is emitted as Hawking radiation, while the IN mode falls to the white hole horizon. The IN mode transfers to the P mode and N mode with higher group velocity and then can turn back to the black hole horizon by the mode conversion at the white hole horizon. Then the P mode crosses the black hole horizon, while the N mode bounces back at the black hole horizon. In other words, the antiparticle modes bounce at horizons while the particle modes are emitted as Hawking radiation. As a result, the anomalous dispersion realizes a carp that overcomes the background flow, making the horizons behave like mirrors.

Next, we briefly review the essence of the amplification mechanism by Corley et al. From the conservation of the Noether current for the time

$$\frac{\partial}{\partial t} \int d^3x J^0 = 0, \quad (5.24)$$

we can define a conserved value as

$$(f, g) = i \int dx [f^* (\partial_t + v\partial_x) g - g (\partial_t + v\partial_x) f^*], \quad (5.25)$$

which is called Klein Gordon inner product, where f and g are the solutions of the Eq. (5.13). The norm of the modes is conserved through the process as follows,

$$\|IN_m\| = \|IN_{m+1}\| + \|T_{m+1}\|, \quad m \geq 0, \quad (5.26)$$

where $\|X_m\|$ denotes the norm defined by the Klein Gordon inner product of the m th X mode. Since $\|IN_m\| > 0$ and $\|T_{m+1}\| < 0$, this results in $\|IN_{m+1}\| > \|IN_m\|$. Therefore, the Hawking radiation is amplified by the mode transformations based on the norm conservation at the event horizon. This is the essential concept of the black hole laser [51–53]. The detailed derivation of the amplification is described in [51–53].

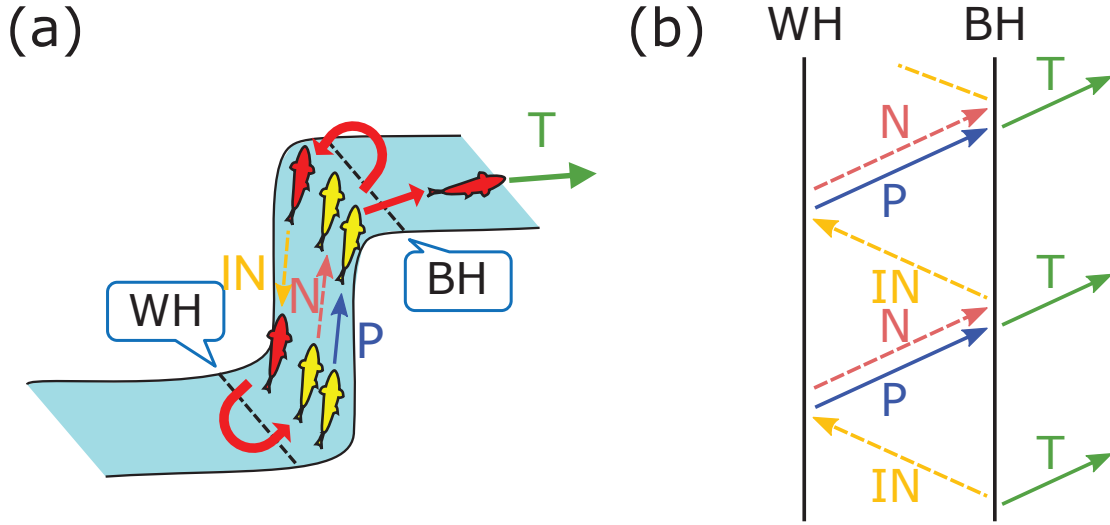


Figure 5.5: (a) Image of the mode propagation. The anomalous dispersion creates a yellow carp that can climb the waterfall against strong currents, resulting in a horizon acting as a mirror. (b) Schematic diagram of the trajectories of modes. The solid (dashed) lines represent modes with positive (negative) frequencies for antiparticles (particles).

5.2 Identifying issues and their approaches

The black hole laser originally requires the anomalous (superluminal) dispersion with a positive curvature in the dispersion curve of the system [51–53]. However, the anomalous dispersion required for black hole lasers has not been reported in the electric circuits so far. In addition, nonlinear effects have not been actively considered because they are not a necessary condition for analogue gravity effects. These are ones of the reasons why no black hole laser has been proposed so far.

To overcome the first issue, we use the model that a black hole laser is feasible even in subluminal dispersion where the dispersion curve is well designed as in optical fibers [56]. A carp that can climb up the waterfall without flowing (hereinafter referred to as “super carp”) is required to obtain two horizons that behave like mirrors as described above. In order to produce super carp in normal dispersion, the dispersion curve needs to form a mode in which it has a large curvature at low frequencies and propagates with a group velocity faster than the reference wave. In the desired

normal dispersion relation, there is only one mode in which the super carp climbs the waterfall and reaches the black hole horizon. Then, the super carp turns into ordinary carp and drifted off to the white hole horizon. After that, some become super carp again, while others flow downstream. In that way, two horizons behave as mirrors even in the normal dispersion by creating the desired dispersion relation.

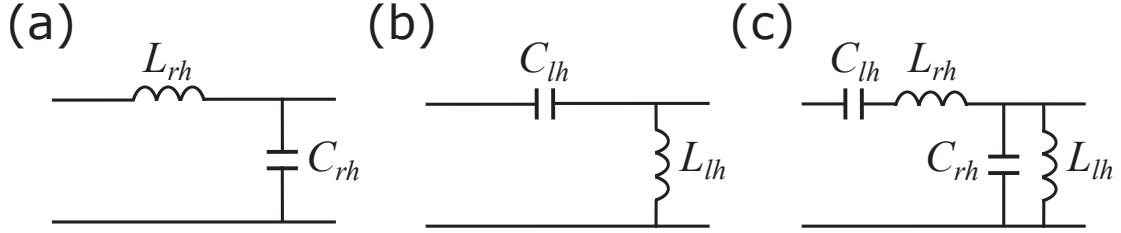


Figure 5.6: (a) A right-handed transmission line with the inductance L_{rh} and capacitance C_{rh} . (b) A left-handed transmission line with the inductance L_{lh} and capacitance C_{lh} . (c) A composite right/left-handed transmission line called CRLH.

To create the desired dispersion relation in electric circuits, we employ dispersion engineering using *metamaterials* made of sub-wavelength inclusions that provide tremendous degrees of freedom to manipulate the electromagnetic parameters of materials and modes with high precision. In fact, metamaterials create a medium in which the permittivity and permeability are simultaneously negative, which does not exist in nature, and enables the unique property that the phase velocity and group velocity of electromagnetic waves are opposite to each other. Figure 5.6 (a) and (b) represent right-handed components and left-handed components on transmission lines, respectively. The dispersion relation on the right-handed transmission lines is given by

$$\omega = \frac{2}{\sqrt{L_{rh}C_{rh}}} \sin \frac{ka}{2}, \quad (5.27)$$

where L_{rh} and C_{rh} are the inductance and the capacitance. On the other hand, the dispersion relation on the left-handed transmission lines is given by

$$\omega = -\frac{2}{\sqrt{L_{lh}C_{lh}}} \frac{1}{\sin \frac{ka}{2}}, \quad (5.28)$$

where L_{lh} and C_{lh} are the inductance and the capacitance. The left-handed transmission lines are not realized practically, because the group velocity would become infinity as the frequency increases and then faster than the light velocity c . In practice, we need to consider the composite of the right-handed and the left-handed elements which is called CRLH(Composite Right/Left-Handed) as shown in Fig. 5.6 (c). It has the dispersion relation as

$$k = \frac{1}{a} \arccos \left\{ 1 - \frac{1}{2} \left(\omega L_{rh} - \frac{1}{\omega C_{lh}} \right) \left(\omega C_{rh} - \frac{1}{\omega L_{lh}} \right) \right\}. \quad (5.29)$$

The left-handed elements are dominant in low frequencies and the right-handed elements are dominant in high frequencies. In this way, we can engineer the dispersion relation by adding the metamaterial elements into transmission lines.

We also introduce the Josephson effect in the transmission line for addressing the second issue. It provides the Kerr nonlinearity [57, 58] essential for black hole laser, which determines the group velocity, required to select the propagation modes in the system.

5.3 Model

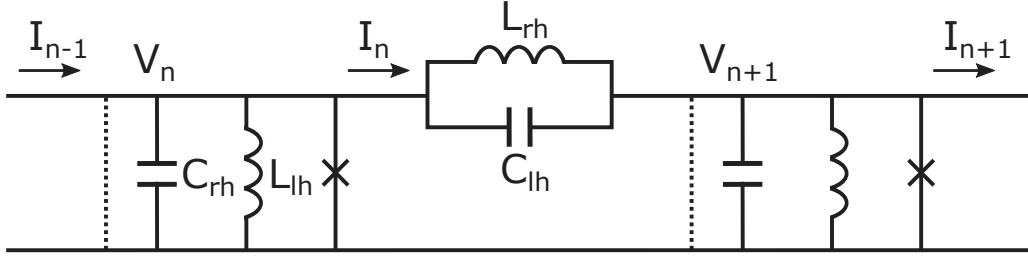


Figure 5.7: Schematic representation of the composite right/left-handed nonlinear transmission line. Each unit cell consists of a linear inductive element of inductance L_{rh} in parallel with a linear capacitance C_{lh} in the series branch, which constitute the linear dispersive element of the line, and a linear inductive element of inductance L_{lh} in parallel with a linear capacitor of capacitance C_{rh} as well as the Josephson element responsible for the nonlinearity of the system in the shunt branch. The dotted vertical lines mark the unit cell of the lattice.

Here, we propose black hole lasers in transmission lines by introducing *metamaterial* elements into the circuit that realize particle-antiparticle pair propagation modes possible with anomalous dispersion into a normal one, as well as the Kerr nonlinearity for controlling propagating mode selection in the cavity and amplifying the Hawking process. Suppose a Josephson *metamaterial* transmission line which consists of a number of LC blocks each comprised of composite right/left-handed components together with a Josephson element in the shunt branch as illustrated in Fig. 5.7. Starting from the application of Kirchoff's law to this system together with the Josephson relation, the current conservation at the n th node is expressed as

$$I_n - I_{n-1} = -I_{J,n} - I_{C_{rh},n} - I_{L_{lh},n}, \quad (5.30)$$

where I_n is the current through the n th node comprising of the current through the right-handed (rh) inductor with inductance L_{rh} and the left-handed (lh) capacitor with capacitance C_{lh} at the n th cell, i.e., $I_n = I_{L_{rh},n} + I_{C_{lh},n}$,

$$I_{L_{rh},n} = -\frac{\hbar}{2e} \frac{1}{L_{rh}} (\theta_{n+1} - \theta_n), \quad (5.31)$$

$$I_{C_{lh},n} = -\frac{\hbar}{2e} C_{lh} \frac{d^2}{dt^2} (\theta_{n+1} - \theta_n), \quad (5.32)$$

where I_c , \hbar , e , and θ_n are the Josephson critical current, Dirac's constant, an elementary charge, and the phase difference in the n th junction, respectively. The currents on the right-hand side of Eq. (5.30) are the Josephson current $I_{J,n}$, the displacement current $I_{C_{rh},n}$ flowing through the n th

Josephson junction with capacitance C_{rh} , and the current $I_{L_{lh}}$ through the left-handed inductor with inductance L_{lh} . Combining these relations, we obtain the following circuit equation,

$$C_{rh} \frac{d^2 \theta_n}{dt^2} + \frac{1}{L_{lh}} \theta_n + \frac{1}{L_J} \left(\theta_n - \frac{\theta_n^3}{3!} \right) - \left(\frac{1}{L_{rh}} + C_{lh} \frac{d^2}{dt^2} \right) (\theta_{n+1} + \theta_{n-1} - 2\theta_n) = 0, \quad (5.33)$$

where we use $\sin \theta_n \simeq \theta_n - \theta_n^3/6$ and $L_J = \hbar/(2eI_c)$.

Now let us derive the dispersion relation of this transmission line by ignoring the nonlinear terms of the Josephson effect. We substitute a plane-wave solution $\theta \sim \exp[i(kna - \omega t)]$ with the wavenumber k and the frequency ω for Eq. (5.33) and obtain the dispersion relation

$$\sin^2 \frac{k}{2} = \frac{1}{4} \left\{ \frac{\omega^2}{\omega_{rh}^2} - L_{rh} \left(\frac{1}{L_{lh}} + \frac{1}{L_J} \right) \right\} \left(1 - \gamma \frac{\omega^2}{\omega_{rh}^2} \right)^{-1}, \quad (5.34)$$

where $\omega_{rh} = 1/\sqrt{C_{rh}L_{rh}}$ and $\gamma = C_{lh}/C_{rh}$. We also set $a = 1$ for simplicity. In the regime of $\gamma\omega^2 \ll \omega_{rh}^2$, this reduces to

$$k \simeq \frac{\omega}{\omega_{rh}} + \frac{\gamma}{2} \frac{\omega^3}{\omega_{rh}^3}, \quad (5.35)$$

by designing the circuit so that $L_{lh} = -L_J$ [59]. This dispersion relation is the same as that of optical fibers considering black hole lasers [56]. Thus, our proposed circuit can be regarded as a circuit version of an optical fiber [56,60] at the nanometer scale.

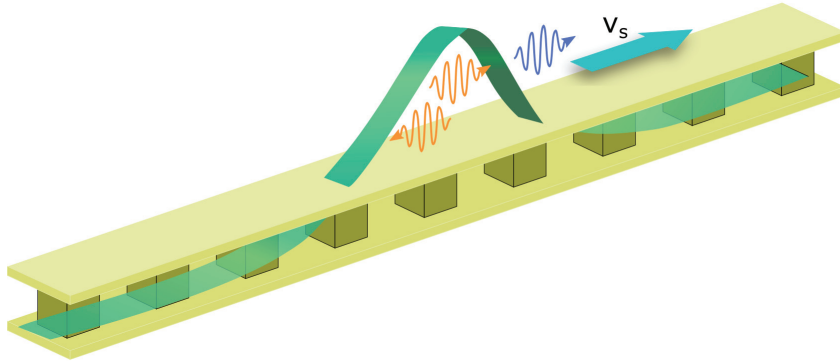


Figure 5.8: Schematic diagram of a black hole laser in an electric circuit. The refractive index perturbation $\delta n(\eta)$ (green) moving with the velocity v_s changes the velocity of the probe pulses (orange wave packets) and classically traps them inside the soliton acting as the cavity. The probe pulses can be radiated quantum-mechanically as Hawking radiation (blue) by pair productions near the horizon.

Our circuit equation contains a third-order nonlinear term just like an optical fiber, so the existence of a nonlinear wave is highly expected. Next, let us explore the waves hidden in the circuit equation (5.33) by using the discrete reductive perturbation method as follows [32,39–43]. We introduce two slow stretched space and time variables $\xi = \varepsilon(n - v_g t)$ and $\tau = \varepsilon^2 t$ with the small

dimensionless parameter ε ($0 < \varepsilon \ll 1$) and group velocity v_g to separate fast and slow variations of θ_n and expand θ_n in principle as

$$\theta_n = \theta^{(0)} + \sum_{l=-\infty}^{+\infty} \sum_{\alpha=1} \varepsilon^\alpha \theta_l^{(\alpha)}(\xi, \tau) \exp[i l(kn - \omega t)]. \quad (5.36)$$

Here, our analysis is restricted to the so-called rotating-wave approximation consisting essentially in neglecting higher harmonics,

$$\theta_n(t) \simeq \varepsilon \theta_1^{(1)}(\xi, \tau) \exp[i(kn - \omega t)] + \varepsilon \theta_1^{*(1)}(\xi, \tau) \exp[-i(kn - \omega t)]. \quad (5.37)$$

Inserting these formulas into Eq. (5.33) in order to find balanced dispersion and nonlinearity, we obtain the following equation for the ε^3 order,

$$i \frac{\partial \theta_1^{(1)}}{\partial \tau} + P \frac{\partial^2 \theta_1^{(1)}}{\partial \xi^2} + Q \left| \theta_1^{(1)} \right|^2 \theta_1^{(1)} = 0, \quad (5.38)$$

where

$$P = \frac{\omega \bar{\Omega}}{2} \left[\cos k - \omega_c^2 \left(\frac{1}{\omega^2} + \frac{3\gamma}{\omega_{rh}^2} \right) \sin^2 k \right], \quad (5.39)$$

$$Q = \frac{1}{4\omega L_J C_c}, \quad (5.40)$$

$$C_c = C_{rh} + 4C_{lh} \sin^2 \frac{k}{2}, \quad (5.41)$$

$$\bar{\Omega} = \frac{\omega_c^2}{\omega^2} \left(1 - \gamma \frac{\omega^2}{\omega_{rh}^2} \right), \quad (5.42)$$

$$\omega_c = \frac{1}{\sqrt{L_{rh} C_c}}. \quad (5.43)$$

This is a well-known nonlinear Schrödinger equation found in various systems including optical fibers [61], which contains soliton solutions. One such solution is a dark soliton expressed as,

$$\theta_1^{(1)}(\xi, \tau) = A \tanh \left(A \sqrt{\left| \frac{Q}{2P} \right|} (\xi - u\tau) \right) e^{i(k\xi - \omega t)}, \quad (5.44)$$

as shown in Fig. 5.9 (a), where A is the soliton amplitude and u is the relative soliton velocity in the $\xi - \tau$ coordinate. The solution holds under the condition $PQ < 0$, which is always satisfied in our system.

5.4 Quantum-circuit black hole lasers

Our system equipped with both the desired normal dispersion supporting pair-propagating modes and a Kerr effect is expected to be a circuit version of black hole lasers in optical fibers [56, 60]. Here we briefly review the black hole laser in an optical fiber as an example and reorganize the key parameters appropriate for our system. The fundamental idea is to amplify a probe pulse as Hawking radiation confined in the cavity formed by the two propagating solitons with the same velocity v_s acting as mirrors in a conventional laser.

5.4.1 Horizon resonators

The event horizons occur at the points where the group velocity v_g^{eff} of the probe pulse in the system cannot keep up with the soliton velocity v_s , i.e., $v_g^{\text{eff}} = v_s$. In other words, the probe pulse is trapped in the cavity and it cannot escape from the cavity, i.e., it cannot go outside the horizons classically. The effective group velocity under the Kerr modulations is given as

$$v_g^{\text{eff}} = \frac{c}{n_g + \delta n(\eta)}, \quad (5.45)$$

where n_g and $\delta n(\eta)$ represent the unperturbed group index and the refractive index perturbation modified by the Kerr effect of Josephson junctions in the comoving frame ($\eta = \xi - u\tau$), respectively.

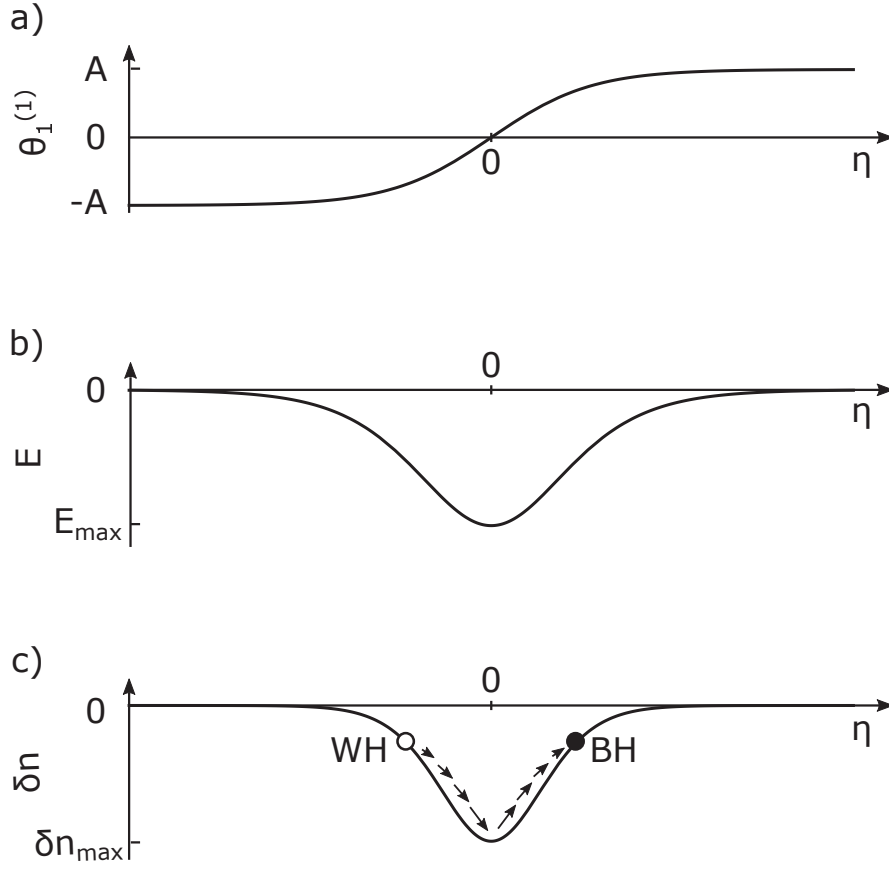


Figure 5.9: Schematic diagrams of a) the phase soliton with the amplitude A , b) the electric field with the amplitude $E_{\text{max}} = (-\hbar/2ed)A^2\sqrt{|Q/2P|}u$, and c) the cavity formed by the *single* dark soliton with the amplitude δn_{max} . The filled circle and open circle represent the horizon of the black hole and white hole, respectively. The size of arrows representing the velocity of the probe pulse varies in space.

The Kerr effect can cause a change in the refractive index depending on the strength of the electric field, equivalently the strength of the voltage in our circuit [62]. The refractive index

perturbation under the soliton propagation is expressed as

$$\delta n(\eta) = \chi E^2, \quad (5.46)$$

where χ is the third-order nonlinear susceptibility [63], which is a negative constant in the case of the circuit with Josephson junctions [57, 58] and the electric field E is given by V/d with d being the distance between plates. The voltage V across the junction is derived from the Josephson acceleration relation $V = (\hbar/2e)\partial\theta/\partial\tau$ and is expressed as

$$V = -\frac{\hbar}{2e}A^2\sqrt{\left|\frac{Q}{2P}\right|}u \operatorname{sech}^2\left(A\sqrt{\left|\frac{Q}{2P}\right|}\eta\right). \quad (5.47)$$

The soliton width w is roughly evaluated by $2\sqrt{|2P/Q|}/A$ and is about $w \simeq 150a$ for the soliton centered at the frequency $\omega_s = 4.3 \times 10^9$ Hz with $A = 0.01$, which is large enough to apply the continuum approximation. Figure 5.9 shows the electric field E (b) and the refractive index perturbation δn (c). The probe pulses are trapped in the soliton because the refractive index perturbation is negative [55]. In other words, a single soliton behaves as the cavity in our system as shown in Fig. 5.8.

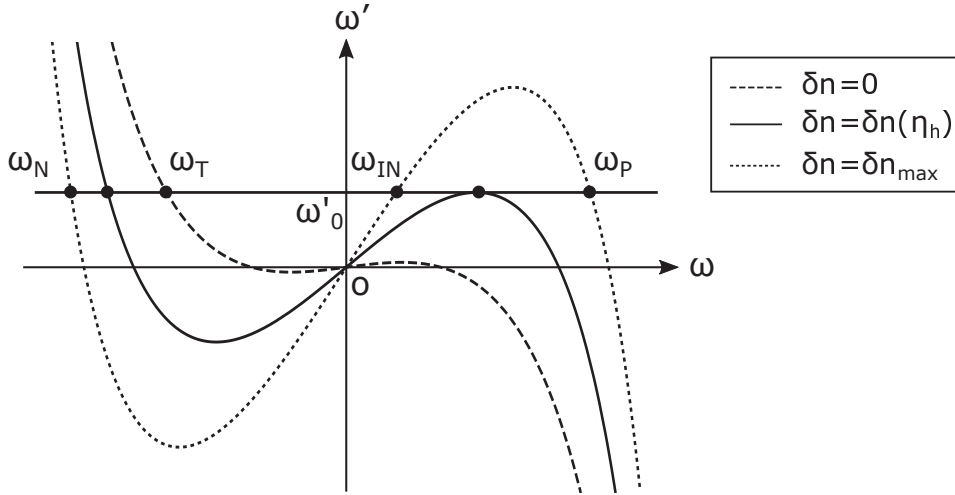


Figure 5.10: The frequencies relation between the frequency ω in the laboratory frame and the frequency ω' in the comoving frame by the Doppler shift. The dashed, solid and dotted curved lines represent the $\omega - \omega'$ relation at the perturbed index $\delta n = 0$, $\delta n = \delta n(\eta_h)$ and $\delta n = \delta n_{max}$, respectively. The horizontal line shows the invariant frequency ω'_0 in the comoving frame and the intersections with the curved lines correspond to the modes.

Now let us find the frequency modes satisfying the dispersion relation. The frequency ω' in the comoving frame is given by the Doppler relation as follows,

$$\omega'(\omega) = \omega - \omega \frac{v_s}{c} [n(\omega) + \delta n(\eta)], \quad (5.48)$$

with the soliton velocity $v_s = u + v_g(\omega_s)$ in the laboratory frame. The modes are given by the solutions of $\omega'_0 = \omega'(\omega)$, where ω'_0 is the invariant frequency in the comoving frame for the given

input frequency ω_{IN} . Figure 5.10 shows the Doppler relation in frequencies between the laboratory frame and comoving frame. The intersections of the horizontal line and the curved lines represent the modes that are realized in the system. For $\delta n = \delta n_{\text{max}}$, there are three modes ω_{IN} , ω_{P} and ω_{N} between horizons, whereas for $\delta n = 0$ there is only one mode ω_{T} outside the horizons. The frequency ω_h at the event horizon satisfies $d\omega'/d\omega|_{\omega=\omega_h} = 0$ and $\omega'(\omega_h) = \omega'_0$. We can find the position of the event horizon η_h by solving these equations.

In the laboratory frame, Eq. (5.48) is transformed as

$$k_{\text{eff}}(\omega) = \frac{\omega - \omega'_0}{v_s}, \quad (5.49)$$

where $k_{\text{eff}}(\omega)$ represents the effective dispersion relation in the laboratory system modulated by the refractive index perturbation $\delta n(\eta)$ as

$$k_{\text{eff}}(\omega) = \frac{\omega}{c}(n(\omega) + \delta n(\eta)). \quad (5.50)$$

Figure 5.11 depicts the effective dispersion relation $k_{\text{eff}}(\omega)$ as a curve and the Doppler shift as a straight line in a laboratory system, where the horizontal axis is the wavenumber k and the vertical axis is the frequency ω . The intersections of the curved lines and the straight line are the modes satisfying Eq. (5.49). The gradient of the curved line represents the group velocity v_g^{eff} in the laboratory frame, while the gradient of the straight line is the soliton velocity v_s . Contrary to Corleys' system, the soliton velocity corresponding to the waterfall flow velocity is constant, and the group velocity corresponding to the carp velocity depends on the space.

In our proposal, the cavity formed by two horizons is moving at the soliton velocity v_s . Therefore, the direction of traveling mode in the cavity is determined by the group velocity of the modes in the comoving frame. The gradient of the dispersion curve in Fig. 5.10 gives the group velocity of the mode in the comoving frame. The P, N, and IN modes travel to the left, while IN mode moves to the right. The IN mode corresponds to the yellow carp overcoming the waterfall flow as shown in Fig. 5.12 (a) and gives the function of the mirror to two horizons. This was achieved by adding the metamaterial elements into the circuit. The evolution of these modes is shown in Fig. 5.12 (b). The IN mode propagates towards the black hole horizon and turns back as the P mode to the white hole horizon together with the N mode where both modes undergo partial mode conversion. The P mode bounces at the white hole horizon and then becomes the IN mode propagating to the black hole horizon, while the N mode crosses the white hole horizon and is emitted as the T mode. Note that the antiparticles (T mode) with negative energy are emitted from the white hole horizon as partner Hawking radiation just as in the case with an optical fiber under normal dispersion. This is dual to the particle emission from the black hole horizon as Hawking radiation as shown in Fig. 5.13.

In fact, Equation (5.48) is rearranged as

$$(W - v(\eta)K)^2 = F^2(K), \quad (5.51)$$

where

$$\begin{cases} W = v_g \omega' \\ K = \omega \\ F(K) = v_s v_g k(\omega), \end{cases} \quad (5.52)$$

which is the same as the dispersion relation of the black hole lasers by Corley et al. The trajectories of the modes are represented in Fig. 5.5, where the modes corresponding to the particles and antiparticle are reversed to each other as well as reversed horizons.

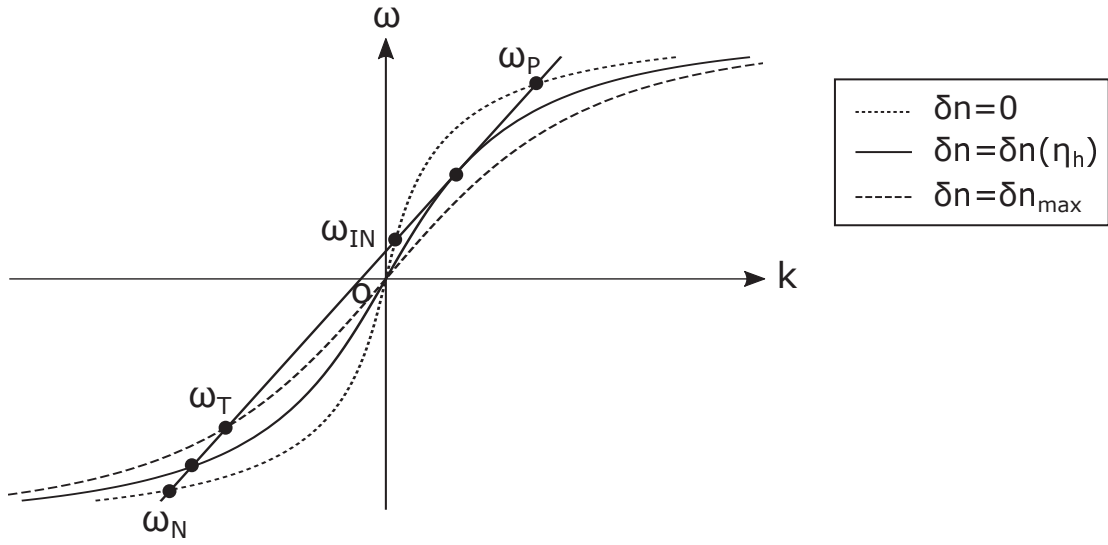


Figure 5.11: The graph of the dispersion relation (curved lines) and the Doppler shift $\omega = \omega'_0 + v_s k$ (straight line) in the laboratory frame. The horizontal axis represents the wavenumber k and the vertical axis is the frequency ω in the laboratory system. The dashed, solid and dotted curved lines represent the dispersion relation at the perturbed index $\delta n = 0$, $\delta n = \delta n(\eta_h)$ and $\delta n = \delta n_{max}$, respectively. The intersections of the straight line with the curved lines correspond to the modes realized in the system.

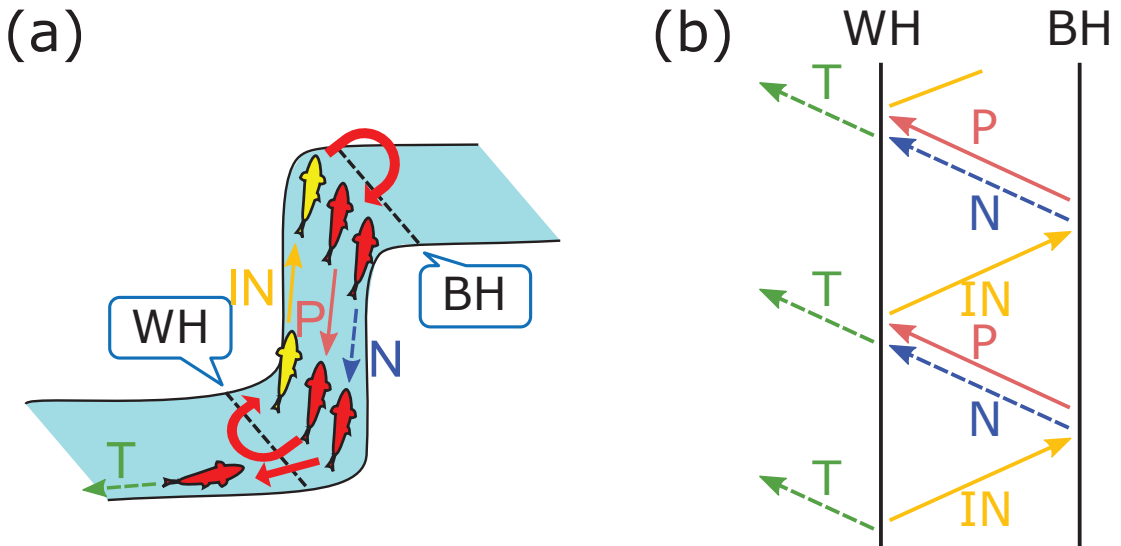


Figure 5.12: (a) Image of the mode propagation. A yellow carp is created by adding the metamaterial elements into the circuit and it can climb the waterfall against a strong current, resulting in the horizons acting like mirrors. (b) Schematic diagram of the trajectories of modes. The solid (dashed) lines represent the mode with positive (negative) frequencies for antiparticles (particles).

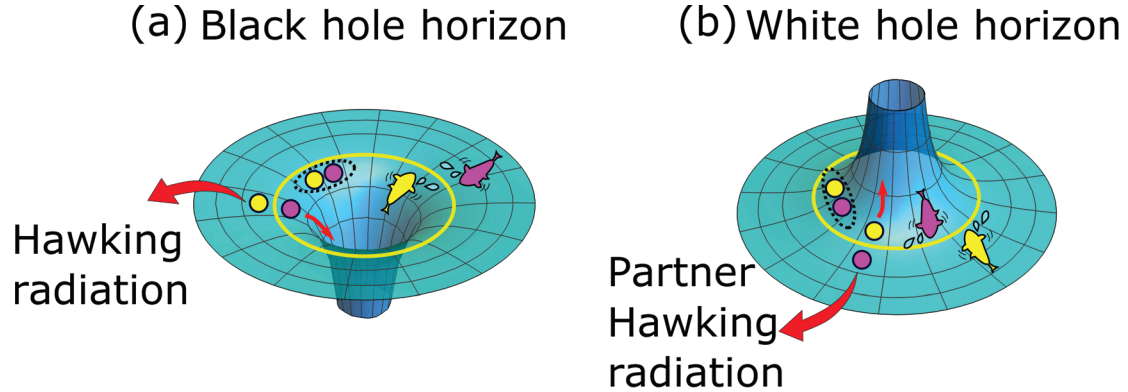


Figure 5.13: (a) Sketch of the black hole horizon. No particles cannot go out from the black hole and no antiparticles cannot enter it classically. In quantum mechanics, the particle with positive energy is released as Hawking radiation and the partner with negative energy falls into the black hole. (b) Sketch of the white hole horizon. No particles cannot enter the white hole and no antiparticles cannot escape from it classically. In quantum mechanics, the antiparticle with negative energy is radiated as partner Hawking radiation and the particle with positive energy climbs into the white hole.

5.4.2 Amplification of Hawking radiation

In our study, we consider the Josephson parametric amplification as well as the original amplification mechanism by Corley et al. In this section, we describe the amplification processes of Hawking radiation in the horizon resonator by the Josephson parametric amplification newly used in this thesis.

Here, we describe the Josephson parametric amplification in our system based on the theory of Fasolo et al. [64]. A Josephson junction has a nonlinear element that induces a four-wave mixing process. The process occurs when lights with more than two different wave-lengths are incident in a nonlinear medium. The energy of the pump with the frequency ω_p is transferred to signal and idler with the frequencies ω_s and ω_i , respectively, and then the signal and idler is amplified by parametric amplification under the relation $\omega_p = \omega_s + \omega_i$. In our system, the soliton is the classical pump, the particle and antiparticle modes behave as signal and idler.

Now, let us begin with the Lagrangian in our system to derive the equation of the motion for the signal and idler. The Lagrangian is given as

$$L = \int_{-\infty}^{\infty} \mathcal{L} dx, \quad (5.53)$$

where the Lagrangian density \mathcal{L} is written as

$$\mathcal{L} = \left(\frac{\hbar}{2e} \right)^2 \left[\frac{c_{rh}}{2} (\partial_t \theta)^2 + \frac{c_{lh}}{2} a^2 (\partial_x \partial_t \theta)^2 - \frac{1}{2l_{rh} a^2} a^2 (\partial_x \theta)^2 - \frac{1}{2l_{lh} a^2} \theta^2 - \frac{1}{l_J a^2} (1 - \cos \theta) \right], \quad (5.54)$$

with the capacitance and inductance of the left(right)-handed element per unit length a denoted as $c_{lh}(c_{rh})$ and $l_{lh}(l_{rh})$, respectively as well as l_J being the Josephson inductance per unit length.

Using the Taylor expansion up to the fourth-order for $\cos\theta$ and setting $l_{lh} = -l_J$, we obtain the following Lagrangian

$$\mathcal{L} = \left(\frac{\hbar}{2e}\right)^2 \left[\frac{c_{rh}}{2} (\partial_t\theta)^2 + \frac{c_{lh}}{2} a^2 (\partial_x\partial_t\theta)^2 - \frac{1}{2l_{rh}a^2} a^2 (\partial_x\theta)^2 + \frac{1}{24l_Ja^2} \theta^4 \right]. \quad (5.55)$$

From the Euler-Lagrange equation for the above Lagrangian $L(\theta, \partial_t\theta, \partial_x\theta, \partial_x\partial_t\theta)$ expressed as,

$$\frac{\partial\mathcal{L}}{\partial\theta} - \frac{\partial}{\partial x} \frac{\partial\mathcal{L}}{\partial(\partial_x\theta)} - \frac{\partial}{\partial t} \frac{\partial\mathcal{L}}{\partial(\partial_t\theta)} + \frac{\partial^2}{\partial x\partial t} \frac{\partial\mathcal{L}}{\partial(\partial_x\partial_t\theta)} = 0, \quad (5.56)$$

the wave equation described by Eq. (5.33) can be reproduced.

The canonical momentum π is given by

$$\begin{aligned} \pi(x, t) &= \frac{\delta L}{\delta(\partial_t\theta(x, t))} \\ &= \frac{\partial\mathcal{L}}{\partial(\partial_t\theta(x, t))} - \partial_x \frac{\partial\mathcal{L}}{\partial(\partial_x\partial_t\theta(x, t))} \\ &= \left(\frac{\hbar}{2e}\right)^2 \{c_{rh} (\partial_t\theta) - c_{lh}a^2 (\partial_t\partial_x^2\theta)\}. \end{aligned} \quad (5.57)$$

The Hamiltonian density can be derived by the Legendre transformation from Lagrangian as

$$\mathcal{H} = \left(\frac{\hbar}{2e}\right)^2 \left[\frac{c_{rh}}{2} (\partial_t\theta)^2 + \frac{c_{lh}}{2} a^2 (\partial_x\partial_t\theta)^2 + \frac{1}{2l_{rh}a^2} a^2 (\partial_x\theta)^2 - \frac{1}{24l_Ja^2} \theta^4 \right]. \quad (5.58)$$

Let us explain how Hawking and its partner particle are generated from the vacuum. Suppose that the Josephson phase difference can be represented by the classical value θ_c and quantum fluctuation $\delta\theta$ around it, i.e., $\theta = \theta_c + \delta\theta$. The Hamiltonian density can be divided into three parts by ignoring the small values $O(\delta\theta^3)$ as follows

$$\mathcal{H} = \mathcal{H}_c + \mathcal{H}_q + \mathcal{H}_{int}, \quad (5.59)$$

where \mathcal{H}_c and \mathcal{H}_q are the Hamiltonian density for a classical phase variable and its quantum fluctuation, respectively

$$\mathcal{H}_c = \left(\frac{\hbar}{2e}\right)^2 \left[\frac{c_{rh}}{2} (\partial_t\theta_c)^2 + \frac{c_{lh}}{2} a^2 (\partial_x\partial_t\theta_c)^2 + \frac{1}{2l_{rh}a^2} a^2 (\partial_x\theta_c)^2 - \frac{1}{24l_Ja^2} \theta_c^4 \right], \quad (5.60)$$

$$\mathcal{H}_q = \left(\frac{\hbar}{2e}\right)^2 \left[\frac{c_{rh}}{2} (\partial_t\delta\theta)^2 + \frac{1}{2l_{rh}a^2} a^2 (\partial_x\delta\theta)^2 \right]. \quad (5.61)$$

The interaction Hamiltonian density \mathcal{H}_{int} arising from the fourth-order nonlinearity will be discussed later. The Hamiltonian density for quantum fluctuation is rewritten as

$$\mathcal{H}_q = \frac{1}{2} c_{rh} d_{eff}^2 (E^2 + c^2 B^2), \quad (5.62)$$

through the Josephson relations

$$\partial_t(\delta\theta) = \frac{2e}{\hbar}V, \quad (5.63)$$

$$\partial_x(\delta\theta) = \frac{2e}{\hbar}d_{eff}B, \quad (5.64)$$

where d_{eff} is the effective barrier thickness of the junction and B is the magnetic flux density. This represents exactly the Hamiltonian of electromagnetic waves. Therefore, the fluctuations of the Josephson phase generate electromagnetic waves. This is a source of Hawking radiation in our system.

Let us get back to the derivation of the equation of motion for the parametric amplification. The Hamiltonian is separated by the linear part H_0 and nonlinear one H_1 that can induce the parametric amplification as follows,

$$H = \int_{-\infty}^{\infty} \mathcal{H} dx = H_0 + H_1, \quad (5.65)$$

where

$$H_0 = \int_{-\infty}^{\infty} dx \left(\frac{\hbar}{2e} \right)^2 \left[\frac{c_{rh}}{2} (\partial_t\theta)^2 + \frac{c_{lh}}{2} a^2 (\partial_x\partial_t\theta)^2 + \frac{1}{2l_{rh}a^2} a^2 (\partial_x\theta)^2 \right], \quad (5.66)$$

$$H_1 = - \int_0^z dx \left(\frac{\hbar}{2e} \right)^2 \left[\frac{1}{24l_J a^2} \theta^4 \right]. \quad (5.67)$$

Particles and antiparticles can be pair-produced anywhere along the transmission line, but let us set $x = 0$ where the pair-production occurs and consider its amplification at $x = z$. The Poisson bracket between θ and π is given as

$$\begin{aligned} \{\theta(x, t), \pi(y, t)\} &= \int dz \left(\frac{\delta\theta(x, t)}{\delta\theta(z, t)} \frac{\delta\pi(y, t)}{\delta\pi(z, t)} - \frac{\delta\pi(y, t)}{\delta\theta(z, t)} \frac{\delta\theta(x, t)}{\delta\pi(z, t)} \right) \\ &= \int dz \delta(x - z) \delta(y - z) \\ &= \delta(x - y). \end{aligned} \quad (5.68)$$

According to the conventional quantization procedure, it is canonically quantized with the commutation relation as

$$\left[\hat{\theta}(x, t), \hat{\pi}(y, t) \right] = i\hbar\delta(x - y). \quad (5.69)$$

Based on the plane-waves modes decomposition, the phase difference operator is expressed as

$$\hat{\theta}(x, t) = \int_{-\infty}^{\infty} dk \frac{2e}{\hbar} \sqrt{\frac{\hbar\omega(k)l_{rh}}{4\pi k^2}} \left[\hat{a}_k e^{i(kx - \omega(k)t)} + \hat{a}_k^\dagger e^{-i(kx - \omega(k)t)} \right], \quad (5.70)$$

where \hat{a}_k and \hat{a}_k^\dagger are the creation and annihilation operators and the commutation relations obey

$$\left[\hat{a}_k, \hat{a}_{k'}^\dagger \right] = \delta(k - k'), \quad (5.71)$$

$$\left[\hat{a}_k, \hat{a}_{k'} \right] = \left[\hat{a}_k^\dagger, \hat{a}_{k'}^\dagger \right] = 0. \quad (5.72)$$

The linear Hamiltonian is diagonalized as

$$\hat{H}_0 = \int_{-\infty}^{\infty} dk \hbar \omega(k) \hat{a}_k^\dagger \hat{a}_k, \quad (5.73)$$

where the zero-point energy is ignored. The field is considered as a set of an infinite number of harmonic oscillators with the frequencies $\omega(k)$.

Assuming that the pump is strong enough to be treated as classical value, we replace $\hat{a}_k \rightarrow \hat{a}_k + b(\omega(k))$ with the complex function $b(\omega(k))$ centered at $\omega_p = \omega(\bar{k}_p)$. Equation (5.70) becomes

$$\hat{\theta}(x, t) = \int_{-\infty}^{\infty} dk c(k) \left[\{\hat{a}_k + b(\omega(k))\} e^{i(kx - \omega(k)t)} + \{\hat{a}_k^\dagger + b^*(\omega(k))\} e^{-i(kx - \omega(k)t)} \right], \quad (5.74)$$

where

$$c(k) = \frac{2e}{\hbar} \sqrt{\frac{\hbar \omega(k) l_{rh}}{4\pi k^2}}. \quad (5.75)$$

In the rotating wave approximation, the nonlinear Hamiltonian is composed of three parts as

$$\hat{H}_1(t) = \hat{H}_{CPM}(t) + \hat{H}_{SQ} + H_{SPM}(t), \quad (5.76)$$

where the first part represents the cross-phase modulation

$$\begin{aligned} \hat{H}_{CPM}(t) = \frac{8}{24l_J} \left(\frac{\hbar}{2e} \right)^2 \int_0^\infty dk_s dk_i dk_p dk_{p'} c(k_s) c(k_i) c(k_p) c(k_{p'}) b^*(\omega(k_p)) b(\omega(k_{p'})) \\ \hat{a}_{k_s}^\dagger \hat{a}_{k_i} e^{i(\omega(k_s) - \omega(k_i) + \omega(k_p) - \omega(k_{p'}))t} \int_0^z dx e^{-i(k_s - k_i + k_p - k_{p'})x} + H.c., \end{aligned} \quad (5.77)$$

the second one is broadband squeezing

$$\begin{aligned} \hat{H}_{SQ}(t) = -\frac{4}{24l_J} \left(\frac{\hbar}{2e} \right)^2 \int_0^\infty dk_s dk_i dk_p dk_{p'} c(k_s) c(k_i) c(k_p) c(k_{p'}) b(\omega(k_p)) b(\omega(k_{p'})) \\ \hat{a}_{k_s}^\dagger \hat{a}_{k_i}^\dagger e^{i(\omega(k_s) - \omega(k_p) + \omega(k_i) - \omega(k_{p'}))t} \int_0^z dx e^{-i(k_s - k_p + k_i - k_{p'})x} + H.c., \end{aligned} \quad (5.78)$$

and the last one describes the self-phase modulation

$$\begin{aligned} H_{SPM}(t) = -\frac{2}{24l_J} \left(\frac{\hbar}{2e} \right)^2 \int_0^\infty dk_s dk_i dk_p dk_{p'} c(k_s) c(k_i) c(k_p) c(k_{p'}) b^*(\omega(k_p)) b(\omega(k_{p'})) \\ b^*(\omega(k_s)) b(\omega(k_i)) e^{i(\omega(k_s) - \omega(k_i) + \omega(k_p) - \omega(k_{p'}))t} \int_0^z dx e^{-i(k_s - k_i + k_p - k_{p'})x} + H.c.. \end{aligned} \quad (5.79)$$

Here, we discuss the Hamiltonian in the interaction picture. Note that our Hamiltonian is composed of the time-independent unperturbed Hamiltonian \hat{H}_0 and time-dependent perturbed Hamiltonian \hat{H}_1 . The annihilation operator $\hat{a}_k(t)$ evolves as

$$\hat{a}_k(t) = \hat{u}_0^\dagger(t) \hat{a}_k \hat{u}_0(t), \quad (5.80)$$

The differential equation is obtained as follows,

$$\begin{aligned}\frac{\partial \hat{a}_k(t)}{\partial t} &= \frac{i}{\hbar} [\hat{H}_0, \hat{a}_k(t)] \\ &= -i\omega(k)\hat{a}_k(t),\end{aligned}\quad (5.81)$$

and it can be solved as

$$\hat{a}_k(t) = e^{-i\omega(k)t}\hat{a}_k(t_0), \quad (5.82)$$

where t_0 is the initial time of the interaction. The time evolution of \hat{H}_1 is written as

$$\begin{aligned}\hat{H}_1^{int}(t) &= \hat{u}_0^\dagger(t)\hat{H}_1(t)\hat{u}_0(t) \\ &= \hat{H}_{CPM}^{int}(t) + \hat{H}_{SQ}^{int}(t) + H_{SPM}(t),\end{aligned}\quad (5.83)$$

where

$$\begin{aligned}\hat{H}_{CPM}^{int}(t) &= \hat{u}_0^\dagger(t)\hat{H}_{CPM}(t)\hat{u}_0(t) \\ &= -\frac{8}{24l_J a^2} \left(\frac{\hbar}{2e}\right)^2 \int_{-\infty}^{\infty} dk_s dk_i c(k_s) c(k_i) c^2(\bar{k}_p) |b(\omega(\bar{k}_p))|^2 e^{2i(\omega(k_s)-\omega(k_i))t} \\ &\quad \times \int_0^z dx e^{-i(k_s-k_i)x} \hat{a}_{k_s}^\dagger(t_0)\hat{a}_{k_i}(t_0) + H.c.,\end{aligned}\quad (5.84)$$

$$\begin{aligned}\hat{H}_{SQ}^{int}(t) &= \hat{u}_0^\dagger(t)\hat{H}_{SQ}(t)\hat{u}_0(t) \\ &= -\frac{4}{24l_J a^2} \left(\frac{\hbar}{2e}\right)^2 \int_{-\infty}^{\infty} dk_s dk_i c(k_s) c(k_i) c^2(\bar{k}_p) b^2(\omega(\bar{k}_p)) e^{2i(\omega(k_s)+\omega(k_i)-\omega(\bar{k}_p))t} \\ &\quad \times \int_0^z dx e^{-i(k_s+k_i-2\bar{k}_p)x} \hat{a}_{k_s}^\dagger(t_0)\hat{a}_{k_i}^\dagger(t_0) + H.c.,\end{aligned}\quad (5.85)$$

and

$$\begin{aligned}H_{SPM}(t) &= -\frac{2}{24l_J} \left(\frac{\hbar}{2e}\right)^2 \int_0^\infty dk_s dk_i c(k_s) c(k_i) c^2(\bar{k}_p) |b(\omega(\bar{k}_p))|^2 \\ &\quad \times b^*(\omega(k_s)) b(\omega(k_i)) e^{i(\omega(k_s)-\omega(k_i))t} \int_0^z dx e^{-i(k_s-k_i)x} + H.c.,\end{aligned}\quad (5.86)$$

in the monochromatic degenerate pump limit, i.e. $b(\omega(k_{p'})) = b(\omega(k_p)) \rightarrow b(\omega(k_p)) \delta(k_p - \bar{k}_p)$.

The asymptotic output field is defined as

$$\hat{a}_k^{out} = \hat{U}\hat{a}_k(t_0)\hat{U}^\dagger, \quad (5.87)$$

where we set initial time $t_0 = -\infty$ and the final time $t_1 = \infty$ of the interaction. The asymptotic evolution operator is given as

$$\hat{U} \equiv \hat{U}(-\infty, \infty) = e^{-\frac{i}{\hbar}\hat{K}_1}, \quad (5.88)$$

with

$$\hat{K}_1 = \int_{-\infty}^{\infty} \hat{H}_1(t) dt = \hat{K}_{CPM} + \hat{K}_{SQ} + K_{SPM}, \quad (5.89)$$

where the time ordering does not need to be considered since $[\hat{H}_1(t), \hat{H}_1(t')] = 0$. Each part of \hat{K}_1 is derived as

$$\hat{K}_{CPM} = -\frac{32\pi}{24l_J} \left(\frac{\hbar}{2e}\right)^2 z \int_0^{\infty} dk_s c^2(k_s) c^2(\bar{k}_p) |b(\omega(\bar{k}_p))|^2 \hat{a}_{k_s}^\dagger(t_0) \hat{a}_{k_s}(t_0), \quad (5.90)$$

$$\hat{K}_{SQ} = -\frac{8\pi}{24l_J} \left(\frac{\hbar}{2e}\right)^2 \int_0^{\infty} dk_s c(k_s) c(k_i) c^2(\bar{k}_p) b^2(\omega(\bar{k}_p)) \hat{a}_{k_s}^\dagger(t_0) \hat{a}_{k_i}^\dagger(t_0) \frac{e^{i\Delta k z} - 1}{i\Delta k} + H.c., \quad (5.91)$$

and

$$K_{SPM} = -\frac{8\pi}{24l_J} \left(\frac{\hbar}{2e}\right)^2 c^4(\bar{k}_p) |b(\omega(\bar{k}_p))|^4 z, \quad (5.92)$$

where $\omega(k_i) = \omega(\bar{k}_p) - \omega(k_s)$ and $\Delta k = 2\bar{k}_p - k_s - k_i$.

Defining the initial creation and annihilation operator as $\hat{a}_{k_s(i)}(t_0) \equiv \hat{a}_{k_s(i)}$ and $\hat{a}_{k_s(i)}^\dagger(t_0) \equiv \hat{a}_{k_s(i)}^\dagger$, respectively, Eq. (5.87) is rewritten as

$$\hat{a}_k = \hat{U}^\dagger \hat{a}_k^{out} \hat{U}. \quad (5.93)$$

By the differential for z , the equation of motion for $\hat{a}_{k_s(i)}$ is derived as

$$\frac{d\hat{a}_{k_s(i)}}{dz} = \frac{i}{\hbar} \left[\frac{d\hat{K}_1}{dz}, \hat{a}_{k_s(i)} \right]. \quad (5.94)$$

After some calculations, this leads to

$$\frac{d\hat{a}_{k_s(i)}}{dz} = \frac{il_{rh}}{6l_J a^2} \left(2 \frac{\omega(k_s)}{k_s^2} |\beta_p|^2 \hat{a}_{k_s(i)} + \sqrt{\frac{\omega(k_s)\omega(k_i)}{k_s^2 k_i^2}} \beta_p^2 e^{i\Delta k z} \hat{a}_{k_i(s)}^\dagger \right), \quad (5.95)$$

where $\beta_p \equiv c(\bar{k}_p) b(\omega(\bar{k}_p))$. In the corotating-framework, replacing the fields with

$$\hat{a}_{k_s(i)} = \hat{\tilde{a}}_{k_s(i)} e^{2i\gamma\omega(k_s(i))|\beta_p|^2 z/k_s^2(i)}, \quad (5.96)$$

and

$$\beta_p = \tilde{\beta}_p e^{i\gamma\omega(\bar{k}_p)|\beta_p|^2 z/\bar{k}_p^2}, \quad (5.97)$$

where $\gamma = l_{rh}/(6l_J a^2)$, Eq. (5.95) becomes

$$\frac{\partial \hat{\tilde{a}}_{k_s(i)}}{\partial z} = i\gamma \sqrt{\frac{\omega(k_s)\omega(k_i)}{k_s^2 k_i^2}} \tilde{\beta}_p^2 \hat{\tilde{a}}_{k_i(s)}^\dagger e^{i\Psi z}, \quad (5.98)$$

with the total phase mismatch

$$\Psi = \Delta k + 2\gamma \left(\frac{\omega(\bar{k}_p)}{\bar{k}_p^2} - \frac{\omega(k_s)}{k_s^2} - \frac{\omega(k_i)}{k_i^2} \right) |\beta_p|^2. \quad (5.99)$$

Solving Eq. (5.98), we obtain

$$\hat{a}_{k_{s(i)}}(z) = e^{i\frac{\Psi}{2}z} \left[i\frac{\gamma}{g} \sqrt{\frac{\omega(k_s)\omega(k_i)}{k_s^2 k_i^2}} \tilde{\beta}_p^2 \hat{a}_{k_{i(s)}}^\dagger \sinh gz + \hat{a}_{k_{s(i)}} \left(-\frac{i\Psi}{2g} \sinh gz + \cosh gz \right) \right], \quad (5.100)$$

where

$$g = \sqrt{\gamma^2 \frac{\omega(k_s)\omega(k_i)}{k_s^2 k_i^2} |\tilde{\beta}_p|^4 - \left(\frac{\Psi}{2}\right)^2}. \quad (5.101)$$

At $\Psi = 0$, this becomes

$$\hat{a}_{k_{s(i)}}(z) = i\hat{a}_{k_{i(s)}}^\dagger \sinh gz + \hat{a}_{k_{s(i)}} \cosh gz, \quad (5.102)$$

which means that the signal \hat{a}_{k_s} and idler \hat{a}_{k_i} are amplified. This is exactly the Bogoliubov transformation represented by

$$\begin{aligned} \begin{pmatrix} \hat{a}_{k_s}(L) \\ \hat{a}_{k_i}^\dagger(L) \end{pmatrix} &\equiv U_\zeta \begin{pmatrix} \hat{a}_{k_s} \\ \hat{a}_{k_i}^\dagger \end{pmatrix} U_\zeta^\dagger \\ &= \begin{pmatrix} \cosh gz & e^{i\pi/2} \sinh gz \\ e^{-i\pi/2} \sinh gz & \cosh gz \end{pmatrix} \begin{pmatrix} \hat{a}_{k_s} \\ \hat{a}_{k_i}^\dagger \end{pmatrix}, \end{aligned} \quad (5.103)$$

where

$$U_\zeta = \exp \left\{ \zeta \left(\hat{a}_{k_s} \hat{a}_{k_i} e^{-i\pi/2} - \hat{a}_{k_s}^\dagger \hat{a}_{k_i}^\dagger e^{i\pi/2} \right) \right\}, \quad (5.104)$$

with the squeezing parameter $\zeta = gL$ and the distance between horizons L . The Bogoliubov transformation mixes creation and annihilation operators of the two different modes.

The parametric amplification occurs everywhere in our system. However, only the particles and antiparticles that are pair-generated near the horizon survive and are amplified without being offset because the horizons behave as a resonator. The particle and antiparticle modes corresponding to the signal and idler are amplified by gaining the energy of the soliton corresponding to the pump. Therefore, the soliton gradually decays and disappears in the end. This is an analogy of the evaporation of a black hole. In this thesis, we consider the steady state before decaying.

In the following, we incorporate the nonlinear mode conversions near the event horizon by adopting the model considered by Leonhardt et al. [65] from the standpoint of nonlinear quantum optics and then find that our laser is a squeezed state laser. Figure 5.14 represents the trajectories of modes with the operators. Consider the m th amplification process in the horizon cavity. The two modes pair produced by mode conversion (B_1) at the black hole horizon propagate toward the white hole horizon (B_2). At the white hole horizon, the two modes again undergo a time-reversed mode conversion (B_3) opposite to the previous one and then propagate toward the departed black

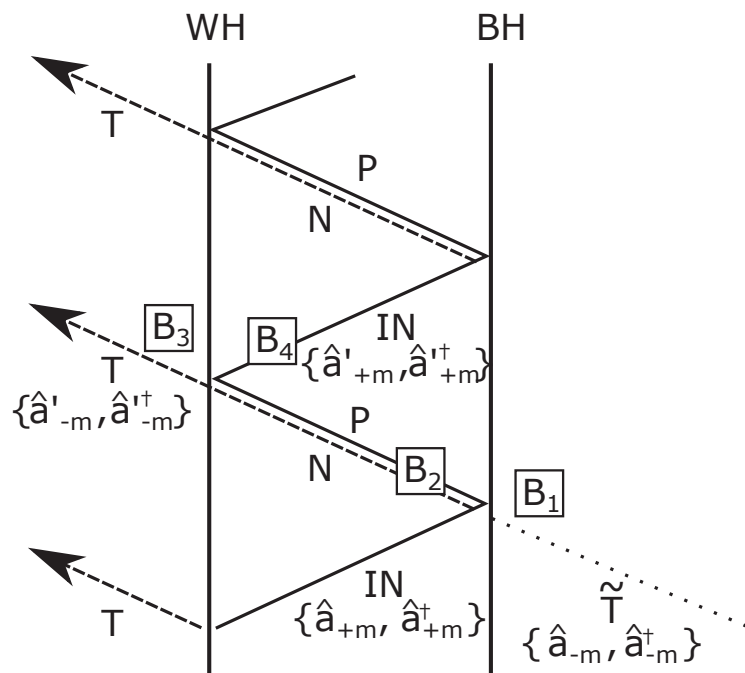


Figure 5.14: Sketch of the trajectories of modes. The solid (dashed) lines represent the mode with positive (negative) frequencies for particles (antiparticles). The dotted line is a virtual input mode for antiparticles.

hole horizon (B_4). These four distinct processes are incorporated in the matrix B , allowing it to be expressed as

$$B = B_4 B_3 B_2 B_1, \quad (5.105)$$

where

$$B_1 = \begin{pmatrix} \cosh \zeta & -\sinh \zeta \\ -\sinh \zeta & \cosh \zeta \end{pmatrix}, \quad (5.106)$$

$$B_2 = \begin{pmatrix} e^{-i\theta_-} & 0 \\ 0 & e^{i\theta_+} \end{pmatrix}, \quad (5.107)$$

$$B_3 = \begin{pmatrix} \cosh \zeta & \sinh \zeta \\ \sinh \zeta & \cosh \zeta \end{pmatrix}, \quad (5.108)$$

$$B_4 = \begin{pmatrix} e^{-i\theta_0} & 0 \\ 0 & 1 \end{pmatrix}, \quad (5.109)$$

with the phases θ_0 , θ_- and θ_+ acquired during propagation for each mode. As a result, the input modes at the m th amplification process are transformed to the output modes by a Bogoliubov transformation B as follows,

$$\begin{pmatrix} \hat{a}'_{-m} \\ \hat{a}'_{+m} \end{pmatrix} = B \begin{pmatrix} \hat{a}_{-m} \\ \hat{a}_{+m} \end{pmatrix}, \quad (5.110)$$

where $\hat{a}_{+(-)m}$ ($\hat{a}_{+(-)m}^\dagger$) represents annihilation (creation) operator of the m th input mode for particles (antiparticles), while $\hat{a}'_{+(-)m}$ ($\hat{a}'_{+(-)m}^\dagger$) are those of output modes for particles (antiparticles). The output modes serve as further input modes ($\hat{a}'_{+m} = \hat{a}_{+(m+1)}$). As shown in Fig. 5.14, the virtual antiparticle in the \tilde{T} mode incident from the right side of the black hole event horizon and the particle in the IN mode inside the cavity are input modes, while the antiparticle in the outgoing T mode and the particle in the IN mode are output modes.

The transfer matrix B essentially represents squeezing transformation. Therefore, the laser discussed here is nothing but a *squeezed state laser*. The squeezing parameter ζ is given by

$$\tanh^2 \zeta = e^{-\frac{\hbar\omega}{k_B T_H}}, \quad (5.111)$$

where k_B is the Boltzmann constant and T_H is the Hawking temperature which is proportional to the gradient of the velocity as follows [50],

$$T_H = \frac{\hbar}{2\pi k_B} \left| \frac{\partial v_g^{\text{eff}}}{\partial \eta} \right|_{\eta=\eta_h}, \quad (5.112)$$

where

$$\left| \frac{\partial v_g^{\text{eff}}}{\partial \eta} \right|_{\eta=\eta_h} = \frac{4A\delta n(\eta_h)}{c} \sqrt{\left| \frac{Q}{2P} \right|} \tanh \left(A \sqrt{\left| \frac{Q}{2P} \right|} \eta_h \right) u^2. \quad (5.113)$$

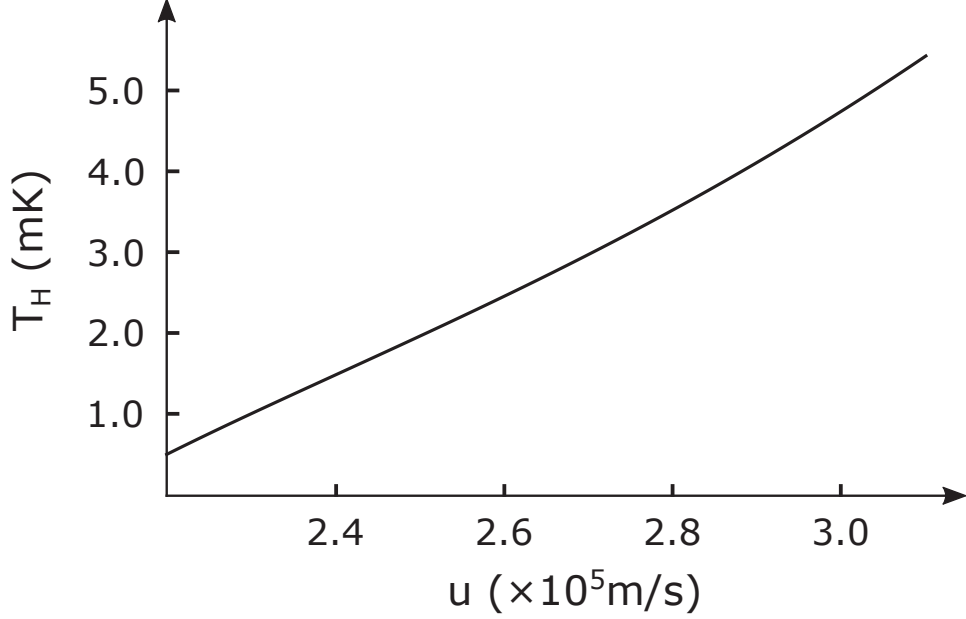


Figure 5.15: The dependence of the Hawking temperature T_H on the relative soliton velocity u . We set the circuit parameters as $L_{rh} = 4 \times 10^{-8}$ H, $C_{rh} = 2.5 \times 10^{-16}$ F, $\gamma = 5000$, $I_c = 10^{-8}$ A, $\omega_0 = 2 \times 10^8$ Hz, $\omega_s = 4.4 \times 10^9$ Hz, and $a = 10^{-6}$ m.

The Hawking temperature depends on the relative soliton velocity u as depicted in Fig. 5.15. The Hawking temperature reaches the well-observable milli-Kelvin order under the circuit parameters feasible with current technology.

The number of antiparticles outside the horizon after m steps amplified by our black hole laser is estimated as

$$\begin{aligned} \langle \hat{N}_{-m} \rangle &= \langle \hat{a}_{-m}^\dagger \hat{a}'_{-m} \rangle \\ &= |\mu|^{2m} (1 - |\mu|^{-2}), \end{aligned} \quad (5.114)$$

where

$$|\mu|^2 = \frac{1}{2} [1 + \cosh^2(2\zeta) - \cos(\theta_+ + \theta_-) \sinh^2(2\zeta)], \quad (5.115)$$

under the reformed Bogoliubov transformation operator

$$B = e^{i\psi} \begin{pmatrix} \mu & \nu^* \\ \nu & \mu^* \end{pmatrix}, \quad (5.116)$$

with $|\mu|^2 - |\nu|^2 = 1$ and ψ is real. The amplification of the number of partner Hawking particles with each bounce process at the black hole horizon is depicted in Fig. 5.16 for the resonant case with $\cos(\theta_+ + \theta_-) = 0$. This typical enhancement shows surely lasing. Therefore, the resulting Hawking radiation is a squeezed state laser with squeezing parameters due to the nonlinearity of solitons.

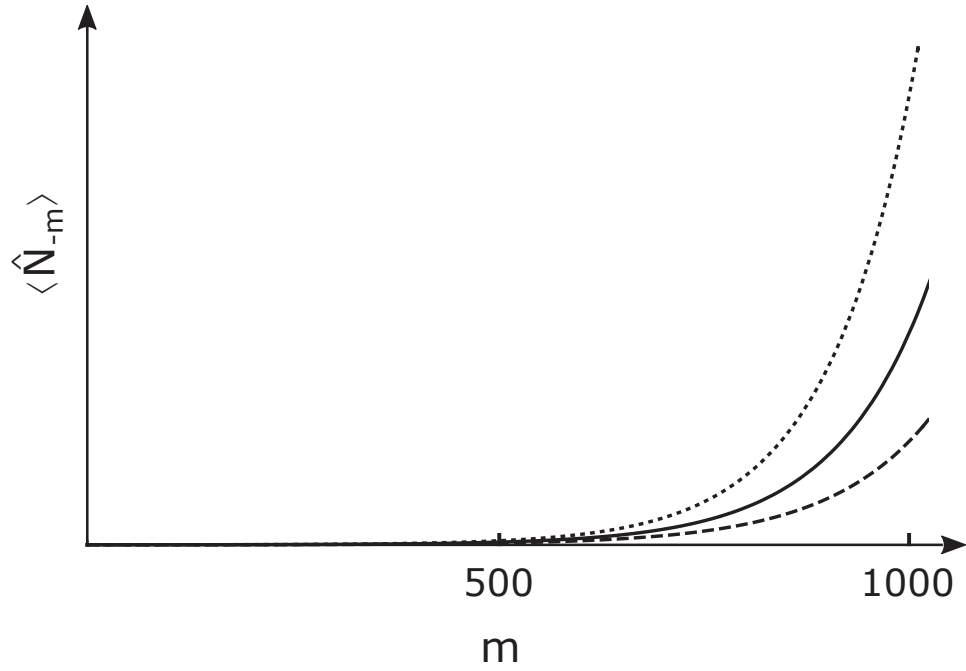


Figure 5.16: The number of outgoing antiparticles as a function of the amplification steps at the fixed relative soliton velocities $u = 2.99 \times 10^5 \text{m/s}$ (dotted line), $u = 3.00 \times 10^5 \text{m/s}$ (solid line) and $u = 3.01 \times 10^5 \text{m/s}$ (dashed line). The circuit parameters are the same as in Fig. 5.15.

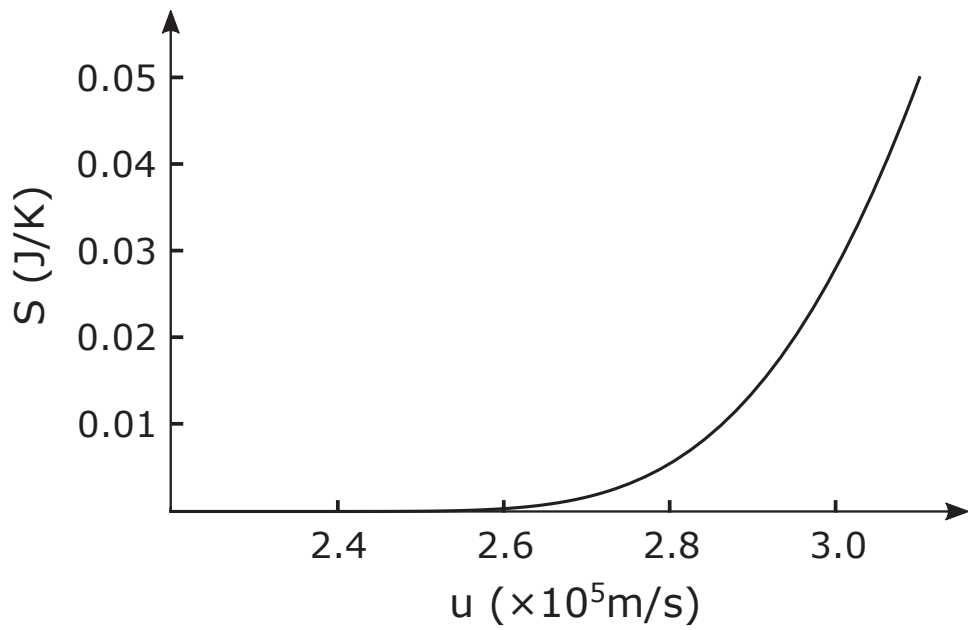


Figure 5.17: The dependence of the entanglement entropy S on the relative soliton velocity u . The circuit parameters are the same as in Fig. 5.15.

5.5 Entanglement entropy

Hawking radiation originates from pair production from the vacuum inside near the horizon. The produced particle and antiparticle are inherently entangled with each other. Therefore, the detection of this entanglement is indispensable for the confirmation of Hawking radiation. However, it is unlikely to confirm the entanglement by conventional detection methods utilizing simultaneous observation of particle-antiparticle pairs because of the difficulty of detecting partner particles left inside the horizon cavity. Here, we evaluate it using entanglement entropy thanks to the fact that an entangled particle bears the shadow of its partner particle. Entanglement entropy is a measure of quantum correlation between two particles labeled A and B and is defined by $S(\rho_A) = -\text{Tr}[\rho_A \log \rho_A]$ where $\rho_A = \text{Tr}_B(\rho_{AB})$ is the reduced density matrix of a pure state density matrix ρ_{AB} . Therefore, the degree of entanglement can be evaluated without simultaneous observation of the partner particles.

Fortunately, our black hole laser is a laser with a two-mode squeezed state due to Hawking radiation and its partner. The quantum correlation between the two modes is naturally incorporated into the squeezed parameter. This squeezing parameter is responsible for the quantum correlation with unobservable partner particles trapped in the cavity. The entanglement entropy for the two-mode squeezed states is given in the well-known form [66, 67] as

$$S = 2k_B [\cosh^2 \zeta \ln (\cosh^2 \zeta) - \sinh^2 \zeta \ln (\sinh^2 \zeta)]. \quad (5.117)$$

Note that the entanglement entropy depends on the relative soliton velocity u as shown in Fig. 5.17 since the squeezing parameter ζ involves the Hawking temperature depending on the soliton velocity. This soliton velocity dependence provides useful evidence for identifying the detected laser as being derived from Hawking radiation.

5.6 Summary

In this chapter, we have proposed the black hole laser in the electric circuit. The black hole laser is an analogue gravity-derived laser that amplifies Hawking photons generated from vacuum fluctuations inside near the event horizon in a cavity formed by two horizons viewed as mirrors. It requires Hawking-related propagation modes with positive (particle) and negative (antiparticle) frequencies, which can be generated by using anomalous dispersion for example, in an analogue resonator. We have applied dispersion engineering that deforms the dispersion relation by adding metamaterial elements to ordinary transmission lines in order to realize Hawking-related modes despite the ordinary dispersion relation in the transmission line. In addition, the third-order Kerr effect through the Josephson nonlinear inductance is introduced to control those modes. Based on these, we have proposed an *optical analogue* black hole laser in a Josephson transmission line with metamaterial elements. Unlike previous optical black hole lasers, our black hole laser still has a black hole/white hole cavity formed within a *single dark* soliton, where Hawking radiation is emitted into the normal region outside of solitons rather than inside of solitons. This selection can be achieved by controlling the Kerr effect through Josephson nonlinear inductance. Unfortunately, Hawking radiation obtained here has a negative frequency due to normal dispersion like an optical black hole laser and is different from actual Hawking radiation with a positive frequency. This will be solved if anomalous dispersion can be introduced in the transmission line.

We have also shown that our laser is a squeezed state laser based on Leonhardt's quantum optical treatment of mode conversions in the horizon. This facilitates the analysis of the quantum

entanglement required to identify the origin of Hawking radiation. In particular, entanglement entropy, which measures the degree of entanglement, is very effective when direct observation of partner radiation is difficult. The resulting entanglement entropy was found to be characterized by a squeezed parameter defined by the Hawking temperature that depends on the soliton velocity. It can be proved that Hawking radiation is strongly related to the soliton providing the analogue horizon if the entanglement entropy involved in this soliton velocity can be evaluated.

Black hole lasers have not been discussed in superconducting transmission lines so far. However, there are some advantages to the study of black hole lasers due to the latest technology accumulated in research such as quantum computers. In particular, the scalability and controllability of the system is an advantage over other systems. In addition, the detection of microwave photons and their quantum correlations in Josephson transmission lines has been proven through the study of the dynamical Casimir effect [20]. The observation of Hawking radiation is also highly promising if our proposal is implemented.

Chapter 6

Conclusion

6.1 Summary and conclusion

Observation of Hawking radiation, which is a quantum phenomenon in gravity, is a key to unifying general relativity and quantum mechanics. However, it is extremely difficult to observe Hawking radiation from an actual black hole because it is much smaller than the background radiation in the universe. There are proposals of analogue black holes to explore it with observable Hawking temperature in laboratory systems instead.

In electrical circuits, analogue black holes have been proposed by using the spatial changes in the circuit parameters (inductance or capacitance) which cause the spatial varying velocity of the electromagnetic waves. However, there are serious problems in modulating the circuit parameters, such as unstable control of the external field or overheating the circuit.

6.1.1 Analogue Hawking radiation

In this study, we have proposed analogue black holes induced by solitons propagating on the transmission lines to overcome the problems mentioned above. We have introduced the nonlinearity to the circuit parameters on transmission lines and derived solitons using the reductive perturbation method by focusing on the waves with the balance between the nonlinearity and the dispersion. In the Josephson transmission lines with nonlinear inductance, we have obtained the defocusing (negative) modified Korteweg de Vries (mKdV) equation with the current soliton solution. On the other hand, in the nonlinear LC transmission lines with nonlinear capacitance, we have shown the existence of the voltage solitons obeying the nonlinear Schrödinger equation. The velocity of the electromagnetic waves is modulated by the solitons, resulting in the generation of analogue black holes. In addition, we have derived the Hawking temperature based on the tunneling mechanism for Hawking radiation, supposed that particles are pair-generated by the quantum fluctuations around the classical soliton and passes across the horizon of an analogue black hole. We have evaluated the observability of Hawking radiation in terms of the Hawking temperature and clarified that it is on the order of milli-Kelvin, which is sufficient to be observable. We have also revealed the dynamical contribution of the soliton. This indicates that the Hawking temperature can be controlled simply by changing the soliton velocity without changing the circuit parameters at all. Therefore, this change allows us to confirm that the radiation detected in the experiment is indeed due to Hawking radiation. This is an advantageous feature that has never existed before.

6.1.2 Quantum-circuit black hole lasers

To further amplify Hawking radiation, black hole lasers with a pair of horizons acting as a resonator have been proposed in various systems. However, there are no proposals in the electric circuits due to the lack of anomalous dispersion required for black hole lasers. In this study, we succeeded in constructing a theory of analogue black hole laser in an electric circuit for the first time by proposing a Josephson transmission line using metamaterial elements. We have revealed that there is a phase soliton that obeys a nonlinear Schrödinger equation in the circuit equation by using the reductive perturbation method. The phase soliton spatially modulates the refractive index in proportion to the square of the norm of the electric field through the Kerr effects caused by the nonlinearity of the Josephson inductance. This changes the velocity of electromagnetic waves inside the soliton, and traps the electromagnetic waves, resulting in the creation of a black hole-white hole pair within the soliton. We have shown that these horizons behave like a resonator by introducing the metamaterial elements which control the dispersion relation. The control of the dispersion relation realizes the black hole lasers even though the system has the normal dispersion. There are modes corresponding to particles and antiparticles, and the particle modes are trapped between the horizons while some antiparticle modes are emitted as anti-Hawking radiation from the white hole horizon. We have clarified that the Hawking radiation is exponentially amplified by the parametric amplification as well as the nonlinear mode conversions at the horizons. Unlike black hole lasers in optical fibers, our black hole lasers have both a black hole and a white hole horizon within a single dark soliton and the radiation is emitted into the normal region outside the soliton rather than inside. Therefore, it is easy to observe Hawking radiation. We have also shown that our laser is a squeezed-state laser based on Leonhardt's quantum optical treatment of mode conversions in the horizon. We have also estimated the entanglement entropy, which represents the degree of entanglement, and found that it depends on the soliton velocity. This dependence is one clear evidence for the identification of Hawking radiation.

6.2 Features and impacts

Analogue black holes in electric circuits have advantages over other systems, such as high-precision electromagnetic detection. Our study is an extension of the previous studies, but is unique in that analogue black holes are solitons in electric circuits. As a result, it can be expected that the Hawking temperature can be controlled by changing only the soliton characteristics such as the soliton velocity without changing the parameters of the circuit at all.

This study makes it possible to explore the characteristics of black holes, such as the dynamical behaviors of black holes and their birth (quantum generation), which have not been able to be investigated with existing systems. Furthermore, our systems are also experimentally feasible because it does not require any special technology for soliton generation and control due to its self-forming ability. Therefore, these systems will bring us to experimentally access various quantum gravity phenomena such as Hawking radiation instead of the cosmic theory (high-energy physics) in which their observations are difficult. We can confirm the basic principle of these phenomena with our analogue systems and then feedback to the theory of the universe. In addition, our black hole lasers are expected to be applied to quantum information as a new light source with quantum entanglement. In this way, the impact on both academia and engineering is immeasurable.

6.3 Future prospects

Present problems

In an actual black hole, particles with positive energy are emitted as Hawking radiation while the partner with the negative energy falls into a black hole. However, antiparticles with negative energy are emitted from the white hole horizon in our system of black hole lasers like optical fibers, because it has normal dispersion. This is different from original black hole lasers. The problem will be solved if anomalous dispersion is realized in the transmission lines. We will examine whether such a circuit is feasible. In addition, it is necessary to refine our circuits assuming an experiment in our future works, where we will design the identical circuits using numerical simulation and propose a feasible observation method for Hawking radiation.

Evaporation of black holes

Until now, we have thought that black holes remain unchanged after Hawking radiation. In fact, the black hole loses the energy because of the emissions with positive energy and eventually evaporates after successive Hawking radiation. We are planning to reproduce this evaporation process in our analogue system. Specifically, we consider the effect of dissipation on the black-hole soliton when Hawking particles are emitted outside the soliton. The decay rate of the black hole solitons is analytically derived by considering the dissipation-fluctuation theorem under the semiclassical approximation. In addition, we also perform numerical simulations to check the validity of semiclassical approximation and to investigate the evaporation processes beyond the approximation.

We also plan to study the information paradox based on the formula for the decay process of the black hole solitons. According to the general theory of relativity, a black hole is a local spacetime from which even light cannot escape. Therefore, the information in the black hole cannot go out beyond the event horizon and it seems like a device (a trash can) that erases the information for observers outside the black hole. On the other hand, quantum mechanics predicts that particles are emitted from a black hole as Hawking radiation due to fluctuations in the vacuum. This means that information can be extracted from the black hole. Also, since quantum-mechanical processes are reversible, the information is never lost. In other words, black holes are thought to act as storage devices with a huge storage capacity. The amount of memory is roughly estimated to be 10^{77} bits. The question of whether a black hole is a “trash can” or a “memory” is known as the information paradox of black holes and has plagued physicists for many years. We also try to solve the problem of whether the information is erased or retained by evaluating the entanglement entropy representing the degree of quantum correlation between black hole solitons and emitted particles (Hawking radiation).

Novel phenomena utilizing the dynamic characteristics of solitons

Finally, our challenging goals are directed to study a novel phenomenon that positively utilizes the dynamic characteristics of solitons. One example is the breathing mode between solitons and antisolitons. This causes the event horizon to oscillate in time, resulting in the situation as same as the dynamical Casimir effect induced by oscillations in the spacing of the resonator. Thus, Hawking radiation is expected to be enhanced as the dynamic Casimir effect enhances photon-pair productions. This enhancement will not only increase the observability of Hawking radiation but

also provide a new platform to verify dynamic vacuum fluctuations (dynamic Casimir effect) in an analogue gravitational field.

Appendix A

Designed analogue Black Hole Solitons in Josephson Transmission Lines

In the main text, we clarified the wave nature hidden in the circuit equation by using the reductive perturbation method [33]. As a result, it was found that the defocusing modified Korteweg-de Vries (mKdV) equation is obtained with shock-wave-type soliton solutions in Josephson transmission lines. This is consistent with the numerical results obtained in the previous studies [36] and is the first clarification of the existence of current solitons. In addition, we demonstrated that this current soliton behaves like black holes in the circuit [11, 21]. In the LC circuit, the velocity c of the electromagnetic wave depends on both the inductance L and the capacitance C via $c = a/\sqrt{LC}$ with a being the unit length of the circuit. Current solitons are formed by balancing the nonlinearity of the inductance and the wavenumber dispersion, leading to a spatial change in the velocity of the electromagnetic wave through the nonlinear inductance induced by the current soliton. This eventually produces an analogue black hole in Josephson transmission lines. However, the resulting analogue black hole is spatially restricted by the shape of the soliton, and its configuration cannot be freely controlled. Here, we propose a simple scheme to design the configuration of analogue black holes on demand by combining the solitons and antisolitons.

A.1 Designed analogue black hole solitons

In the main text, we show that a single current soliton produces a pair of analogue black holes in the Josephson transmission line. However, the black holes are located on both sides of the transmission line and cannot be freely changed because they are determined by the shape of the soliton solution. Here we propose a scheme to design the configuration of black holes on demand by combining solitons and antisolitons. Let us consider a pair of analogue black hole solitons created by an approximate solution consisting of a superposition of two single-soliton solutions

$$\bar{I}_{s,s'}(\bar{\eta}) = s\bar{I}(\bar{\eta} + \bar{\Delta}) + s'\bar{I}(\bar{\eta} - \bar{\Delta}), \quad (\text{A.1})$$

where the subscripts specify a soliton ($s, s' = 1$) or an antisoliton ($s, s' = -1$). $\bar{I}(\bar{\eta} \pm \bar{\Delta})$ represents the current soliton with the center position shifted by $\bar{\Delta} = \Delta/a$ expressed as,

$$\bar{I}(\bar{\eta} \pm \bar{\Delta}) = 2\sqrt{3(1 - \bar{v}_s)} \tanh\left[2\sqrt{3(1 - \bar{v}_s)}(\bar{\eta} \pm \bar{\Delta})\right]. \quad (\text{A.2})$$

There are four types of linear combinations of soliton and antisoliton, which are classified into heterogeneous soliton pairs and homogeneous soliton pairs. The electromagnetic wave velocity is modulated by current solitons through the nonlinear inductance in the circuit as follows,

$$\begin{aligned}\bar{c}(\bar{\eta}) &= \sqrt{\cos(\arcsin \bar{I}_{s,s'}(\bar{\eta}))} \\ &= \left[1 - \{s\bar{I}(\bar{\eta} + \bar{\Delta}) + s'\bar{I}(\bar{\eta} - \bar{\Delta})\}^2\right]^{\frac{1}{4}}.\end{aligned}\quad (\text{A.3})$$

The electromagnetic waves with spatially varying velocities generate analogue black holes. Different types of black holes are formed by the heterogeneous soliton pairs and homogeneous soliton pairs.

A.1.1 Heterogeneous soliton pairs

The heterogeneous soliton pairs are the combinations of single soliton and antisoliton ($\bar{I}_{1,-1}$ and $\bar{I}_{-1,1}$) as shown in Fig. A.1 (A) and (B), respectively. They produce the electromagnetic wave with spatially varying velocity as depicted in Fig. A.1 (a) and (b), respectively. The positions of event horizons where the electromagnetic wave velocity equals the soliton velocity are given as

$$\bar{\eta}_h = \pm \frac{1}{2\alpha'} \tanh^{-1} \left[\sqrt{\frac{2 \tanh(\tilde{\Delta}) - w}{\tanh(\tilde{\Delta})(2 - w \tanh(\tilde{\Delta}))}} \right], \quad (\text{A.4})$$

where $\tilde{\Delta} = 2\sqrt{3(1 - \bar{v}_s)}\bar{\Delta}$ and $w = \sqrt{(1 + \bar{v}_s)(1 + \bar{v}_s^2)}/12$. The black holes are located inside the two event horizons, where $|\bar{c}(\bar{\eta})| < |\bar{v}_s|$.

A.1.2 Homogeneous soliton pairs

A pair of homogeneous current soliton is a combination of two solitons $\bar{I}_{1,1}$ or two antisolitons $\bar{I}_{-1,-1}$ as depicted in Fig. A.1 (C) and (D), respectively. They create the spatially varying electromagnetic wave velocity as shown in Fig. A.1 (c) and (d), respectively. The positions of event horizons are given as

$$\bar{\eta}_h = \pm \frac{1}{2\alpha'} \tanh^{-1} \left[\frac{1 - \tanh^2 \tilde{\Delta} - \sqrt{1 + (w^2 - 2) \tanh^2 \tilde{\Delta} + \tanh^4 \tilde{\Delta}}}{w \tanh^2 \tilde{\Delta}} \right]. \quad (\text{A.5})$$

The black holes are generated outside the two event horizons, where $|\bar{c}(\bar{\eta})| < |\bar{v}_s|$.

Heterogeneous soliton pairs and homogeneous soliton pairs produce different types of black holes. Both of these black holes are realized under condition $47/48 \leq \bar{v}_s < 1$ from the real-valued velocity in Eq. (A.3), i. e., $|\bar{I}_{s,s'}(\bar{\eta})| \leq 2 \times 2\sqrt{3(1 - \bar{v}_s)} \leq 1$. The width of black holes is controlled by setting $\tilde{\Delta}$.

A.2 Analogue Hawking radiation

Now, let us discuss analogue Hawking radiation from an analogue black hole formed inside the two event horizons (heterogeneous soliton pairs), which provides a new light source originating from

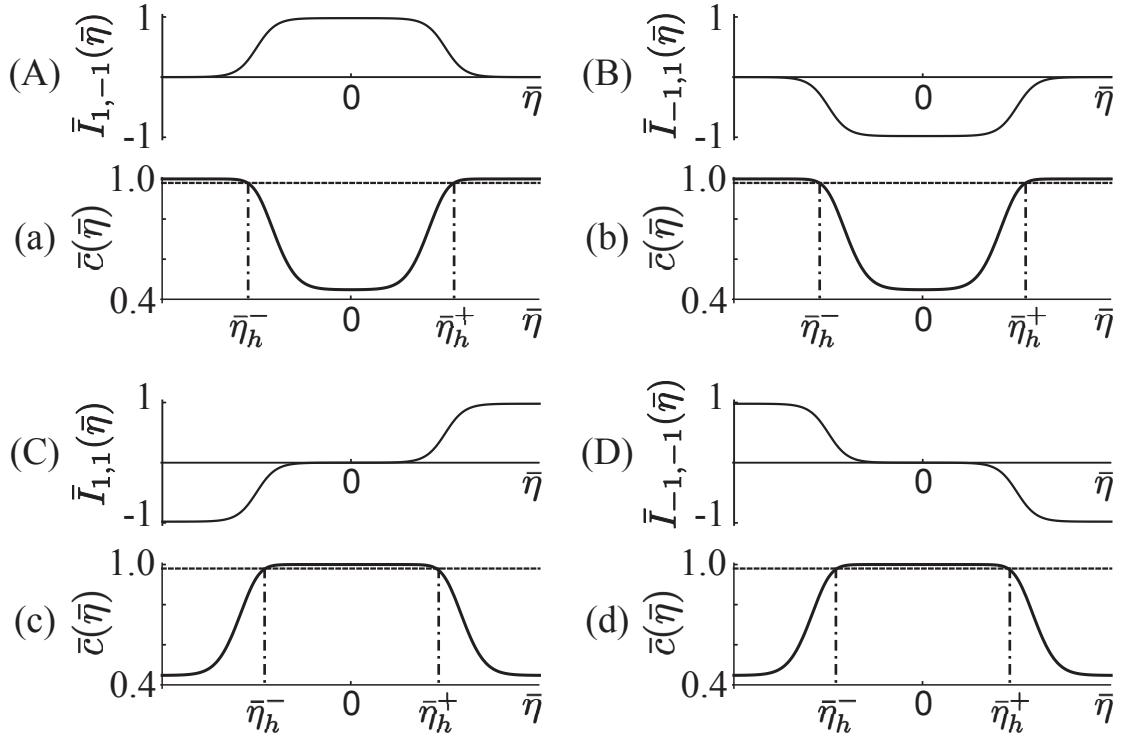


Figure A.1: Normalized current solitons (A) $\bar{I}_{1,-1}$, (B) $\bar{I}_{-1,1}$, (C) $\bar{I}_{1,1}$, and (D) $\bar{I}_{-1,-1}$. The normalized spatially varying electromagnetic wave velocity (a)-(d) induced by current solitons (A)-(D), respectively. The horizontal dotted line indicates the normalized soliton velocity $\bar{v}_s = 0.98$. Two event horizons occur at $\bar{\eta}_h^\pm$.

the quantum fluctuation near the classical solitons in quantum Josephson circuits. The Hawking temperature T_H that characterizes Hawking radiation is given by the formula [50]

$$T_H = \frac{\hbar}{2\pi k_B} \left| \frac{\partial c}{\partial \eta} \right|_{\eta=\eta_h}, \quad (\text{A.6})$$

with the Boltzmann constant k_B . For analogue black holes induced by the heterogeneous soliton pairs, we obtain

$$T_H = \frac{\hbar}{2\pi k_B} \frac{c_0}{a} f(\bar{v}_s), \quad (\text{A.7})$$

where $f(\bar{v}_s)$ is the dynamical contribution of solitons to the Hawking temperature expressed as

$$f(\bar{v}_s) = \frac{\alpha'(1 - \bar{v}_s^4)}{\bar{v}_s^3} \sqrt{\frac{(2 \tanh \tilde{\Delta} - w)(2 - w \tanh \tilde{\Delta})}{\tanh \tilde{\Delta}}} \quad (\text{A.8})$$

and is depicted in Fig. A.2. The Hawking temperature reaches sufficiently observable tens milli-Kelvin order in existing technologies.

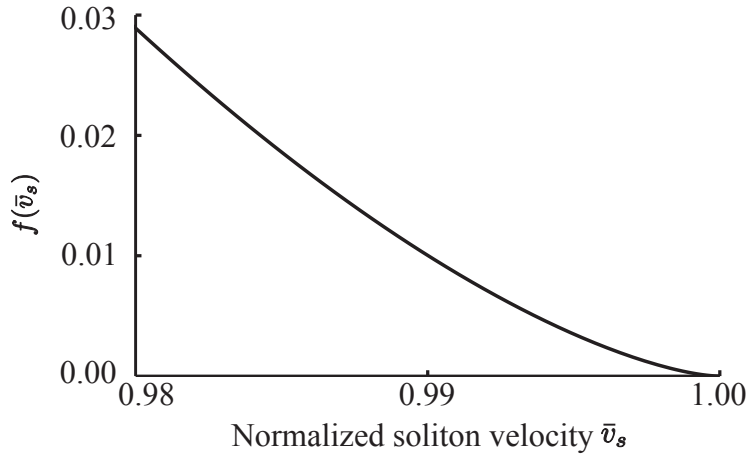


Figure A.2: The dynamical contribution for the Hawking temperature $f(\bar{v}_s)$.

A.3 Summary

We have proposed the analogue black holes designed by current soliton pairs. This scheme allows us to control the configuration of analogue black holes on demand. In other words, the black hole region can be set as desired. The result provides a new platform for exploring Hawking radiation if the quantum fluctuation of the classical soliton is taken into account. This is particularly useful for the design of the black hole laser devised in Chapter 5. Hawking radiation produced near event horizons is amplified by a stimulated emission of radiation between the event horizons, which can be considered as a resonator for electromagnetic fields. The proposed scheme allows the event horizon to be freely designed so that the resonator can be controlled to satisfy the phase-matching conditions required for laser operation. This contributes to the observation of Hawking radiation that cannot be observed due to the background radiation of the universe.

Appendix B

Solitonic black holes induced by magnetic solitons in a dc-SQUID array transmission line coupled with a magnetic chain

We have proposed analogue black holes in two types of nonlinear transmission lines, namely Josephson transmission lines and nonlinear LC transmission lines with nonlinear capacitors, in the main text. These black holes behave as solitons and can exist stably in transmission lines. The unique properties of solitons have also been very useful in the identification of Hawking radiation. However, soliton formation requires nonlinearity in the system.

In this appendix, we propose a scheme to introduce a black hole soliton into a linear system where no soliton exists. Specifically, we propose to create an analogue black hole by controlling an external magnetic field using magnetic solitons. Solitons in magnetic chains with easy-axis anisotropy are formed by the competition between the exchange energy J and the anisotropy energy D , leading to moving domain walls connecting between two different but energetically degenerate ground states [68, 69]. In a ferromagnet, a π -soliton mediates between the ground states of the upward and downward magnetic moments for example. In our proposed system, magnetic solitons play a role in generating the magnetic field applied to the dc SQUID array. Thus, single-domain magnetic nanoparticles are aligned just below the dc SQUID transmission line indicated in Fig. B.1.

We begin with a description of the magnetic soliton in a single-domain magnetic nanoparticle chain that provides the external magnetic field applied to the SQUID array, which is the key issue in this appendix. In particular, the alternating upward and downward magnetic moments in the chain in Fig. B.1 (b) are effectively treated as the magnetic moments pointing in the same direction. We consider two types of solitons that produce black holes and black hole-white hole pairs. We then describe black holes using solitons and discuss the observability of Hawking radiation in our analogue black holes by assessing the Hawking temperature. The soliton characteristics appearing in the Hawking temperature formula play a critical role in the identification of Hawking radiation.

B.1 Magnetic solitons

We propose the dc-SQUID (superconducting quantum interference device) array transmission line coupled with a magnetic chain as our third proposal for analogue black holes. The Josephson inductance is controlled by the external magnetic fields. In this section, we describe the magnetic soliton in a single-domain magnetic nanoparticle chain that provides the external magnetic field applied to the SQUID array.

B.1.1 Model

Let us consider a coplanar dc-SQUID array consisting of identical capacitance C and critical current I_c in all Josephson junctions together with a single-domain magnetic nanoparticle chain as shown in Fig. B.1. As shown in Fig. B.1 (b), the chain composed of alternating nano-sized single-domain magnets with different magnetic moments spacing $a/2$ is arranged in parallel at a distance l just below the dc-SQUID array. Suppose that all of the single-domain nanoparticles have the same size. The magnetic moments in the single-domain nanoparticle chain are inevitably forced to align alternately due to the dipole-dipole interaction. Therefore, we have no choice but to use a soliton-bearing nanoparticle model with antiferromagnetic interaction [70] as a starting point. However, the single-domain nanoparticle chain with antiferromagnetic interaction results in generating a non-magnetic field. In order to generate the suitable external magnetic field applying to the dc-SQUID array, we adopt the arrangement of single-domain nanoparticles of two sizes that alternate, in which magnetic moments alternate upward and downward similar to ferrimagnet as shown in Fig. B.1 (b). Hereafter we call this chain a ferrimagnetic-aligned nanoparticle chain. In the following, we will show that a nanomagnetic material with a small magnetic moment is substantially renormalized into a nanomagnetic material with a large magnetic moment in the ferrimagnetic-aligned nanoparticle chain, and can be effectively regarded as an alignment of same-sized nanoparticles similar to ferromagnets i.e. a ferromagnetic-aligned nanoparticle chain. The system we consider is thus a system that introduces a magnetic field generated by a well-controllable soliton into the framework of Nation's black hole system.

B.1.2 Ferrimagnetic-aligned nanoparticle chains

The model Hamiltonian for the ferrimagnetic-aligned nanoparticle chain with different sublattice anisotropies placed just below the dc SQUID array is represented by

$$\begin{aligned} \hat{H} = & J \sum_n \left(\hat{S}_{2n-1} \cdot \hat{\sigma}_{2n} + \hat{\sigma}_{2n} \cdot \hat{S}_{2n+1} \right) + \sum_n \left\{ K_\sigma^z (\hat{\sigma}_{2n}^z)^2 - K_\sigma^x (\hat{\sigma}_{2n}^x)^2 \right\} \\ & + \sum_n \left[K_S^z \left(\hat{S}_{2n-1}^z \right)^2 - K_S^x \left(\hat{S}_{2n-1}^x \right)^2 - \frac{K_S^{xy}}{4} \left\{ \left(\hat{S}_{2n-1}^x \right)^2 - \left(\hat{S}_{2n-1}^y \right)^2 \right\}^2 \right], \quad (\text{B.1}) \end{aligned}$$

where the operators \hat{S}_n and $\hat{\sigma}_n$ refer to the large and small magnetic moments of the single-domain magnets at the n th site of each sublattice, respectively. The first parenthesis of the right-hand side of Eq. (B.1) represents the dipole-dipole interaction energy with antiferromagnetic coupling ($J > 0$) between them. The second one represents magnetic anisotropy energy for small magnetic moments with $K_\sigma^{x(z)} (> 0)$ being the magnetic anisotropy parameter of the $x(z)$ component. Similarly, the last one expresses magnetic anisotropy energy for large magnetic moments, including two types

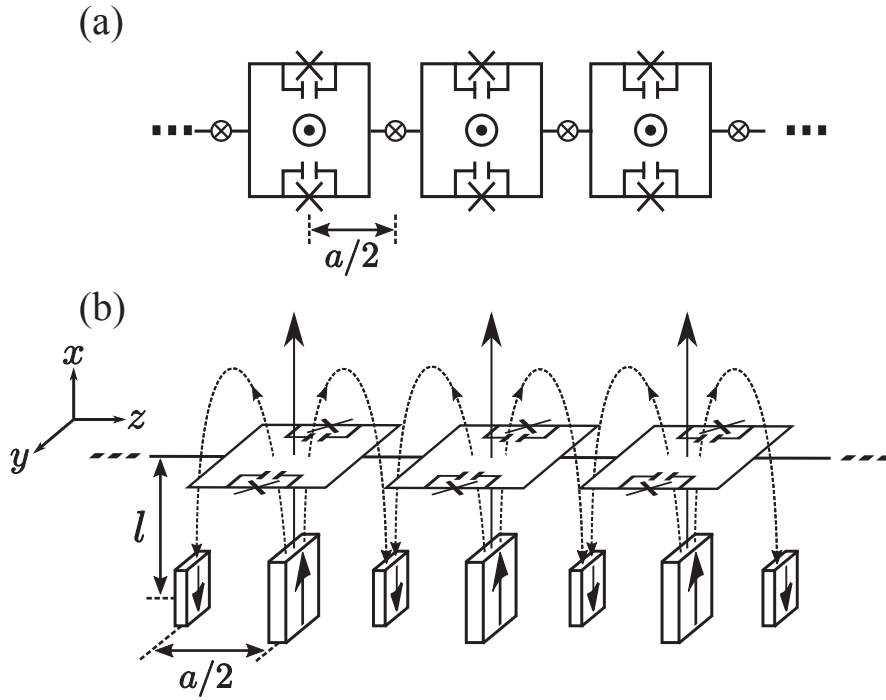


Figure B.1: (a) Diagram of a dc-SQUID array transmission line with identical capacitance C and critical current I_c in all Josephson junctions (top view). A circled dot and a cross inside the circle represent the magnetic flux applied from back to front and opposite direction, respectively when viewed from a vertical direction on a page. (b) Schematic diagram of our system. Nanosized single-domain magnets with magnetic moments different in size arranged below the dc SQUID transmission line. The magnetic flux line exits from the large upward magnetic moment and enters the small downward magnetic moment.

of anisotropy. One is uniaxial anisotropy with $K_S^{x(z)} (> 0)$ being the anisotropy parameter of the $x(z)$ component, similar to small magnetic moments. The other is biaxial anisotropy [71] with anisotropy constant $K_S^{xy} (> 0)$ coming from fourfold symmetric, which is not available in small magnetic moments. Let us assume here the relations $K_S^z \gg K_S^x, K_S^{xy}$ and $K_\sigma^z \gg K_\sigma^x$. This implies that the single-domain magnetic nanoparticle at each site has a xy easy plane. In this paper, the magnetic moment operators can be treated as classical vectors due to large magnitudes of magnetic moments in the single-domain nanoparticles; $\hat{S}_n \rightarrow \mathbf{S}_n = (S_n^x, S_n^y, S_n^z)$, $\hat{\sigma}_n \rightarrow \boldsymbol{\sigma}_n = (\sigma_n^x, \sigma_n^y, \sigma_n^z)$.

B.1.3 Effective ferromagnetic-aligned nanoparticle chains

Here we derive the effective ferromagnetic Hamiltonian from our original ferrimagnetic Hamiltonian for a single-domain ferrimagnetic-aligned nanoparticle chain by eliminating the variables $\boldsymbol{\sigma}$ for small magnetic moments [72]. This can be achieved by tracing out the relevant variables in the partition function. For the sake of simplicity, let us focus on the specific Hamiltonian $H^{(2n)}$, which is related only to $\mathbf{S}_{2n\pm 1}$ and $\boldsymbol{\sigma}_{2n}$. By integrating the classical partition function over $\boldsymbol{\sigma}_{2n}$, the effective Hamiltonian $H'^{(2n)}$ depending only on \mathbf{S}_{2n} is obtained as follows: The partition function is given as

$$Z = \int d\boldsymbol{\sigma}_{2n} \exp(-\beta H^{(2n)}) = \exp[-\beta H'^{(2n)}], \quad (\text{B.2})$$

with inverse temperature β and the Hamiltonian $H^{(2n)}$ written as

$$H^{(2n)} = H_S^{(2n)} + H_\sigma^{(2n)} + H_{S\sigma}^{(2n)}, \quad (\text{B.3})$$

where the first and second terms are Hamiltonians for large magnetic moments and small magnetic moments, respectively, and the last term is their interaction Hamiltonian. In carrying out the integration over $\boldsymbol{\sigma}_{2n}$, it is convenient to introduce a mean field for the magnetic moment, i.e.,

$$H_\sigma^{(2n)} + H_{S\sigma}^{(2n)} = -\boldsymbol{\sigma}_{2n} \cdot \mathbf{B}_{2n} - K_\sigma^z \langle \sigma_{2n}^z \rangle^2 + K_\sigma^x \langle \sigma_{2n}^x \rangle^2, \quad (\text{B.4})$$

with

$$\mathbf{B}_{2n} = -J(\mathbf{S}_{2n-1} + \mathbf{S}_{2n+1}) - 2K_\sigma^z \langle \sigma_{2n}^z \rangle \mathbf{e}_z + 2K_\sigma^x \langle \sigma_{2n}^x \rangle \mathbf{e}_x, \quad (\text{B.5})$$

under the mean field approximation $(\sigma_{2n}^{x(z)} - \langle \sigma_{2n}^{x(z)} \rangle)^2 \simeq 0$, where $\mathbf{e}_{x(z)}$ represents the unit vector pointing in $x(z)$ direction. Based on the calculations shown in Appendix, we obtain the effective Hamiltonian H'

$$H' = -J' \sum_{\langle i,j \rangle} \mathbf{S}_i \cdot \mathbf{S}_j + \sum_i \left[K'_z (S_i^z)^2 - K'_x (S_i^x)^2 - \frac{K_S^{xy}}{4} \left\{ (S_i^x)^2 - (S_i^y)^2 \right\}^2 \right], \quad (\text{B.6})$$

where $\langle i,j \rangle$ represents the sum over the nearest neighbors only. The exchange ($J' > 0$) and anisotropy (K'_x and K'_z) coefficients together with the conditions $J' > 0$, $K'_z \gg K'_x$, and $K_S^{xy} > 0$ are given by

$$J' = \frac{J\sigma}{2S}, \quad (\text{B.7})$$

$$K'_x = K_S^x - \frac{\sigma^2}{S^2} K_\sigma^x, \quad (\text{B.8})$$

$$K'_z = K_S^z + \frac{\sigma^2}{S^2} K_\sigma^z. \quad (\text{B.9})$$

This means that the ferrimagnetic-aligned nanoparticle chain indicated in Fig. B.2 (a) can be effectively considered as single-domain magnets with the same size magnetic moments aligned with a fixed space a , leading to the ferromagnetic-aligned nanoparticle chain as shown in Fig. B.2 (b). The magnetic moment vector \mathbf{S} rotates in xy plane due to the condition $K'_z \gg K'_x, K_S^{xy}$.

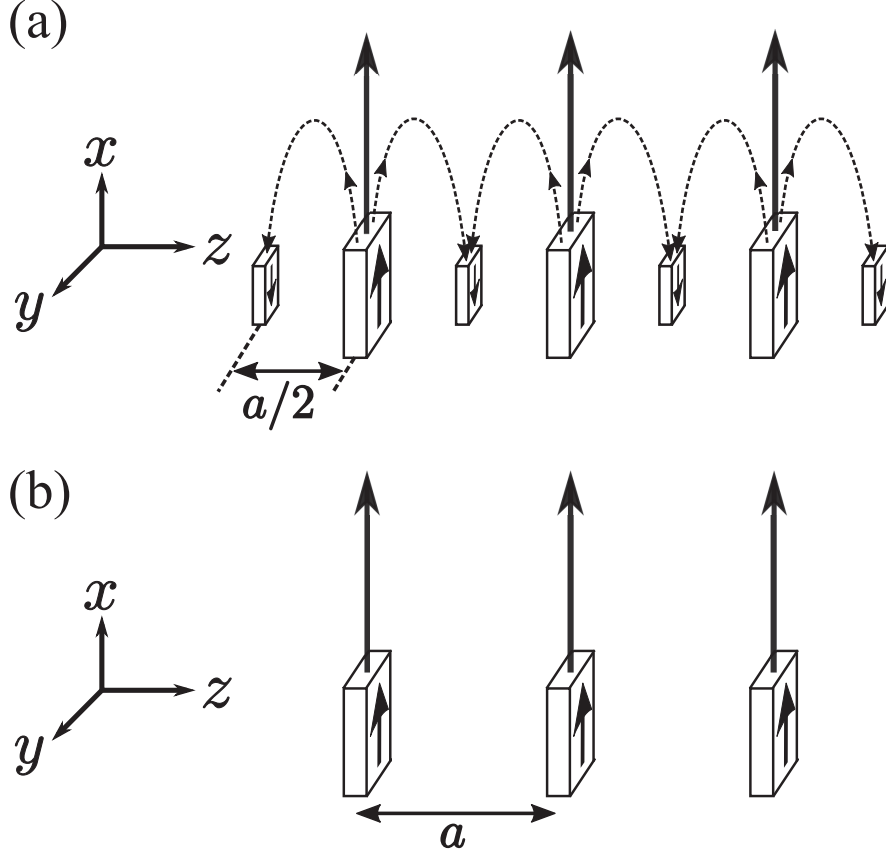


Figure B.2: (a) Ferrimagnetic-aligned nanoparticle chain. The nanoparticles of different sizes are aligned with fixed space $a/2$. The magnetic moments alternatively direct upward and downward for the energetical stability similar to the ferrimagnets. (b) The effective ferromagnetic-aligned nanoparticle chain, where the same size magnetic moments are aligned with fixed space a .

B.1.4 Magnetic solitons as a magnetic-field source

Now let us consider the dynamics of magnetic moments in the effective ferromagnetic chain obtained above and derive two types of soliton solutions as a magnetic-field source. The effective magnetic field \mathbf{B}_i generated by the magnetic moment \mathbf{S}_i in the nanoparticles is given as

$$\mathbf{B}_i = -\frac{dH'}{d\mathbf{S}_i}. \quad (\text{B.10})$$

This causes Larmor precession in magnetic moments [68]. The equation of the motion is

$$\frac{d\mathbf{S}_i}{dt} = \mathbf{S}_i \times \mathbf{B}_i. \quad (\text{B.11})$$

Under the continuum approximation, magnetic moments are expressed in spherical coordinates as follows

$$\begin{aligned}\mathbf{S}_i &= \mathbf{S}(z) \\ &= S \left(\cos \delta \cos \phi(z) \quad \cos \delta \sin \phi(z) \quad \sin \delta \right),\end{aligned}\tag{B.12}$$

where ϕ is the azimuthal angle and $\delta(= \pi/2 - \theta)$ is the perturbation angle with θ being the polar angle. The perturbation angle δ is assumed to be sufficiently small, so that $\sin \delta \simeq \delta$ and $\cos \delta \simeq 1$ hold. We also use the approximation $(\partial\phi/\partial z)^2 \simeq 0$. From Eq. (B.11), we obtain

$$\frac{\partial\delta}{\partial t} = J'Sa^2 \frac{\partial^2\phi}{\partial z^2} - K'_x S \sin 2\phi - \frac{1}{2}K_S^{xy} S^3 \sin 4\phi,\tag{B.13}$$

$$\begin{aligned}\frac{\partial\phi}{\partial t} &= 2K'_z S\delta + 2K'_x S\delta \cos^2 \phi + K_S^{xy} S^3 \delta \cos^2 2\phi \\ &\simeq 2K'_z S\delta,\end{aligned}\tag{B.14}$$

leading to double sine-Gordon equation

$$\frac{\partial^2\phi}{\partial t^2} - v_0^2 \frac{\partial^2\phi}{\partial z^2} + m_1^2 \sin 2\phi + m_2^2 \sin 4\phi = 0,\tag{B.15}$$

where $v_0^2 = 2K'_z J' S^2 a^2$, $m_1^2 = 2K'_x K'_z S^2$, and $m_2^2 = K_S^{xy} K'_z S^4$. v_0 stands for the velocity of the linear wave. The double sine-Gordon equation has been investigated in detail and is known to have various types of soliton solutions depending on the parameters [73]. Here let us focus on two types of solitons that are useful for the generation of black hole solitons to be discussed below.

B.1.5 90-degree magnetic solitons

The first type of soliton is 90-degree (\perp) magnetic soliton as shown in Fig. B.3 (a), which reproduces a *single* black hole equivalent to the black hole proposed by Nation et al. [21] except for the characteristics of the soliton. This soliton solution is obtained in the double sine-Gordon equation Eq. (B.15) when $m_1 = 0$, that is, the uniaxial coefficient K'_x is 0. The 90-degree magnetic soliton solution is expressed as

$$\phi^\perp(z, t) = \arctan \left\{ e^{\pm \frac{\gamma}{d_0^\perp} (z - v_s t)} \right\},\tag{B.16}$$

with the soliton velocity v_s , $d_0^\perp = a\sqrt{J'/4K_S^{xy}S^2}$, and Lorentz factor $\gamma = 1/\sqrt{1 - (v_s/v_0)^2}$. Figure B.3 (a) shows the 90-degree magnetic soliton expressed by the soliton solution Eq. (B.16) with the width $d \sim 2d_0^\perp/\gamma$. The continuum approximation is applicable when the soliton width is larger than the unit length $d/a \sim \sqrt{J'/4K_S^{xy}S^2}/\gamma > 1$. This condition can be satisfied by properly designing the system parameters and soliton velocity. This type of soliton results from biaxial magnetic anisotropy with the anisotropy energy $-K_S^{xy} \left\{ (S_i^x)^2 - (S_i^z)^2 \right\} / 4$ where the magnetization along $+x$ and $+y$ are degenerate. Therefore, the magnetic moments in a single-domain magnets chain are forced to rotate 90 degrees for a transition between two equilibrium states.

B.1.6 180-degree magnetic solitons

On the other hand, the 180-degree (\parallel) magnetic solitons are formed when $m_2 = 0$, equivalently, the biaxial magnetic anisotropy constant $K_S^{xy} = 0$. The soliton solution of Eq. (B.15) is similarly expressed as

$$\phi^{\parallel}(z, t) = 2 \arctan \left\{ e^{\pm \frac{\gamma}{d_0^{\parallel}}(z - v_s t)} \right\}, \quad (\text{B.17})$$

with $d_0^{\parallel} = a\sqrt{J'/2K'_x}$. Figure B.3 (b) shows the 180-degree magnetic soliton formed by the soliton solution Eq. (B.17) with the width $d \sim 2d_0^{\parallel}/\gamma$. In this case, the magnetization along $+x$ and $-x$ are degenerate due to the uniaxial magnetic anisotropy energy $-K'_x(S_i^x)^2$. The magnetic moments in a single-domain magnets chain are forced to rotate 180 degrees for a transition between two equilibrium states. This is the origin of the 180-degree magnetic soliton generation. Unlike 90-degree magnetic solitons, the 180-degree magnetic solitons form black hole *pairs* as described below.

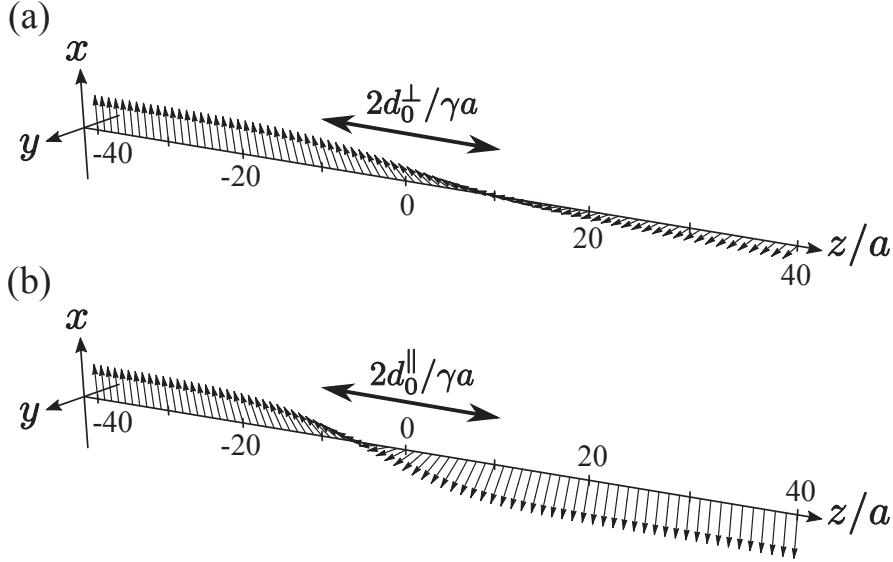


Figure B.3: Sketch of the soliton with the width $d \sim 2d_0^{\perp(\parallel)}/\gamma$ in the effective ferromagnetic-aligned nanoparticle chain, where nanoparticles are arranged at uniform distance a . z/a denotes the number of dc SQUIDS. (a) 90-degree magnetic soliton and (b) 180-degree magnetic soliton.

B.2 Magnetic soliton induced analogue black hole

Here let us discuss black hole solitons generated using magnetic solitons. In the Josephson circuit, the kinetic inductance $L(\Phi)$ of the junction depends on the flux Φ through dc SQUID as follows,

$$L(\Phi) = \frac{L_0}{\cos(2\pi\Phi/\Phi_0)}, \quad (\text{B.18})$$

with magnetic flux quantum $\Phi_0 = h/2e$ and the Josephson inductance $L_0 = \hbar/2eI_c$. As is well known, the propagation velocity of electromagnetic wave c in this circuit is given by $c = a/\sqrt{LC}$.

Thus, the propagation velocity depending on the magnetic flux through dc SQUID is expressed as

$$\bar{c}(\Phi) = \sqrt{\cos(2\pi\Phi/\Phi_0)}, \quad (\text{B.19})$$

where c is normalized by $c_0 = a/\sqrt{L_0 C}$. In our model, the magnetic field perpendicular to the SQUID is generated by the magnetic moments of the single-domain magnets chain. The magnetic flux threading through the dc SQUID with its area A is

$$\Phi = B_x A = \frac{SA}{2\pi l^3} \cos \phi = \frac{\Phi_1}{2\pi} \cos \phi \quad (\text{B.20})$$

with $\Phi_1 = SA/l^3$. By substituting soliton solutions for the azimuthal angle ϕ of the magnetic moments, the magnetic flux is then obtained. The magnetic flux induced by the magnetic solitons modulates the velocity of an electromagnetic wave spatially as

$$\bar{c}(z, t) = \sqrt{\cos \{ \bar{\Phi} \cos \phi(z, t) \}} \quad (\text{B.21})$$

where $\bar{\Phi} = \Phi_1/\Phi_0$, leading to the analogue black holes.

There are three conditions for creating analogue black holes in our system. First, the velocity of an electromagnetic wave in the circuit expressed in Eq. (B.21) must be real. This leads to the condition $0 \leq \bar{\Phi} \leq \pi/2$. Second, the soliton velocity is faster than the lower limit of the velocity of an electromagnetic wave in the circuit, i.e., $\lim_{x \rightarrow \pm\infty} \bar{c}(x, t) = \sqrt{\cos \bar{\Phi}} < \bar{v}_s$. The third is the natural condition that the velocity of an electromagnetic wave in the circuit under the magnetic field is slower than the velocity of an electromagnetic wave with no magnetic field. As a result, the soliton velocity is restricted in the range $\sqrt{\cos \bar{\Phi}} < \bar{v}_s < 1$.

B.2.1 Black hole solitons induced by the 90-degree magnetic solitons

Here, let us consider the black hole solitons induced by 90-degree magnetic soliton obeying Eq. (B.16). The magnetic flux through the dc SQUID is written as

$$\begin{aligned} \Phi^\perp(z, t) &= \frac{\Phi_1}{2\pi} \cos \left[\arctan \left\{ e^{\pm \frac{\gamma}{d_0^\perp} (z - v_s t)} \right\} \right] \\ &= \frac{\Phi_1}{2\pi} \sqrt{\frac{1}{2} \{ 1 \mp \tanh(\gamma(z - v_s t)/d_0^\perp) \}}, \end{aligned} \quad (\text{B.22})$$

by using Eq. (B.20). The magnetic flux through the dc SQUID in the transmission line changes spatially between 0 and $\Phi_1/2\pi$ as shown in Fig. B.4 (b) since the magnetic moments rotate 90 degrees as shown in Fig. B.4 (a). From Eq. (B.18), one has the spatially varying Josephson inductance $L(\Phi)$ as follows,

$$L^\perp(\Phi) = \frac{L_0}{\cos \left[\bar{\Phi} \sqrt{\frac{1}{2} \{ 1 \mp \tanh(\gamma(z - v_s t)/d_0^\perp) \}} \right]}. \quad (\text{B.23})$$

As a result, the effective velocity of an electromagnetic wave in the dc-SQUID array transmission line is obtained from Eq. (B.19) as

$$\bar{c}^\perp(z, t) = \sqrt{\cos \left[\frac{\bar{\Phi}}{\sqrt{2}} \{ 1 \mp \tanh(\gamma(z - v_s t)/d_0^\perp) \}^{1/2} \right]}. \quad (\text{B.24})$$

Figure B.4 (c) shows the normalized space-dependent velocity of an electromagnetic wave in the comoving frame at $\bar{v}_s = 0.98$ as an example. The event horizon occurs at $(\bar{c}(\xi_h^\perp))^2 = \bar{v}_s^2$. The position of the event horizon in the comoving frame is given by

$$\xi_h^\perp = \pm \frac{d_0^\perp}{\gamma} \operatorname{arctanh} \left(\frac{2}{\bar{\Phi}^2} \arccos^2 \bar{v}_s^2 - 1 \right) \quad (\text{B.25})$$

and is shown in Fig. B.6 (b). An analogue black hole can be formed where the velocity of the electromagnetic wave is slower than the soliton velocity.

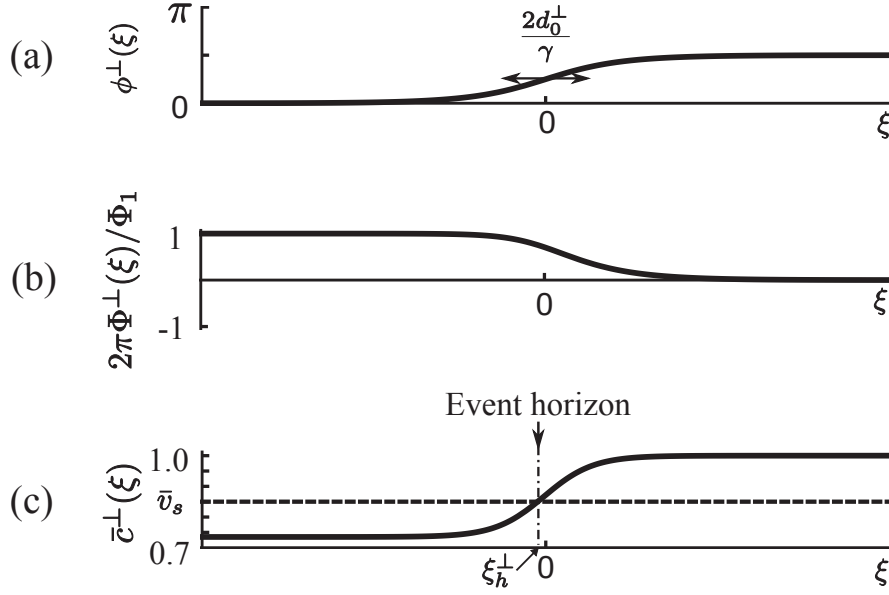


Figure B.4: (a) The rotation angle of the magnetic moments in xy plane at ξ in the comoving frame. (b) The spatially varying magnetic flux applying to the dc-SQUID array in the comoving frame. (c) The normalized velocity of the electromagnetic wave with $\bar{\Phi} = 1$. The horizontal dotted line represents the normalized soliton velocity \bar{v}_s . ξ_h^\perp indicates the position of the event horizon.

B.2.2 Black hole solitons induced by the 180-degree magnetic solitons

Here, let us consider the black hole solitons created by 180-degree magnetic soliton obtained in Eq. (B.17). The magnetic flux through the dc SQUID is written as

$$\begin{aligned} \Phi^\parallel(z, t) &= \frac{\Phi_1}{2\pi} \cos \left[2 \arctan \left\{ e^{\pm \frac{\gamma}{d_0^\parallel} (z - v_s t)} \right\} \right] \\ &= \frac{\Phi_1}{2\pi} \tanh \left\{ \mp \gamma (z - v_s t) / d_0^\parallel \right\}, \end{aligned} \quad (\text{B.26})$$

by using Eq. (B.20). The magnetic flux through the dc SQUID in the transmission line changes spatially between $-\Phi_1/2\pi$ and $\Phi_1/2\pi$ as shown in Fig. B.5 (b) since the magnetic moments rotate

180 degrees shown in Fig. B.5 (a). From Eq. (B.18), the Josephson inductance is given as

$$L^{\parallel}(\Phi) = \frac{L_0}{\cos \left[\bar{\Phi} \tanh \left\{ \mp \gamma (z - v_s t) / d_0^{\parallel} \right\} \right]}. \quad (\text{B.27})$$

The effective velocity of an electromagnetic wave in the transmission line is then obtained from Eq. (B.19) as

$$\bar{c}^{\parallel}(z, t) = \sqrt{\cos \left[\bar{\Phi} \tanh \left\{ \mp \gamma (z - v_s t) / d_0^{\parallel} \right\} \right]}. \quad (\text{B.28})$$

Figure B.5 (c) shows the normalized space-dependent velocity of the electromagnetic wave in the comoving frame at $\bar{v}_s = 0.98$ similar to the example at the 90-degree soliton. The event horizon occurs at $(\bar{c}(\xi_h^{\parallel}))^2 = \bar{v}_s^2$. The position of the event horizon in the comoving frame is given by

$$\xi_h^{\parallel \pm} = \pm \frac{d_0^{\parallel}}{\gamma} \operatorname{arctanh} \left(\frac{1}{\bar{\Phi}} \arccos \bar{v}_s^2 \right), \quad (\text{B.29})$$

(see Fig. B.7 (b)). Unlike the analogue black hole induced by 90-degree magnetic solitons, *the pair of analogue black holes* can be created where the velocity of the electromagnetic wave is slower than the soliton velocity.

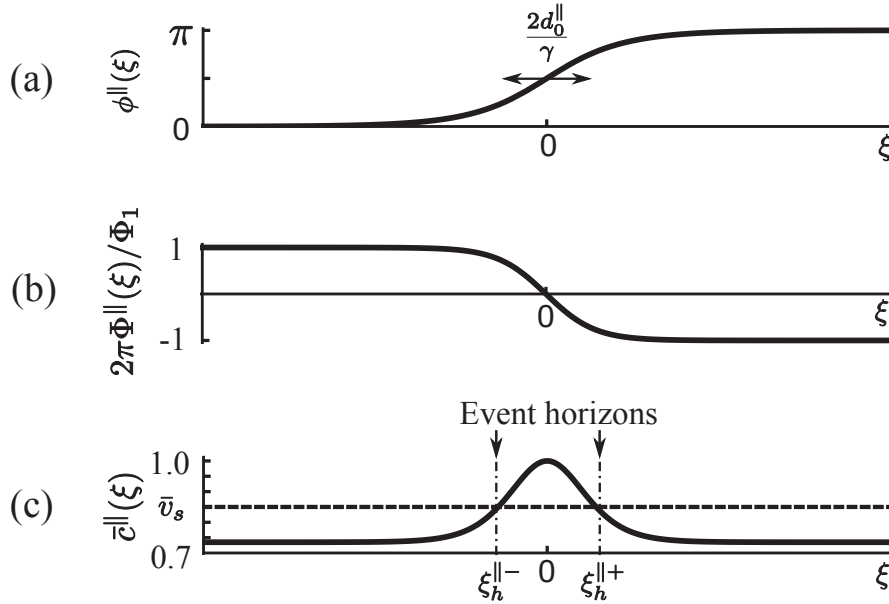


Figure B.5: (a) The rotation angle of the magnetic moments in xy plane at ξ in the comoving frame. (b) The spatially varying magnetic flux applying to the dc SQUID array in the comoving frame. (c) The normalized velocity of the electromagnetic wave with $\bar{\Phi} = 1$. The horizontal dotted line represents the normalized soliton velocity \bar{v}_s . $\xi_h^{\parallel -}$ and $\xi_h^{\parallel +}$ indicate the black hole and white hole horizon positions, respectively.

B.2.3 Magnetic soliton induced analogue black hole

Black hole solitons induced by the 90-degree magnetic solitons

Now, we derive the Hawking temperature in the obtained analogue black hole. Substituting Eq. (B.24) into Eq. (A.6), we obtain the formula,

$$T_H^\perp = (T_H^0)^\perp f^\perp(\bar{v}_s), \quad (\text{B.30})$$

where $(T_H^0)^\perp$ and $f^\perp(\bar{v}_s)$ stand for *bare* Hawking temperature and soliton characteristic function, respectively, and are given as follows:

$$(T_H^0)^\perp = \frac{\hbar}{2\pi k_B} c_0 \frac{1}{d_0^\perp}, \quad (\text{B.31})$$

$$f^\perp(\bar{v}_s) = \frac{1}{2} \left(\arccos \bar{v}_s^2 \right) \sqrt{1 + \frac{1}{\bar{v}_s^2}} \left| 1 - \left(\frac{\arccos \bar{v}_s^2}{\bar{\Phi}} \right)^2 \right|. \quad (\text{B.32})$$

The *bare* Hawking temperature $(T_H^0)^\perp$ given solely by the system parameters determines the rough temperature scale. Thus one can control $(T_H^0)^\perp$ by designing the system parameters. For example, assuming $d \sim 2d_0^\perp/\gamma > a$ to satisfy the continuum approximation together with circuit parameters accessible with current technology, typically, $C \sim 10^{-16} F$ and $I_0 \sim 10^{-7} A$, the bare Hawking temperature T_H^0 is in the sub-Kelvin order and is fully observable.

In addition, it is found that the Hawking temperature also depends on the soliton velocity \bar{v}_s as shown in Fig. B.6 (d), which was not found in previous studies. This is essentially due to the relativistic dynamical contribution of the soliton $f^\perp(\bar{v}_s)$ through the Lorentz factor as discussed below. According to Eq. (A.6), the Hawking temperature is determined by the velocity gradient of the electromagnetic wave in the circuit at the event horizon. The two elements of the definition, the velocity gradient and the position of the event horizon, both depend on the soliton velocity.

First, let us discuss the velocity gradient of the electromagnetic wave in the circuit, which is introduced by the magnetic soliton. The velocity gradient then depends on the soliton shape that is characterized by the soliton width $d \sim 2d_0^\perp/\gamma$. A short soliton width means a steep velocity gradient. The width contains the Lorentz factor γ depending on the soliton velocity. Thus, the soliton width decreases as the soliton velocity increases due to the Lorentz contraction. This makes the tanh-type soliton shape steeper. In other words, the relativistic effect γ increases the slope of the soliton, resulting in the steeper velocity gradient of the electromagnetic wave.

The second factor that affects the Hawking temperature, which involves the soliton velocity, is the position of the event horizon. Figure B.6 (b) shows the position of the event horizon as a function of soliton velocity. This strange behavior is due to the peculiar soliton-velocity dependence on the Lorentz factor. As you can see in Fig. B.6 (a), when the soliton velocity increases, the position of the event horizon shifts to the right at first. This is simply because $\bar{c}^\perp(\xi_h^\perp)$, which satisfies the event horizon condition, increases. Lorentz contractions are less important for slow solitons. However, it then turns to the left from a certain point. This is due to the Lorentz contraction manifested at a soliton velocity close to the speed of light. The soliton width becomes shorter and the points that satisfy the condition shift to the left.

To summarize the above discussion, the Hawking temperature increases monotonically with increasing soliton velocity and decreases rapidly to zero at high velocities where Lorentz contraction becomes prominent. In these decreasing parts in temperature, the soliton width shortens rapidly

and the velocity gradient $|\partial\bar{c}^\perp/\partial\xi|$ approaches the delta function. Therefore, the velocity gradient at the event horizon decreases rapidly and finally becomes 0. In other words, the change of the velocity gradient approaching the delta function is more rapid than the change of the position of the event horizon as a function of the soliton velocity.

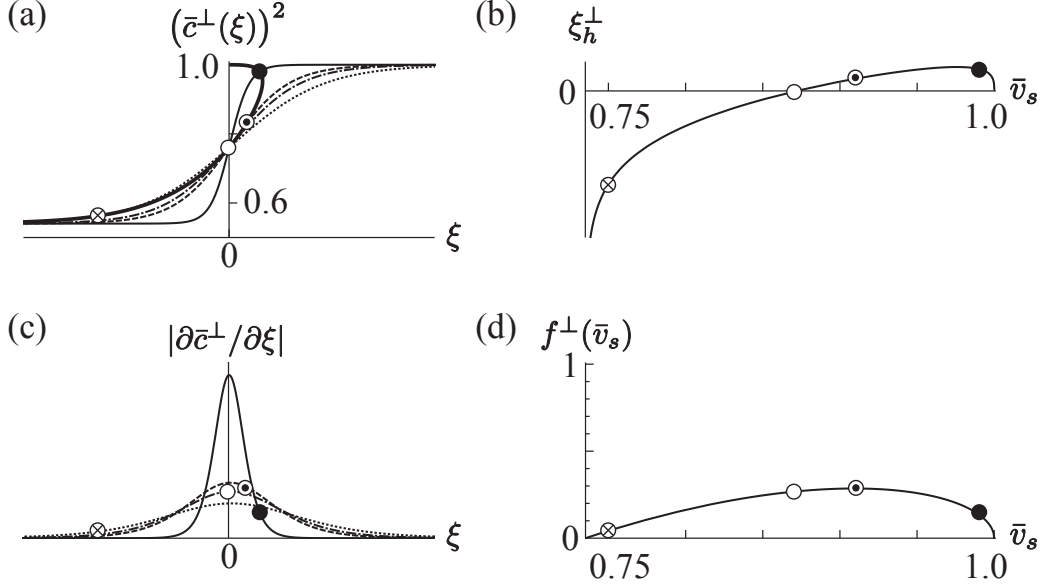


Figure B.6: (a) Spatial dependence of squared velocity of the electromagnetic wave $(\bar{c}^\perp(\xi))^2$ for some typical soliton velocities; $\bar{v}_s = 0.75$ (dotted line), 0.87 (one-dot chain line), 0.91 (dashed line), and 0.99 (solid line). The position of event horizons is depicted by the bold line with circles corresponding to the typical soliton velocities shown above, such as $\bar{v}_s = 0.75$ (cross inside a circle), 0.86 (open circle), 0.91 (circled dot), and 0.99 (filled circle). The circles in all embedded figures correspond to these values. (b) The position of the event horizon as a function of the soliton velocity. (c) The velocity gradient of the electromagnetic wave $|\partial\bar{c}^\perp/\partial\xi|$. (d) The Hawking temperatures $f^\perp(\bar{v}_s)$ given in Eq. (B.32) under the condition $\bar{\Phi} = 1$ as a function of the soliton velocity \bar{v}_s .

Black hole solitons induced by the 180-degree magnetic solitons

Here we discuss the observability of the Hawking radiation in the pair of the analogue black holes by deriving the Hawking temperature analytically using the formula Eq. (A.6). The Hawking temperature is expressed as

$$T_H^\parallel = (T_H^0)^\parallel f^\parallel(\bar{v}_s), \quad (\text{B.33})$$

where $(T_H^0)^\parallel$ and $f^\parallel(\bar{v}_s)$ represent the bare Hawking temperature and the soliton characteristic function, respectively, and are written as follows:

$$(T_H^0)^\parallel = \frac{\hbar}{2\pi k_B} c_0 \bar{\Phi} \frac{1}{d_0^\parallel}, \quad (\text{B.34})$$

$$f^\parallel(\bar{v}_s) = \frac{1}{2} \sqrt{1 + \frac{1}{\bar{v}_s^2}} \left| 1 - \left(\frac{\arccos \bar{v}_s^2}{\bar{\Phi}} \right)^2 \right|. \quad (\text{B.35})$$

The bare Hawking temperature $(T_H^0)^\parallel$ determines the rough temperature scale. One can control $(T_H^0)^\parallel$ by designing the system parameters since it depends solely on the system parameters. For example, assuming $d \sim 2d_0^\parallel/\gamma > a$ at $\bar{\Phi} = 1$ together with circuit parameters accessible with current technology, the bare Hawking temperature T_H^0 is in the sub-Kelvin order and is also observable.

Similar to the black hole soliton formed by the 90-degree magnetic solitons, the Hawking temperature is also found to be dependent on the soliton velocity \bar{v}_s as shown in Fig. B.7 (d), which has not been found in the previous studies. This is due to the same relativistic mechanism as the black hole soliton induced by 90-degree magnetic solitons. Here, only the differences are described. The velocity of the electromagnetic wave in the circuit is symmetric with respect to the origin. This is the origin of two degenerate event horizons. Therefore, the soliton-velocity dependence is the same for two event horizons. In fact, the soliton-velocity dependence on the Hawking temperature is exactly the same for black holes and white holes as shown in Fig. B.7 (d).

To summarize our black hole solitons, their Hawking temperatures reflect the dynamic properties of soliton and show unprecedented properties that depend on the soliton velocity. This dependence implies that the Hawking temperature can be controlled simply by changing the soliton velocity without changing the circuit configuration at all. Therefore, this change confirms that the experimentally detected radiation is actually due to Hawking radiation. This is an excellent advantage that has never been seen before.

B.3 Summary

We have investigated analogue black holes generated in an array of dc SQUIDs coupled in parallel with a one-dimensional chain of single-domain nanomagnets. Starting with a ferrimagnetic-aligned nanoparticle chain with alternating magnetic moments both in direction and magnitude, we have shown that the ferrimagnetic-aligned nanoparticle chain can be effectively reduced to a ferromagnetic-aligned nanoparticle chain. Then, we derived two types of solitons that appear there. The magnetic solitons in the chain produce magnetic fields perpendicular to the SQUID array, leading to the spatially varying velocities of electromagnetic waves through the nonlinear inductance in the array. The effective event horizon is established where the soliton velocity is equal to the spatially varying velocity of the electromagnetic wave in the circuit. Therefore, an analogue black hole is created in the region of the circuit with an effective velocity of the electromagnetic wave lower than the soliton velocity. It was found that 90-degree magnetic solitons produce single analogue black holes as described in previous studies, whereas 180-degree magnetic solitons produce analogue black hole pairs.

We have also derived the Hawking temperature in these analogue black holes based on the tunneling mechanism for Hawking radiation. In our system, the electromagnetic wave produced by the quantum fluctuation of the Josephson phase near the classical soliton is observed as the Hawking radiation. According to the formula, Hawking radiation is observable in the circuit using existing technologies. In addition, the Hawking temperature reflects the characteristics of solitons because the black holes are derived from solitons. That is, it depends on the soliton velocity. If this dependence can be confirmed experimentally, it can be identified that the observed radiation is certainly from an analogue black hole. This might reinforce the previously known identification method based on the entanglement of radiated light [15].

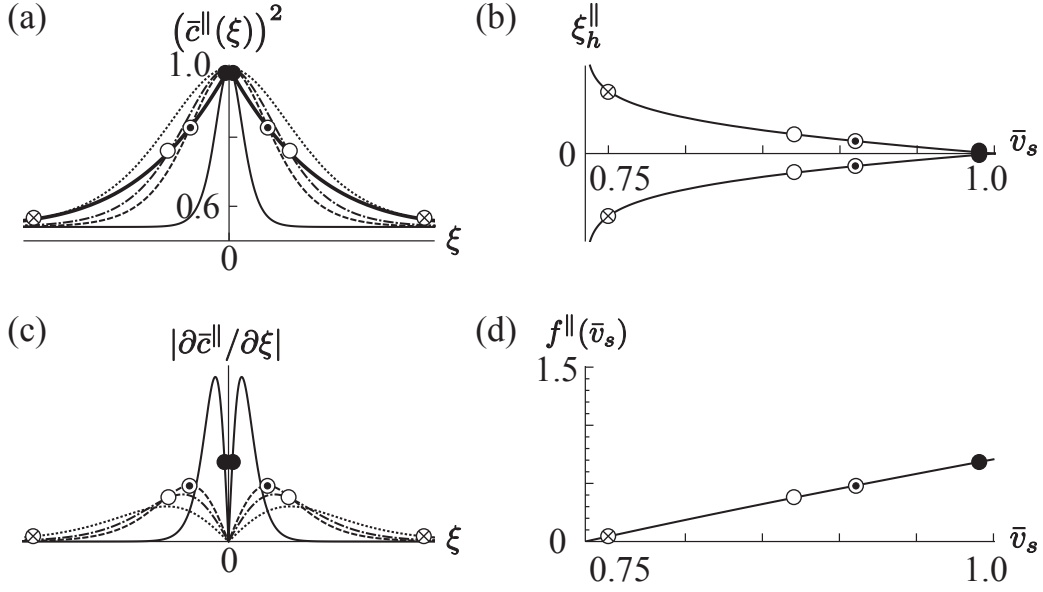


Figure B.7: (a) Spatial dependence of squared velocity of the electromagnetic wave $(\bar{c}^{\parallel}(\xi))^2$ for some typical soliton velocities; $\bar{v}_s = 0.75$ (dotted line), 0.87 (one-dot chain line), 0.91 (dashed line), and 0.99 (solid line). The pair of event horizons are formed for each soliton velocities, unlike 90-degree magnetic solitons. The position of event horizons is depicted by the bold line with circles corresponding to the typical soliton velocities shown above, such as $\bar{v}_s = 0.75$ (cross inside a circle), 0.86 (open circle), 0.91 (circled dot), and 0.99 (filled circle). The circles in all embedded figures correspond to these values. (b) The position of the event horizon as a function of the soliton velocity. (c) The velocity gradient of the electromagnetic wave $|\partial\bar{c}^{\parallel}/\partial\xi|$. It is symmetric about the vertical axis so that the Hawking temperatures are the same at both positions of the event horizons. (d) The Hawking temperatures $f^{\parallel}(\bar{v}_s)$ given in Eq. (B.35) under the condition $\bar{\Phi} = 1$ as a function of the soliton velocity \bar{v}_s .

B.4 Supplementary

Here we derive the effective ferromagnetic Hamiltonian starting from our original ferrimagnetic Hamiltonian for a single-domain ferrimagnetic chain given in Eq. (B.1), which is rewritten as

$$H = \sum_n (H_{S\sigma}^{(2n)} + H_S^{(2n)} + H_\sigma^{(2n)}), \quad (\text{B.36})$$

where

$$H_{S\sigma}^{(2n)} = J (\mathbf{S}_{2n-1} \cdot \boldsymbol{\sigma}_{2n} + \boldsymbol{\sigma}_{2n} \cdot \mathbf{S}_{2n+1}), \quad (\text{B.37})$$

$$H_S^{(2n)} = K_S^z (S_{2n-1}^z)^2 - K_S^x (S_{2n-1}^x)^2 - \frac{K_S^{xy}}{4} \left\{ (S_{2n-1}^x)^2 - (S_{2n-1}^y)^2 \right\}^2, \quad (\text{B.38})$$

$$H_\sigma^{(2n)} = K_\sigma^z (\sigma_{2n}^z)^2 - K_\sigma^x (\sigma_{2n}^x)^2. \quad (\text{B.39})$$

In order to remove the variables $\boldsymbol{\sigma}_{2n}$ from this Hamiltonian, let us consider the integration over $\boldsymbol{\sigma}_{2n}$ of the partition function as follows,

$$Z^{(2n)} = Z_S^{(2n)} \cdot Z_{\sigma,S\sigma}^{(2n)}, \quad (\text{B.40})$$

where

$$Z_S^{(2n)} = \exp(-\beta H_S^{(2n)}) \quad (\text{B.41})$$

$$Z_{\sigma,S\sigma}^{(2n)} = \int d\boldsymbol{\sigma}_{2n} \exp\{-\beta(H_\sigma^{(2n)} + H_{S\sigma}^{(2n)})\}. \quad (\text{B.42})$$

Equation (B.4) is derived by substituting Eq. (B.43) for Eq. (B.39) with $(\sigma_{2n}^{x(z)} - \langle \sigma_{2n}^{x(z)} \rangle)^2 \simeq 0$,

$$\begin{aligned} & \left(\sigma_{2n}^{x(z)} \right)^2 \\ &= \left(\sigma_{2n}^{x(z)} - \langle \sigma_{2n}^{x(z)} \rangle + \langle \sigma_{2n}^{x(z)} \rangle \right)^2 \\ &\simeq 2 \left(\sigma_{2n}^{x(z)} - \langle \sigma_{2n}^{x(z)} \rangle \right) \langle \sigma_{2n}^{x(z)} \rangle + \langle \sigma_{2n}^{x(z)} \rangle^2. \end{aligned} \quad (\text{B.43})$$

Then, we obtain

$$\begin{aligned} Z_{\sigma,S\sigma}^{(2n)} &= \int d\boldsymbol{\sigma}_{2n} \exp\{-\beta(-\boldsymbol{\sigma}_{2n} \cdot \mathbf{B}_{2n} \\ &\quad - K_\sigma^z \langle \sigma_{2n}^z \rangle^2 + K_\sigma^x \langle \sigma_{2n}^x \rangle^2)\}. \end{aligned} \quad (\text{B.44})$$

In order to carry out the integration over σ_{2n} in Eq. (B.44), we use the polar variables with the azimuthal angle ϕ and the angle Θ between σ_{2n} and \mathbf{B}_{2n} as follows,

$$Z_{\sigma, S\sigma}^{(2n)} = \int_0^{2\pi} \int_{-1}^1 \exp \left[-\beta \left(-\sigma |\mathbf{B}_{2n}| \cos \Theta - K_\sigma^z \langle \sigma_{2n}^z \rangle^2 + K_\sigma^x \langle \sigma_{2n}^x \rangle^2 \right) \right] d(\cos \Theta) d\phi \quad (\text{B.45})$$

$$= 2\pi \exp \left[-\beta \left(-K_\sigma^z \langle \sigma_{2n}^z \rangle^2 + K_\sigma^x \langle \sigma_{2n}^x \rangle^2 \right) \right] \times \int_{-1}^1 \exp [\beta \sigma |\mathbf{B}_{2n}| \cos \Theta] d(\cos \Theta) \quad (\text{B.46})$$

$$= \frac{2\pi}{\beta \sigma |\mathbf{B}_{2n}|} \exp \left[-\beta \left(-K_\sigma^z \langle \sigma_{2n}^z \rangle^2 + K_\sigma^x \langle \sigma_{2n}^x \rangle^2 \right) \right] \times (\exp [\beta \sigma |\mathbf{B}_{2n}|] - \exp [-\beta \sigma |\mathbf{B}_{2n}|]). \quad (\text{B.47})$$

In the limit $\beta \rightarrow 0$, $Z_{\sigma, S\sigma}^{(2n)}$ converges as follows,

$$Z_{\sigma, S\sigma}^{(2n)} \rightarrow \frac{2\pi}{\beta \sigma |\mathbf{B}_{2n}|} \exp \left[-\beta \left(-K_\sigma^z \langle \sigma_{2n}^z \rangle^2 + K_\sigma^x \langle \sigma_{2n}^x \rangle^2 \right) \right] \times \exp [\beta \sigma |\mathbf{B}_{2n}|] \quad (\text{B.48})$$

$$\sim \exp \left[-\beta \left(-\sigma |\mathbf{B}_{2n}| - K_\sigma^z \langle \sigma_{2n}^z \rangle^2 + K_\sigma^x \langle \sigma_{2n}^x \rangle^2 \right) \right]. \quad (\text{B.49})$$

From Eq. (B.40), we obtain

$$Z^{(2n)} \sim \exp \left[-\beta \left(H_S^{(2n)} - \sigma |\mathbf{B}_{2n}| - K_\sigma^z \langle \sigma_{2n}^z \rangle^2 + K_\sigma^x \langle \sigma_{2n}^x \rangle^2 \right) \right]. \quad (\text{B.50})$$

In comparison with the right-hand side of Eq. (B.2), the effective Hamiltonian is given as

$$H^{(2n)} \sim H_S^{(2n)} - \sigma |\mathbf{B}_{2n}| - K_\sigma^z \langle \sigma_{2n}^z \rangle^2 + K_\sigma^x \langle \sigma_{2n}^x \rangle^2. \quad (\text{B.51})$$

Now let us derive $|\mathbf{B}_{2n}|$ from Eq. (B.5) as follows,

$$\begin{aligned}
|\mathbf{B}_{2n}|^2 &= J^2(\mathbf{S}_{2n-1} + \mathbf{S}_{2n+1})^2 \\
&\quad + 4(K_\sigma^z)^2 \langle \sigma_{2n}^z \rangle^2 \mathbf{e}_z^2 + 4(K_\sigma^x)^2 \langle \sigma_{2n}^x \rangle^2 \mathbf{e}_x^2 \\
&\quad + 4JK_\sigma^z(\mathbf{S}_{2n-1} + \mathbf{S}_{2n+1}) \langle \sigma_{2n}^z \rangle \mathbf{e}_z \\
&\quad - 4JK_\sigma^x(\mathbf{S}_{2n-1} + \mathbf{S}_{2n+1}) \langle \sigma_{2n}^x \rangle \mathbf{e}_x \\
&\quad - 4K_\sigma^x K_\sigma^z \langle \sigma_{2n}^x \rangle \langle \sigma_{2n}^z \rangle \mathbf{e}_z \cdot \mathbf{e}_x \\
&= 4J^2 S^2 - J^2(\mathbf{S}_{2n-1} - \mathbf{S}_{2n+1})^2 \\
&\quad + 4(K_\sigma^z)^2 \langle \sigma_{2n}^z \rangle^2 + 4(K_\sigma^x)^2 \langle \sigma_{2n}^x \rangle^2 \\
&\quad + 4JK_\sigma^z(S_{2n-1}^z + S_{2n+1}^z) \langle \sigma_{2n}^z \rangle \\
&\quad - 4JK_\sigma^x(S_{2n-1}^x + S_{2n+1}^x) \langle \sigma_{2n}^x \rangle \\
&\simeq 4J^2 S^2 - J^2(\mathbf{S}_{2n-1} - \mathbf{S}_{2n+1})^2 \\
&\quad + 4JK_\sigma^z(S_{2n-1}^z + S_{2n+1}^z) \langle \sigma_{2n}^z \rangle \\
&\quad - 4JK_\sigma^x(S_{2n-1}^x + S_{2n+1}^x) \langle \sigma_{2n}^x \rangle \\
&= 4J^2 S^2 \left\{ 1 - \frac{1}{4S^2} (\mathbf{S}_{2n-1} - \mathbf{S}_{2n+1})^2 \right. \\
&\quad \left. + \frac{K_\sigma^z}{JS^2} \langle \sigma_{2n}^z \rangle (S_{2n-1}^z + S_{2n+1}^z) \right. \\
&\quad \left. - \frac{K_\sigma^x}{JS^2} \langle \sigma_{2n}^x \rangle (S_{2n-1}^x + S_{2n+1}^x) \right\}, \tag{B.52}
\end{aligned}$$

where we use the approximation $4(K_\sigma^z)^2 \langle \sigma_{2n}^z \rangle^2 + 4(K_\sigma^x)^2 \langle \sigma_{2n}^x \rangle^2 \ll J^2 S^2$. This leads to

$$\begin{aligned}
|\mathbf{B}_{2n}| &\simeq 2JS \left\{ 1 - \frac{1}{8S^2} (\mathbf{S}_{2n-1} - \mathbf{S}_{2n+1})^2 \right. \\
&\quad \left. - \frac{K_\sigma^z}{2JS^2} \langle \sigma_{2n}^z \rangle (S_{2n-1}^z + S_{2n+1}^z) \right. \\
&\quad \left. + \frac{K_\sigma^x}{2JS^2} \langle \sigma_{2n}^x \rangle (S_{2n-1}^x + S_{2n+1}^x) \right\}, \tag{B.53}
\end{aligned}$$

by applying the approximation $\sqrt{1+x} \simeq 1+x/2$ for small x . We obtain

$$\begin{aligned}
Z_{\sigma, S\sigma}^{(2n)} &\sim \exp \left[-\beta \left\{ -2JS\sigma + \frac{J\sigma}{4S} (\mathbf{S}_{2n-1} - \mathbf{S}_{2n+1})^2 \right. \right. \\
&\quad \left. + \frac{\sigma K_\sigma^x}{S} \langle \sigma_{2n}^2 \rangle (S_{2n-1}^x + S_{2n+1}^x) \right. \\
&\quad \left. - \frac{\sigma K_\sigma^z}{S} \langle \sigma_{2n}^2 \rangle (S_{2n-1}^z + S_{2n+1}^z) \right. \\
&\quad \left. - K_\sigma^z \langle \sigma_{2n}^z \rangle^2 + K_\sigma^x \langle \sigma_{2n}^x \rangle^2 \right\} \right]. \tag{B.54}
\end{aligned}$$

by substituting Eq. (B.53) into Eq. (B.49). The quantity $\langle \sigma_{2n}^x \rangle$ is obtained in self-consistent calculations using the following relation

$$\langle \sigma_{2n}^x \rangle^2 = \frac{1}{\beta} \frac{\partial}{\partial K_\sigma^x} \ln Z_{\sigma, S\sigma}^{(2n)}, \tag{B.55}$$

that holds from Eq. (B.44). In addition, Eq. (B.54) leads to the relation as follows,

$$\frac{1}{\beta} \frac{\partial}{\partial K_\sigma^x} \ln Z_{\sigma, S\sigma}^{(2n)} \sim -\frac{\sigma}{S} \langle \sigma_{2n}^2 \rangle (S_{2n-1}^x + S_{2n+1}^x) - \langle \sigma_{2n}^x \rangle^2. \quad (\text{B.56})$$

These relations result in

$$\langle \sigma_{2n}^x \rangle^2 = -\frac{\sigma}{S} \langle \sigma_{2n}^x \rangle (S_{2n-1}^x + S_{2n+1}^x) - \langle \sigma_{2n}^x \rangle^2 \quad (\text{B.57})$$

$$\langle \sigma_{2n}^x \rangle = -\frac{\sigma}{2S} (S_{2n-1}^x + S_{2n+1}^x). \quad (\text{B.58})$$

We also obtain

$$\langle \sigma_{2n}^z \rangle = -\frac{\sigma}{S} (S_{2n-1}^z + S_{2n+1}^z), \quad (\text{B.59})$$

through procedures parallel to those described above.

Finally, we reach the effective Hamiltonian by substituting Eqs. (B.53), (B.58), and (B.59) into Eq. (B.51) as follows,

$$\begin{aligned} H^{(2n)} &\sim H_S^{(2n)} - 2JS\sigma + \frac{J\sigma}{4S} (\mathbf{S}_{2n-1} - \mathbf{S}_{2n+1})^2 \\ &\quad + \frac{\sigma^2 K_\sigma^z}{4S^2} (S_{2n-1}^z + S_{2n+1}^z)^2 \\ &\quad - \frac{\sigma^2 K_\sigma^x}{4S^2} (S_{2n-1}^x + S_{2n+1}^x)^2 \end{aligned} \quad (\text{B.60})$$

$$\begin{aligned} &\sim H_S^{(2n)} - \frac{J\sigma}{2S} \mathbf{S}_{2n-1} \cdot \mathbf{S}_{2n+1} \\ &\quad + \frac{\sigma^2}{S^2} K_\sigma^z (S_{2n-1}^z)^2 - \frac{\sigma^2}{S^2} K_\sigma^x (S_{2n-1}^x)^2, \end{aligned} \quad (\text{B.61})$$

where $S_{2n-1}^{x(z)} \simeq S_{2n+1}^{x(z)}$. The total effective ferromagnetic Hamiltonian for a ferrimagnetic-aligned nanoparticle chain is shown in Eq. (B.6).

Acknowledgements

First and foremost, I would like to express my sincere gratitude to my supervisor, Prof. Noriyuki Hatakenaka for his continuous support and valuable advice. I really respect not only his immense knowledge and plentiful experience but also his passion for study. He gave me a compass for life as well as the knowledge required for studies. I am also deeply grateful to my subadvisors Prof. Satoshi Ishizaka, Prof. Seiji Higashitani, Prof. Norio Ogita, Prof. Tomohiro Inagaki, and Prof. Masataka Iinuma for their valuable comments and kind support. I would like to extend my sincere thanks to Dr. Toshiyuki Fujii and Prof. Ken-ichi Matsuda for their helpful discussion and technical support. I also wish to thank Dr. Sahel Ashhab and Ms. N Syakirah Nabilah S Bahri for their technical inputs. In addition, I would like to thank all of the members studying in the same student room, Mr. Shingo Uefuji, Mr. Kouki Sakurai, Mr. Yuta Yamamoto, and Mr. Yusuke Kanamori. They have made my study and life a wonderful time. Finally, my appreciation also goes out to my family and friends for their encouragement and support.

Bibliography

- [1] R. B. Laughlin and D. Pines, “From the cover: The theory of everything,” *Proceedings of the national academy of sciences of the United States of America*, vol. 97, no. 1, p. 28, 2000.
- [2] C. Kiefer, *Quantum Gravity — A Short Overview*, pp. 1–13. Basel: Birkhäuser Basel, 2007.
- [3] S. W. Hawking, “Black hole explosions?,” *Nature*, 1974.
- [4] S. W. Hawking, “Particle creation by black holes,” *Comm. Math. Phys.*, vol. 43, no. 3, pp. 199–220, 1975.
- [5] K. Schwarzschild, “Über das Gravitationsfeld eines Massenpunktes nach der Einsteinschen Theorie,” *Sitzungsberichte der Königlich Preussischen Akademie der Wissenschaften (Berlin)*, 1916.
- [6] K. Schwarzschild, “On the gravitational field of a mass point according to einstein’s theory,” 1999.
- [7] W. G. Unruh, “Experimental black-hole evaporation?,” *Phys. Rev. Lett.*, vol. 46, pp. 1351–1353, 1981.
- [8] M.-a. Sakagami and A. Ohashi, “Hawking radiation in the laboratory,” *Progress of Theoretical Physics*, vol. 107, no. 6, pp. 1267–1272, 2002.
- [9] G. E. Volovik, “Simulation of a Panlevé-Gullstrand black hole in a thin 3He-A film,” *Journal of Experimental and Theoretical Physics Letters*, vol. 69, no. 9, pp. 705–713, 1999.
- [10] L. J. Garay, J. R. Anglin, J. I. Cirac, and P. Zoller, “Sonic analog of gravitational black holes in Bose-Einstein condensates,” *Phys. Rev. Lett.*, vol. 85, pp. 4643–4647, 2000.
- [11] R. Schützhold and W. G. Unruh, “Hawking radiation in an electromagnetic waveguide?,” *Phys. Rev. Lett.*, vol. 95, p. 031301, 2005.
- [12] T. G. Philbin, C. Kuklewicz, S. Robertson, S. Hill, F. König, and U. Leonhardt, “Fiber-optical analog of the event horizon,” *Science*, vol. 319, no. 5868, pp. 1367–1370, 2008.
- [13] C. Barceló, “Analogue black-hole horizons,” *Nature Phys.*, vol. 15, no. 3, pp. 210–213, 2019.
- [14] O. Lahav, A. Itah, A. Blumkin, C. Gordon, S. Rinott, A. Zayats, and J. Steinhauer, “Realization of a sonic black hole analog in a bose-einstein condensate,” *Phys. Rev. Lett.*, vol. 105, p. 240401, 2010.

- [15] J. Steinhauer, “Observation of quantum hawking radiation and its entanglement in an analogue black hole,” *Nature Physics*, vol. 12, no. 10, pp. 959–965, 2016.
- [16] A. Finke, P. Jain, and S. Weinfurter, “On the observation of nonclassical excitations in bose–einstein condensates,” *New Journal of Physics*, vol. 18, no. 11, p. 113017, 2016.
- [17] U. Leonhardt, “Questioning the recent observation of quantum hawking radiation,” *Annalen der Physik*, vol. 530, no. 5, p. 1700114, 2018.
- [18] F. Belgiorno, S. L. Cacciatori, G. Ortenzi, V. G. Sala, and D. Faccio, “Quantum radiation from superluminal refractive-index perturbations,” *Phys. Rev. Lett.*, vol. 104, p. 140403, 2010.
- [19] E. Rubino, F. Belgiorno, S. L. Cacciatori, M. Clerici, V. Gorini, G. Ortenzi, L. Rizzi, V. G. Sala, M. Kolesik, and D. Faccio, “Experimental evidence of analogue hawking radiation from ultrashort laser pulse filaments,” *New Journal of Physics*, vol. 13, no. 8, p. 085005, 2011.
- [20] C. M. Wilson, G. Johansson, A. Pourkabirian, M. Simoen, J. R. Johansson, T. Duty, F. Nori, and P. Delsing, “Observation of the dynamical casimir effect in a superconducting circuit,” *Nature*, vol. 479, no. 7373, 2011.
- [21] P. D. Nation, M. P. Blencowe, A. J. Rimberg, and E. Buks, “Analogue hawking radiation in a dc-squid array transmission line,” *Phys. Rev. Lett.*, vol. 103, p. 087004, 2009.
- [22] J. S. Russell, “Report on waves,” *Report of the Fourteenth Meeting of the British Association for the Advancement of Science*, pp. 311–390, 1844.
- [23] N. J. Zabusky and M. D. Kruskal, “Interaction of ”solitons” in a collisionless plasma and the recurrence of initial states,” *Phys. Rev. Lett.*, vol. 15, pp. 240–243, 1965.
- [24] C. S. Gardner, J. M. Greene, M. D. Kruskal, and R. M. Miura, “Method for solving the korteweg-devries equation,” *Phys. Rev. Lett.*, vol. 19, pp. 1095–1097, 1967.
- [25] M. Toda, “Vibration of a chain with nonlinear interaction,” *Journal of the Physical Society of Japan*, vol. 22, no. 2, pp. 431–436, 1967.
- [26] D. D. J. Korteweg and D. G. de Vries, “Xli. on the change of form of long waves advancing in a rectangular canal, and on a new type of long stationary waves,” *The London, Edinburgh, and Dublin Philosophical Magazine and Journal of Science*, vol. 39, no. 240, pp. 422–443, 1895.
- [27] A. Hasegawa and F. Tappert, “Transmission of stationary nonlinear optical pulses in dispersive dielectric fibers. i. anomalous dispersion,” *Applied Physics Letters*, vol. 23, no. 3, pp. 142–144, 1973.
- [28] M. Toda, “Wave propagation in anharmonic lattices,” *Journal of the Physical Society of Japan*, vol. 23, no. 3, pp. 501–506, 1967.
- [29] R. Hirota and K. Suzuki, “Studies on lattice solitons by using electrical networks,” *Journal of the Physical Society of Japan*, vol. 28, no. 5, pp. 1366–1367, 1970.
- [30] H. Nagashima and Y. Amagishi, “Experiment on the toda lattice using nonlinear transmission lines,” *Journal of the Physical Society of Japan*, vol. 45, no. 2, pp. 680–688, 1978.

- [31] T. Taniuti and C.-C. Wei, “Reductive perturbation method in nonlinear wave propagation. i,” *Journal of the Physical Society of Japan*, vol. 24, no. 4, pp. 941–946, 1968.
- [32] T. Taniuti and N. Yajima, “Perturbation method for a nonlinear wave modulation. i,” *Journal of Mathematical Physics*, vol. 10, no. 8, pp. 1369–1372, 1969.
- [33] T. Taniuti, “Reductive Perturbation Method and Far Fields of Wave Equations,” *Progress of Theoretical Physics Supplement*, vol. 55, pp. 1–35, 1974.
- [34] L. Gardner, G. Gardner, and T. Geyikli, “Solitary wave solutions of the mKdV – equation,” *Computer Methods in Applied Mechanics and Engineering*, vol. 124, no. 4, pp. 321 – 333, 1995.
- [35] G. Chanteur and M. Raadu, “Formation of shocklike modified Korteweg-de Vries solitons: Application to double layers,” *The Physics of Fluids*, vol. 30, no. 9, pp. 2708–2719, 1987.
- [36] G. J. Chen and M. R. Beasley, “Shock-wave generation and pulse sharpening on a series array Josephson junction transmission line,” *IEEE Transactions on Applied Superconductivity*, vol. 1, no. 3, pp. 140–144, 1991.
- [37] H. R. Mohebbi and A. H. Majedi, “Shock wave generation and cut off condition in nonlinear series connected discrete Josephson transmission line,” *IEEE Transactions on Applied Superconductivity*, vol. 19, no. 3, pp. 891–894, 2009.
- [38] H. Ghafouri-Shiraz and P. Shum, “Narrow pulse formation using nonlinear LC ladder networks,” *Fiber and Integrated Optics*, vol. 15, no. 4, pp. 305–323, 1996.
- [39] C. Kengne, E. and Bame, “Dynamics of modulated wave trains in a discrete nonlinear-dispersive dissipative bi-inductance transmission line,” *Czech J Phys*, vol. 55, p. 609–630, 2005.
- [40] E. Kengne and A. Lakhssassi, “Analytical study of dynamics of matter-wave solitons in lossless nonlinear discrete bi-inductance transmission lines,” *Phys. Rev. E*, vol. 91, p. 032907, 2015.
- [41] E. Kengne and A. Lakhssassi, “Analytical studies of soliton pulses along two-dimensional coupled nonlinear transmission lines,” *Chaos, Solitons & Fractals*, vol. 73, pp. 191–201, 2015.
- [42] E. Kengne and W. M. Liu, “Transmission of rogue wave signals through a modified Noguchi electrical transmission network,” *Phys. Rev. E*, vol. 99, p. 062222, 2019.
- [43] S. Abdoukary, L. English, and A. Mohamadou, “Envelope solitons in a left-handed nonlinear transmission line with Josephson junction,” *Chaos, Solitons & Fractals*, vol. 85, pp. 44–50, 2016.
- [44] J. B. Hartle and S. W. Hawking, “Path-integral derivation of black-hole radiance,” *Phys. Rev. D*, vol. 13, pp. 2188–2203, 1976.
- [45] W. G. Unruh and R. Schützhold, “On slow light as a black hole analogue,” *Phys. Rev. D*, vol. 68, no. 2, 2003.
- [46] M. K. Parikh and F. Wilczek, “Hawking radiation as tunneling,” *Phys. Rev. Lett.*, vol. 85, pp. 5042–5045, 2000.

- [47] M. K. Parikh, “Energy conservation and hawking radiation,” *The Tenth Marcel Grossmann Meeting*, 2006.
- [48] M. P. Blencowe and V. Vitelli, “Universal quantum limits on single-channel information, entropy, and heat flow,” *Phys. Rev. A*, vol. 62, p. 052104, 2000.
- [49] R. Mistry, S. Upadhyay, A. F. Ali, and M. Faizal, “Hawking radiation power equations for black holes,” *Nuclear Physics B*, vol. 923, pp. 378 – 393, 2017.
- [50] H. Katayama, N. Hatakenaka, and T. Fujii, “Analogue hawking radiation from black hole solitons in quantum josephson transmission lines,” *Phys. Rev. D*, vol. 102, p. 086018, 2020.
- [51] S. Corley and T. Jacobson, “Hawking spectrum and high frequency dispersion,” *Physical Review D*, vol. 54, no. 2, 1996.
- [52] S. Corley, “Computing the spectrum of black hole radiation in the presence of high frequency dispersion: An analytical approach,” *Phys. Rev. D*, vol. 57, no. 10, 1998.
- [53] S. Corley and T. Jacobson, “Black hole lasers,” *Phys. Rev. D*, vol. 59, p. 124011, 1999.
- [54] J. Steinhauer, “Observation of self-amplifying hawking radiation in an analogue black-hole laser,” *Nature Physics*, vol. 10, no. 11, pp. 864–869, 2014.
- [55] D. Faccio, T. Arane, M. Lamperti, and U. Leonhardt, “Optical black hole lasers,” *Classical and Quantum Gravity*, vol. 29, no. 22, p. 224009, 2012.
- [56] J. L. Gaona-Reyes and D. Bermudez, “The theory of optical black hole lasers,” *Annals of Physics*, vol. 380, 2017.
- [57] T. Weißl, B. Küng, E. Dumur, A. K. Feofanov, I. Matei, C. Naud, O. Buisson, F. W. J. Hekking, and W. Guichard, “Kerr coefficients of plasma resonances in josephson junction chains,” *Phys. Rev. B*, vol. 92, p. 104508, 2015.
- [58] Y. Krupko, V. D. Nguyen, T. Weißl, E. Dumur, J. Puertas, R. Dassonneville, C. Naud, F. W. J. Hekking, D. M. Basko, O. Buisson, N. Roch, and W. Hasch-Guichard, “Kerr nonlinearity in a superconducting josephson metamaterial,” *Phys. Rev. B*, vol. 98, p. 094516, 2018.
- [59] J. Ieda and Y. Yamane, “Intrinsic and extrinsic tunability of rashba spin-orbit coupled emergent inductors,” *Phys. Rev. B*, vol. 103, p. L100402, 2021.
- [60] J. D. Rincon - Estrada and D. Bermudez, “Instabilities in an optical black - hole laser,” *Annalen der Physik*, vol. 533, no. 1, 2020.
- [61] A. Hasegawa and F. Tappert, “Transmission of stationary nonlinear optical pulses in dispersive dielectric fibers. i. anomalous dispersion,” *Applied Physics Letters*, vol. 23, no. 3, pp. 142–144, 1973.
- [62] Y. Ohsawa and Y. Fujii, “Stationary solution of nonlinear propagation of femtosecond optical pulse by circuit model,” *Journal of the Physical Society of Japan*, vol. 61, no. 11, pp. 3977–3983, 1992.

- [63] R. del Coso and J. Solis, “Relation between nonlinear refractive index and third-order susceptibility in absorbing media,” *J. Opt. Soc. Am. B*, vol. 21, no. 3, pp. 640–644.
- [64] L. Fasolo, A. Greco, and E. Enrico, “Superconducting josephson-based metamaterials for quantum-limited parametric amplification: A review,” in *Advances in Condensed-Matter and Materials Physics* (J. Thirumalai and S. I. Pokutnyi, eds.), ch. 5, Rijeka: IntechOpen, 2020.
- [65] U. Leonhardt and T. G. Philbin, “Black hole lasers revisited,” in *Quantum Analogues: From Phase Transitions to Black Holes and Cosmology* (W. G. Unruh and R. Schützhold, eds.), pp. 229–245, Berlin, Heidelberg: Springer Berlin Heidelberg, 2007.
- [66] S. M. Barnett and S. J. D. Phoenix, “Entropy as a measure of quantum optical correlation,” *Phys. Rev. A*, vol. 40, pp. 2404–2409, 1989.
- [67] S. Brahma, O. Alaryani, and R. Brandenberger, “Entanglement entropy of cosmological perturbations,” *Phys. Rev. D*, vol. 102, p. 043529, 2020.
- [68] H. How, R. C. O’Handley, and F. R. Morgenthaler, “Soliton theory for realistic magnetic domain-wall dynamics,” *Phys. Rev. B*, vol. 40, pp. 4808–4817, 1989.
- [69] G.-P. Zheng, J.-Q. Liang, and W. M. Liu, “Instantons in a ferromagnetic spin chain with biaxial anisotropy,” *Phys. Rev. B*, vol. 79, p. 014415, 2009.
- [70] S. Ishizaka and K. Nakamura, “Propagation of solitons of the magnetization in magnetic nanoparticle arrays,” *Journal of Magnetism and Magnetic Materials*, vol. 210, no. 1, pp. 15 – 19, 2000.
- [71] S. T. Chui and V. N. Ryzhov, “Soliton and 2d domains in ultrathin magnetic films,” *Phys. Rev. Lett.*, vol. 78, pp. 2224–2227, 1997.
- [72] F. Ferraro, D. Gatteschi, A. Rettori, and M. Corti, “Nmr investigation of $\text{Mn}(\text{hfac})_2\text{nitipr}$: evidence of nonlinear excitations in a one-dimensional ferrimagnet,” *Molecular Physics*, vol. 85, no. 6, pp. 1073–1088, 1995.
- [73] C. A. Condat, R. A. Guyer, and M. D. Miller, “Double sine-gordon chain,” *Phys. Rev. B*, vol. 27, pp. 474–494, 1983.